Electroluminescence in Ion Gel Gated Organic Polymer Semiconductor Transistors

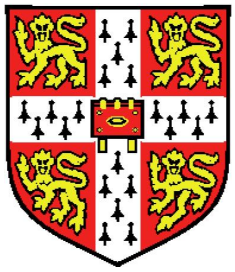

Shrivalli Bhat

Queens' College

University of Cambridge

A dissertation submitted for the degree of

Doctor of Philosophy

March 2011

To
Sunshine,
Raindrops
and
Harsha.

Acknowledgements

This thesis is a result of the work undertaken at the Cavendish Laboratory at the University of Cambridge between October 2007 and March 2010. I would like to express my gratitude towards the Gates Cambridge Trust and Cambridge Overseas Trust for the financial support during this period. I would also like to express the same towards The Queens' college and The Department of Physics.

I am thankful to my supervisor Prof. Henning Sirringhaus, for helping me in understanding the physics behind the light emission in ion gel gated transistors as well as for his exemplary calm and consistent patience.

Thanks to many friends who have always been open to technical discussions and have helped me in the lab in different ways, Matt Bird, Anup Dhoot, Mario Caironi, Dinesh Kabra, Sylvain Massip, Ronald Naber, Tomo Sakanoue, Thomas Strobel and Burak Ulgut. Special thanks to Riccardo Di Pietro for the help in CMS measurements and to Micheal Gwinner for ZnO patterns. Many thanks to Roger Beadle, Radoslav Chakalov, Alex Crook, Richard Gymer, Ron Hodierne, Jean Phillips, and Gilly Walker for their help in distinct different aspects.

Thanks to all of my beloved colleagues from the group. Especially, thanks to each and every one who were in the Pen of OE-FET group, during the period of time starting from October 2007 to March 2010. Special thanks to Dong Fang, Mijung Lee, Aurlie Meneau, Jenny Moore, Sebastian Mooser, George Nikiforov, Vincenzo Pecunia, Alesandro Rossi and Sebastian Schoefer for their cheerful affection.

I would like to express my gratefulness to the folks in my life. To my loving family, admirable teachers and fond friends. I am indebted

to them for helping me to cultivate different perspectives towards different things in life.

I thank Harsha (N. Shastri), without whom I wouldn't call myself complete, and am filled with gratitude to the cause that has brought us together, be it the god or that nature of probability function or the free will.

Abstract

This thesis reports the light emission in ion gel gated, thin film organic semiconductor transistors and investigates the light emission mechanism behind these devices. We report that ion gel gated organic polymer semiconductor transistors emit light when the drain source voltage is swept slightly beyond the energy gap of the polymer divided by the elementary charge ($V_{ds} > E_g/e$). In particular, the light emission in poly(9,9'-dioctylfluorene-co-benzothiadiazole) (F8BT) polymer semiconductor, with 1-ethyl-3-methylimidazoliumbis (trifluoromethylsulfonyl) imide/ poly(styrene-block-ethylene oxide-block-styrene (EMIM TFSI/ SOS) ion gel as dielectric material is reported. The current-voltage characteristics corresponding to the light emission, where the systematic increase of the drain current, correlated with light emission is reported. In low voltage regime, ($V_{ds} < E_g/e$), well saturated transistor characteristics are observed. By charge modulation spectroscopy (CMS) study we show that there is a prominent electrochemical doping occurring with gate voltages. Further, owing to the movement of ions with voltages, irrespective of the location of electrodes, we show that the ion gel, bilayer planar devices emit light in $V_{ds} > E_g/e$ regime (without any gate voltages), at room temperature. Based on the location of the recombination zone in the proximity of electron injecting electrode and CMS results showing prominent diffusion the of negative ions into the polymer layer, we conclude that the light emitting mechanism is akin to light emitting electrochemical cells (LECs). Even in the the transistor regime, where $V_{ds} \ll E_g/e$, with the signatures of increasing drain current for fixed V_g and V_{ds} values, we show that the transistor can not be of purely electrostatic operation alone.

We study the fluorescence quenching of an operating bilayer device under a constant bias over a period of time and compare the results with the electroluminescence of the device and show that the formation of the p-n junction within the polymer layer due to the penetrated ions from the gel dielectric into the polymer semiconductor layer on the application of the voltage is the cause behind the light emission. We show that diffusivity of the cation (EMIM) is very low compared to the anion (TFSI). This is consistent with the fact that the recombination zone is near the electron injecting electrode in these devices.

We have developed a theoretical model for the ions movement within the semiconductor polymer matrix governed by both diffusion and drift independently, for the bilayer, polymer ion gel planar, light emitting electrochemical cells. We have further developed a 2- dimensional numerical model based on the theoretical model and have compared the results of the numerical model with the results of a fluorescence probing of the bilayer device with time, at constant potential across the bilayer LEC and report that the drift coefficient of $1.0 \times 10^{-13} cm^2/Vs$ and a diffusion coefficient of $1.0 \times 10^{-15} cm^2/s$ for TFSI ions in F8BT matrix.

Except where specific reference is made to the involvement of others, the work presented herein is my own and contains nothing which is the result of collaboration. This dissertation has not been submitted in whole or in part for the award of a degree at this, or any other University and does not exceed 60,000 words in length.

Shrivalli Bhat
Cambridge, March 2011

Contents

Chapter 1

Introduction

Light emitting organic polymer semiconductor devices such as light emitting diodes (LEDs)[10] [46], light emitting field effect transistors (LEFETs)[56] [138], light emitting electrochemical cells (LECs)[101] have been of great interest recently due to their lower material and fabrication costs for application areas like large area displays. Organic light emitting semiconductor devices can be fabricated with a simple printing process, reducing the fabrication cost substantially compared to their inorganic counterparts. Further, several of the organic semiconductor materials are lighter, flexible and environmentally friendlier compared to current generation inorganic light emitting devices.

However, before the organic light emitting devices become mainstream, there are several challenges that need to be resolved and current research focus is to address those challenges. One particular challenge is relatively high operating voltages of light emitting organic semiconductor FETs. In case of LEFETs, though the devices are very interesting light emitting devices with gate modulation, the operating voltage is high in the range of 40-100V[138] with traditional dielectric materials. Many different distinct attempts[7] [85] [59] [123] [55] to bring down the operating voltages have been reported. Some include a proper matching of the work functions of the metal electrodes used in case of LEDs[65], and in case of LEFETs, in addition to this, a very thin gate dielectric materials would bring down the operating voltages.

Ion gel materials have shown great promise as a gate dielectric material due to their high ionic conductivity leading to high specific capacitance. Their physical

properties like transparency and flexibility also make them ideally suited in light emitting applications. Ion gels are obtained by gelation of an ionic liquid and a copolymer. The motivation of this work is to develop and study organic semiconductor devices with ion gel gate material and to demonstrate the light emission in transistors with low operating voltages. In this work the ion gel materials with high specific capacitance ($\approx$ few $\mu F/cm^2$) [72] are used as gate dielectric materials with polymer semiconductor in transistors.

In this work, I have reported for the first time the light emission in ion gel gated polymer transistors at low operating voltages such as 3 V. The current-voltage characteristics corresponding to the light emission in $V_{ds} > E_g/e$ regime, where the systematic increase of the drain current, correlated with light emission is reported. We present the recombination zone profiles of the light emission. Further, we show a systematic increase in the ion concentration with gate voltages in the active polymer layer under the hole accumulation regime. Based on ions penetration in hole accumulation regime we show that the light emission in ion gel gated polymer transistor is akin to LECs.

Furthermore, we report the light emission in the polymer semiconductor, ion gel planar bilayer devices without any gate modulation at room temperature in nitrogen atmosphere (they do emit light in air as well), with external quantum efficiencies of the order of $10^{-4}\%$. The devices have a very low switch-on voltage for light emission of the order of the energy gap of the polymer divided by the elementary charge. Though the operating mechanism is very similar to LECs due to the assistance of penetrated ions from the gel layer to the active polymer layer on the application of voltage, unlike LECs, these planar bilayer polymer ion gel light emitting devices do not have any phase separation problems. A typical LEC, which consists the ions in the active layer itself due to the mixing of the polymer electrolyte with semiconductor polymer suffers from phase separation issues.

In order to understand the doping mechanism and to quantify the drift and diffusion coefficients for the ions penetrating into the semiconductor on the application of voltage, we have also developed a theoretical and numerical model for the bilayer LEC device and compare the numerical data obtained with the fluorescence probing of an operating device.

Further, we report two orders of magnitude increase in the external quantum efficiency values, by eliminating the metal absorption by introducing transparent ZnO as electron injecting layer. We also report higher values (0.06%) of external quantum efficiency by changing the anion in the ion gel layer.

The rest of this work is divided in to several chapters as described below, concentrating on particular aspects of my work.

Chapter 2 provides a brief background into the current developments in the area of organic semiconductors related to this work, in particular reference to low voltage light emitting polymer devices and gate dielectrics. **Chapter 3** deals with the detailed discussion about the polymer semiconductor materials, ion gel materials, device fabrication methods and measurement techniques used in this work.

Chapter 4 reports light emission from an 1-ethyl-3-methyl imidazolium bis (trifluoro methyl sulfonyl)imide/ poly(styrene- block-ethylene oxide- block- styrene EMIM-TFSI/SOS ion gel gated poly(9,9'-dioctyl fluorene-co-benzo thiadiazole) F8BT polymer system. We distinguish two separate regimes: when the drain source voltage (V_{ds}) is well below the energy gap (E_g) of the polymer, the device behaves as a stable FET with a well defined current saturation regime. On the other hand, when the $V_{ds} > E_g/e$ (where e is the elementary charge) the current starts to increase rapidly and we observe corresponding light emission from the channel.

Based on the increasing drain current at constant V_{ds} and V_g values in the output characteristics and large hysteresis with transfer characteristics of the transistor we investigate the role of ions behind this light emission carefully. Using the charge modulation spectroscopy (CMS) we study the gate voltage dependent ion diffusion from dielectric layer to the polymer semiconductor layer, which increases the charge accumulation dramatically. We see a clear gate voltage dependence of negative ions ($TFSI^-$) diffusion into polymer layer under the hole accumulation (negative gate voltages) which increases with increasing gate voltage. We do not see a clear evidence for gate voltage dependent diffusion of ($EMIM^+$) ions under the electron accumulation regime which is consistent with the fact that we do not have electron transportation with this system and the location of the recombination zone is in the proximity of the electron injecting

electrode.

Moreover, two terminal bilayer devices (without any gate voltage) emit light at room temperature, with similar increase in the current values and corresponding light emission, given the sufficient amount of time for ion diffusion to take place. In these planar devices, without the third modulating terminal (gate terminal), the potential difference between the source and drain electrodes helps ion displacements and diffusion which eventually lead to light emission similar to the work by Sandstrom et al.[113] at high temperatures. These results independently suggest that ion-gel gated FETs operate akin to LECs when $V_{ds} > E_g/e$.

In **chapter 5** we further investigate the nature of the two-terminal bilayer devices. We develop and study F8BT EMIM/TFSI bilayer devices. We report that these devices have a clear onset voltage for light emission and light emission follows the diode equation. The light emission in these devices occurs in the proximity of the electron injecting electrodes, indicating that the light emission is limited by electron transport. To improve the EQE of the device by reducing the light absorption by metal electrode, we fabricate devices with transparent ZnO layer, moving electron injection zone away from the metal electrode. We further report the enhancement of the EQE of the device, also by using a different cation(1-butyl-4-methyl pyridinium bis(trifluoromethane sulfonyl)imide) in the gel layer shifting the recombination zone about a micrometer away from the electrode.

In **chapter 6** we present a theoretical and numerical model to describe the movement of ions within the semiconductor layer. We first demonstrate that a theoretical model which lumps the drift and diffusion coefficients into one single diffusion coefficient is inadequate to satisfactorily explain the motion of ions within the semiconductor. We further develop a model based on drift and diffusion effects taken into account independently. We implement the theoretical model into a numerical model and solve the governing partial differential equation using numerical methods. We compare the results of the numerical model with experimental results from the photoluminescence quenching study on a F8BT-TFSI/EMIM bilayer device under constant applied voltage. We obtain a good match between the experimental and numerical results and also use the numerical model to obtain accurate estimates for the diffusion coefficient and mobility of

$TFSI^-$ ions within the F8BT semiconductor layer.

Finally, **chapter 7** presents concluding remarks on this work and an outlook for further development based on current work.

Chapter 2

Background

This chapter provides a background into organic semiconducting polymers, in particular about the electroluminescence in organic semiconductors. Furthermore, the chapter discusses light emitting diodes, light emitting field effect transistors and light emitting electromechanical cells and their operating mechanisms. We further include a review of low voltage operating polymer electrolyte gated and ion gel gated transistors. We discuss the challenges associated with determining the precise operating mechanism of an ion gel gated transistor.

2.1 Conjugated semiconductor polymers

Semiconducting conjugated polymers are an interesting class of materials that combine the electronic and optical properties of semiconductors with the processability of conventional polymers. A conjugated polymer contains a system of connected p-orbitals with delocalized electrons with alternating single and multiple bonds. Since the discovery of charge carrying organic compounds in the 1950's,[92] there has been significant progress in synthesizing new organic conducting polymers and understanding their underlying charge carrying mechanism. Though there are some important difference between the organic and inorganic semiconductors most of the electronic and optical properties of inorganic semiconductors have been found in organic polymer semiconductors, which also possess the flexible properties in addition. The semiconducting properties of these flex-

ible, cheaper plastic materials, in comparison with their inorganic counterparts however are less understood. Light emitting diodes, field effect transistors, solar cells, photo detectors etc. [8] [48] [134] [9] have been demonstrated using these polymer semiconductors. Amidst all of the different applications the applications based on the electroluminescent properties of these polymers are particularly attractive.

2.1.1 Optical Properties

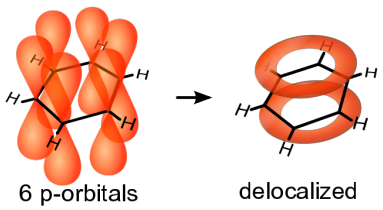

Figure 2.1: Conjugated, planar, cyclic compounds that follow Huckel's rule exhibit an unusual stability. The classic example benzene has a system of all together 6 electrons above and below the flat planar ring.

Semiconducting properties of conjugated polymers is due the localized π-electron bonding along the polymer chain. The π (HOMO) and π^* (LUMO) orbitals for delocalized valence and conduction wave functions support the mobile holes and electrons. A conjugated system is a system of connected π-orbitals with delocalized electrons in compounds with alternating single and multiple bonds. (example, benzene. Figure 2.1). Conjugated polymers mainly consist of carbon atoms, with the electronic configuration $1s^2 2s^2 2p^2$. Since $2s^2$, p_x and p_y orbitals are energetically similar they hybridize into three sp^2 hybrid orbitals. These hybrid orbitals combine with the $1s$ orbital of the hydrogen or with another $2sp^2$ orbital from another carbon to form σ bonds. The remaining p_z electron does not take part in the hybridization and occupies the orbital perpendicular to the plane of the hybrid orbitals. The p_z orbitals on adjacent carbon atoms overlap to create the molecular bonding π (bonding)and π^* orbitals (anti-bonding) with electron density located above and below the molecule plane (as shown with benzene example in figure 2.1). A double bond consists of a σ and a π molecular orbital. In a conjugated polymer system, a chain of carbon atoms is connected

by alternating single and double bonds.

The highest occupied molecular orbital is called the HOMO level, while the lowest unoccupied molecular orbital is called the LUMO level. With increasing number of carbon atoms contributing to p_z-orbitals the number of possible energy levels increases and the energy difference between the LUMO and the HOMO level decreases. If we consider an infinite perfectly conjugated chain of carbon atoms, the discrete energy levels turn into a one dimensional energy band that is partially filled. Since this ideal molecule has a degenerate ground state the system can still lower the energy by breaking its symmetry with a lattice deformation (electron phonon coupling) and thus opening a gap at the Fermi level. Due to the formation of this bandgap, this ideal conjugated molecule is not a conductor. But when it is doped either by partially filling the empty band or emptying the filled band it becomes a conductor. In a realistic conjugated polymer the delocalization of electrons is limited by conformational and spatial disorder. The p_z-orbitals have to be in plane for them to overlap and delocalize.

In general, only stretches of a certain length exist in the polymer chain and this length is called the conjugation length. The conjugation length is typically is of the order of several nanometers[136]. A conjugated polymer can be visualized as a chain of conjugated oligomers of different lengths. This distribution of conjugation lengths gives rise to a distribution of the HOMO and LUMO energies, which is mirrored in the broad Gaussian shape of the absorption peaks of conjugated polymers. The optical bandgap, the energy difference between HOMO and LUMO level, of most conjugated polymers lies within the visible region of the electromagnetic spectrum. Changing the chemical structure of the polymer backbone affects its electronic and optical properties. This allows tailoring of conjugated polymers to the needs of a specific application.

When a photon is absorbed by a conjugated polymer an electron can be excited from the HOMO level to an LUMO level. This excited state is called an exciton and can be represented as a bound electron-hole pair. The exciton is associated with a lattice distortion and it creates new energy levels within the HOMO-LUMO bandgap. The energy required to separate the electron hole pair, the exciton binding energy, is around 0.4 eV in conjugated polymers, which gives the exciton an extent[36] [124] of about 1 nm. Since electronic transitions happen

very fast compared to nuclear motions they are completed before the molecule reaches the vibrational ground state of the new electronic state (Franck-Condon principle). The electron could thus be excited to upper vibronic states. It then relaxes without radiation emission to the lowest vibrational state, from which it can return to its ground state by emission of light (photoluminescence) or by a radiationless channel of decay. Due to this, the emitted light has a longer wavelength than the absorbed light. This difference is called the Stokes shift [79].

Additionally, energy transfer from higher energy sites to lower energy sites of conjugated polymers results in a shift between absorption and emission. There are two possible excited electronic states depending on the nature of spins of bound electron and the hole. The state is called a singlet state if the spins of the bound electron and hole are antiparallel, and it is called a triplet state if the spins are parallel. Triplet states have lower energy than singlet states [1].

Due to spin conservation only singlets can be formed by optical excitation. Those singlets formed by optical excitations can then undergo intersystem crossing to form triplets. This process, however, is slow and hence usually the non radiative and radiative decay of singlets dominates. Radiative decay of singlets is called fluorescence, while radiative decay of triplets is called phosphorescence. Because the transition between the triplet state and the ground state is spin-forbidden, the lifetime of triplets is long compared to singlets (few ns) [136].

During operation of a light emitting diode or a polymer field effect transistor charges are accumulated and transported within the semiconducting polymer film. The presence of a positive or negative charge causes a local structural relaxation of the polymer chain around the charge due to electron-phonon coupling similar to that of an exciton. This quasi-particle (spin = 1/2) of a charge and a lattice distortion is called a polaron for polymers with a non-degenerate ground state, which is the case for many conjugated polymers. Such a change in bond alteration can be observed by spectroscopic studies. The formation of a polaron state also results in the creation of two new energy levels within the bandgap. In an electron polaron state one electron occupies the high energy bandgap level [40].

In a hole polaron state a hole exists in the low energy level. These states allow new electronic transitions, that is, new absorption features. Not all of these transitions are symmetry allowed. As shown in figure 2.2 HOMO and LUMO

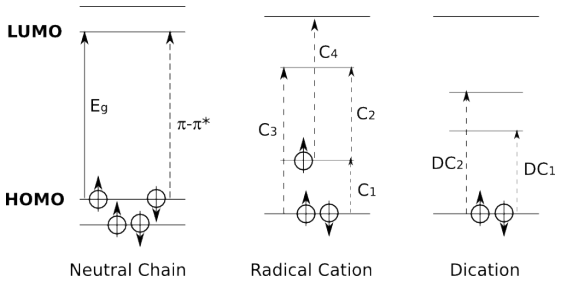

Figure 2.2: Schematic of one-electron energy level diagram and optical transition of (a)neutral, (b) singly charged (polaron) (c) doubly charged (bipolaron) organic polymer semiconductor. Only C1, C2 and DC1 optical transitions are allowed in the polaron and bipolaron energy diagram,as the rest are forbidden since the transition can only occur between asymmetrical orbitals [19]

and polaron levels for a conjugated polymer with a positive or a negative charge and the allowed and forbidden transitions. Adding another charge to the polymer chain would lead to the formation of a spinless bipolaron with an even stronger lattice deformation and energy states deeper in the band gap. These new optical transitions can be used to study charges accumulated in a polymer field effect transistor by charge modulation spectroscopy studies [51] [132].

Field effect transistors, with the gate modulation, unlike LEDs are in particular interesting devices from the fundamental point of view of understanding the charge transportation in the active semiconductor layer, i.e, organic semiconductors.

2.2 Electroluminescence in organic semiconductor polymers

Electroluminescence in organic semiconductors is the prime factor that lead these plastic materials [80] towards fascinating applications [129] [130] [10] [40]. Conjugated polymers show very high photoluminescence and electroluminescence efficiencies over the whole visible light range as well as decent charge transport. These properties enable their use in light emitting diodes.The first report of observation of light emission was reported in anthracene single crystals, back in 1960s [104]. From then onwards, over the last decades lots of effort has been invested in

understanding the underlying science controlling the properties of organic single crystals, small molecules and polymer semiconductors.

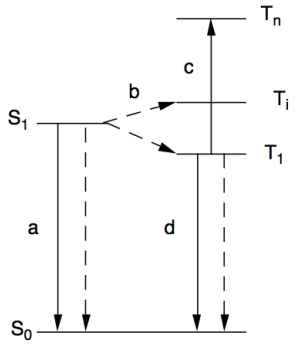

Figure 2.3: Schematic for singlet decay and triplet excitation and decay. Solid arrows represent radiative processes and dashed lines represent not radiative processes. Fluorescence (a), inter system crossing (b), photo induced triplet-triplet absorption (c),and phosphorescence (d)are represented. S_0 is the ground (singlet) state, S_1 is the first excited singlet, T_1 is the first excited triplet, and T_i and T_n are higher lying triplet states. With permission from reference [40]

The process of electron and holes capturing is what that determines the electroluminescence. Modeling of the charge recombination by Langevin theory has been used by several groups [50] [105] [62].

From the Langevin model, electron hole capture process is spin independent. Excitons are formed with spin wave functions with the triplet singlet configurations in the ratio 3:1. However, transition from the triplet excited state to the singlet ground state is symmetry forbidden. This means 75% of the electron hole pairs to the triplet excitons do not decay radiatively. This reduces the efficiency. There have been several approaches to make use of the triplet excitons. One is to introduce the species, that allows sufficient triplet luminescence with high atomic number elements with strong spin orbit coupling [35] [78].

Understanding of the nature of the neutral excited states in conjugated polymers has been advanced by a wide range of quantum-chemical calculations. Inclusion of both electron -electron and electron-phonon terms turns out to be essential to establish a coherent picture of the photo excitations. Figure 2.3 shows the schematic for singlet decay and triplet excitation and decay. Solid arrows represent radiative processes and dashed lines represent non-radiative processes. High

emission requires that S1, the lowest singlet excited state, be strongly coupled (that is, possess a large oscillator strength) with the ground state. S1 is viewed as a polaron-exciton (exciton associated with a local geometry, lattice relaxation) of intermediate binding, a few tenths of an electron volt [70] [36].

2.2.1 Light Emitting diodes

In order to get the efficient electroluminescence efficient injection of holes and electrons is one of the important factors. There have been efforts towards achieving this by matching work functions of the electrodes with HOMO-LUMO of the polymer used, using charge injection layers and by doping the polymers and mixing the polymer with ionic electrolytes and so on. By using high work function anodes and low work function cathodes matched to HOMO and LUMO of the polymers with reasonable efficient injection of electrons and holes is usually adapted in typical LEDs . The nature of interface between the metal electrode and the active polymer layer, is of prime importance in case of light emitting diodes. Injection and transport of holes and electrons from the metal electrodes to the bulk of the polymer is very critical in light emitting devices [106].

A schematic energy level diagram of a typical matching of the work functions of the metal electrodes with HOMO-LUMO of the polymer for an working organic LED under forward bias is shown in 2.4. LEDs operate due the injection of electrons and holes from negative and positive electrodes, respectively. Electrons and holes capture one another within the polymer, and form neutral bound excited states, excitons. Spin allowed radiative emission (fluorescence) is from the singlet only, and when the exchange energy is large, cross over from triplet to singlet is unlikely, so that triplet excitons do not produce light emission, other than by indirect processes such as triplet-triplet annihilation, or by phosphorescence.

An important parameter related to the electroluminescence of LEDs is internal quantum efficiency η_{EL}. It is the ratio of the number of photons produced within the device to the number of electrons flowing in the external circuit and is given by,

$$\eta_{EL} = \eta_{PL} \cdot \gamma \cdot \chi \tag{2.1}$$

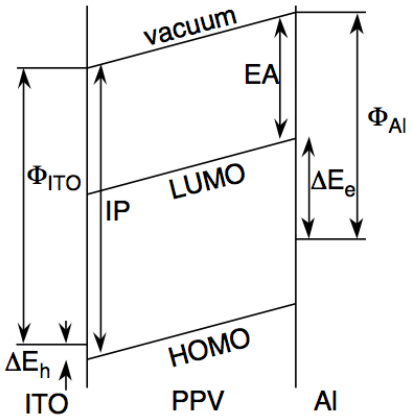

Figure 2.4: Schematic illustration of energy levels and matching of the work function of electrodes used in a single layer, typical polymer light-emitting diode, With permission from reference [40]

where γ is the ratio of the number of exciton formation events within the device to the number of electrons flowing in the external circuit, χ is the fraction of excitons that are formed as singlets, and η_{PL} is the efficiency of radiative decay of these singlet excitons, approximately equal to the photoluminescence efficiency.

The measured external quantum efficiency, η_{ext}, is the ratio of photons emitted from the diode surface to the electrons flowing in the external circuit, and is significantly smaller than η_{EL} because of losses due to total reflection, wave guiding and absorption within the device [111] [2]. Depending on the refractive index of the polymer only a fraction of the emitted photons may be emitted from the surface [136].

2.3 Light Emitting electrochemical cells

Light emitting electrochemical cells on the other hand, are another kind of light emitting device where polymer semiconductors are employed. A blend of polymer electrolytes with semiconducting polymer with energy gap ranges in the visible regime is used [101]. LECs do not require the matching of energy levels with the metal electrodes used. Irrespective of the polymer used, for both holes and electron injection, high or low work function metal electrodes can be used. This is

possible, because of the presence of ions in association with the polymer. On the application of the voltage greater than energy gap of the device, across the device, ions self assemble themselves in the proximity of metal electrodes depending on their polarities due to the injection of charge carriers and eventually reducing the contact resistance.

2.3.1 Operating Mechanism: LECs

An LEC is a mixture of ionic/electronic conductor consisting of a luminescent polymer and a solid polymer electrolyte. When a voltage greater than the energy gap of the polymer divided by the elementary charge, of the polymer semiconductor used, is applied, the luminescent polymer is electrochemically p-doped on the anode side and n-doped on the cathode side. Ions start moving towards the electrodes upon application of the bias and then electrons and holes get injected and in order to ensure the space charge neutrality in the bulk. The light emitting p-n junction is eventually formed, when the expanding p and n doping regions eventually meet within the channel between the electrodes [101].

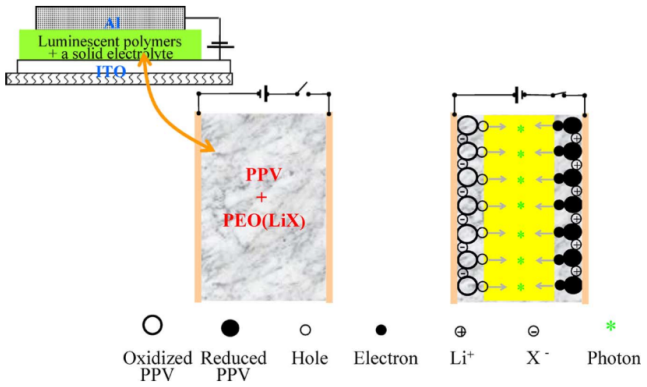

Figure 2.5: Schematic of a typical light emitting electrochemical cell which is a blend of semiconducting polymer with polymer electrolyte and the schematic explaining the working mechanism of the same. With permission from reference [101]

Such in-situ electrochemical doping significantly reduces the bulk and contact resistance in an LECs. High quantum efficiency at low operating voltages ($<$ 4V) are achieved with LECs. During the last decade many researchers have

made a significant contributions towards understanding the operating mechanism and optimization of LECs[135] [107] [118] [112]. Both quantitative[107] and qualitative models[82] have been developed to describe the operating mechanism of LECs.

The operating mechanism of the polymer LECs is quite different from two other important organic/polymer electroluminescent devices: LEDs and electrochemiluminescent (ECL)cells. For the LECs, the formation of the p-n junction depends on redistribution of ionic species (dopants). Once the junction has been formed, the subsequent electroluminescence is a pure electron-hole recombination and radiative decay process that does not require any mass transport. The electroluminescence from LEDs does not concern any ionic species. On the other hand, the luminescence of the ECL relies on ions shuttling between the electrodes where they are oxidized or reduced and the bulk of the electrolyte solution where the oxidized and reduced ions recombine and decay radiatively. The electroluminescence is controlled by the mass transport process[119] [101].

The large spacing planar configuration allows one to study the spatial profile of the dynamic junction by direct imaging. Several studies about the operating mechanism of LEC come from the direct observations[100] [101] [13] [41] [58] and the optical beam induced current measurements[27] of the planar LECs, and also from the electro absorption[42] [45], and alternating current impedance measurements[75] of the sandwich type LECs.

The light emitting junction is a narrow region with width only a fraction of the total spacing between the electrodes. Using the optical beam induced current measurement method, a peak in the built in electrical field was observed at the location of the p-n junction. In the ac impedance study[75], the capacitance of an LEC notably increases when the electrochemical doping process was initiated. The results of theoretical calculations and analysis of the LECs are also in agreement with an electrochemical doping mechanism[12] [135] [118] [107] [82] [112].

However, a recent report by Slinker et al[33] reports the accumulation and depletion of mobile ions near the electrodes creating high interfacial electric fields that enhance the injection of electronic carriers based on probing of the operation of LECs using electric force microscopy on planar devices and theoretical modeling of the same. Another independent report from different group, by Matyaba et al[86] based on the scanning kelvin probe microscopy and optical probing of planar

devices supporting the electrochemical model of the device reported in different group of reports by the Heeger et al [100] [82].

The mechanism and effects of doping in LECs, still far from being fully understood, different groups have been trying to understand the mechanism carefully. One of such report by Reenen et al [127] show that these models are essentially limits of one master model, separated by different rates of carrier injection. Reenen et al demonstrate by using numerical calculations, measured surface potentials and light emission and doping profiles in operational devices that ohmic nonlimited injection case, a dynamic pn junction is formed, which is absent in injection-limited devices.

2.3.2 Electric Field distribution in LECs: Debate

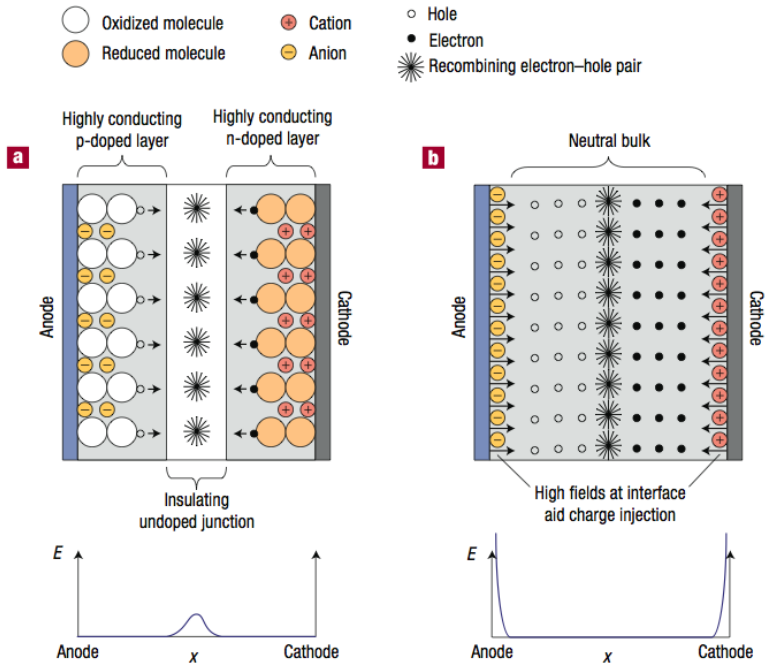

Figure 2.6: The two models proposed, electrochemical and electrodynamic model for LECs operation, with associated spatial distribution of the electric field shown underneath. With permission from reference [24]

On the application of the voltage greater than the energy gap of the polymer divided by the elementary charge results the charge injection and the redistribu-

tion of ions assists the injection of electronic carriers in turn leads to efficient light emission in light-emitting electrochemical cells. However, the operating mechanism of LECs has been controversial, as there is no concurrence regarding the distribution of potential profile or the electric field in these devices.

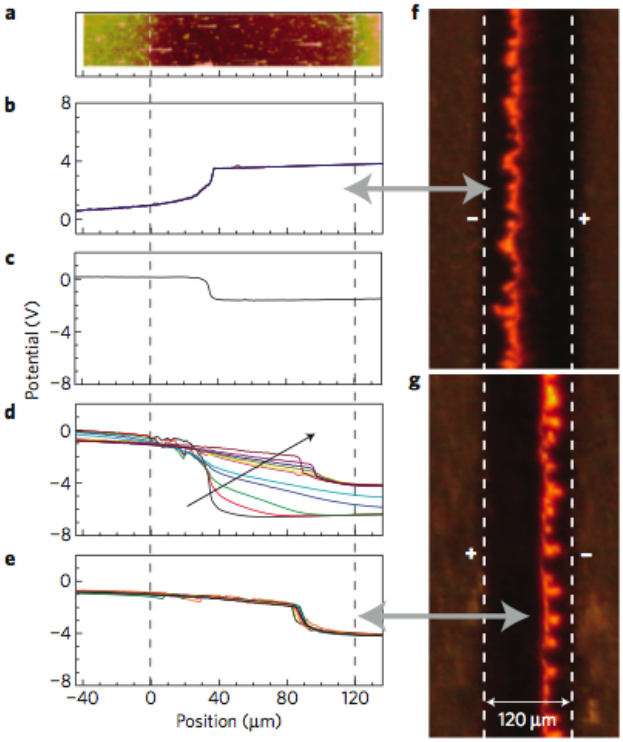

Figure 2.7: Experimental data showing scanning kelvin probe microscopy data along with recombination zone profiles illustrating the formation and reformation of p-n junction in an LECs. With permission from reference [86].

The very first model is is an electrochemical model saying the injection of holes and electrons causes oxidation and reduction of the organic semiconductor close to the anode and cathode, respectively. Counter ions move to compensate the reduced and oxidized molecules, leading to the formation of p- and n-doped layers that extend into the bulk of the device. The high conductivities of the doped regions cause the electrode-organic interfaces to act as low-resistance contacts, allowing easy carrier injection. The radiative recombination of electrons and holes in the middle of the device depletes the charge carriers, leading to the formation of an undoped junction region across which the entire applied bias is dropped.

The later model is known as electrodynamic model stating that under an applied forward bias, a slight redistribution of the ionic charge occurs, leading to an excess of anions and cations at the anode and cathode, respectively. The accumulated ions cause a local enhancement in the electric field and if the density of ions is sufficiently high, leave the bulk of the device virtually field-free. The electrons and holes diffuse through the field-free bulk and meet in the middle of the device where they recombine.

Both models do not doubt the ions assisting the holes and electron injection at the metal electrode contacts. The electrodynamic model says the entire applied potential drops at the thin electrical double layers at the metal electrode and polymer interface, however, the electrochemical model says that the significant fraction of applied potential drops across the light emitting p-n junction.

Both [99] [81] models are supported by experimental data and numerical modeling. Independent works by Demello et al [23] [22], Matyaba et al [86] (figure 2.7 and attempts to the unifying model by Reenen et al [127] and Pingree et al [102] unfolds the mechanisms behind LECs to a greater extent, yet the question seems to remain open.

2.3.3 A comparison: LECs and LEDs

	LEDs	LECs
Active layer	Polymer	Belend of polymer and electrolyte
Thickness of the active layer	Thin	Not sensitive
Anode	High work function	Not sensitive
Cathode	Low work function	Not sensitive
Quantum efficiency	Depends on injection balance	High
Operating Voltage	Varied with thickness	Very low
Power efficiency	Low to moderate	High
Response speed	High	Low
Fabrication process	Complicated	Simple

Table 2.1: A Comparision: LEDs and LECs [119]

LECs offer a number of potential advantages such as low operating voltage, high efficiency and insensitivity to the electrode materials etc as listed in table 2.1. The Quantum efficiency in LECs is not dependent on the injection balance as charges are easily injected[119] due to the presence of ions. Nonetheless, the diffusion coefficients of ions and hence the respective charge transport and the location of the p-n junction formation plays a significant role in determining the quantum efficiency of the devices. In addition to this, there are other drawbacks in LECs such as the phase separation apolar luminescent polymer and strong polar electrolyte, over oxidation of the polymer at higher bias voltages which reduces the lifetime of the devices, and the slow response time of the light emission. Owing to the lack of a clear understanding of the device physics of LECs, these devices are of fundamental interest as they facilitate the exploration of physics involved.

2.3.4 Field Effect Transistors

A typical field effect transistor has three terminals, with an active semiconductor polymer layer and a gate dielectric layer. The source, drain and gate electrodes usually are metal electrodes or conducting polymer inks matched with HOMO, LUMO of the polymer semiconductor used for efficient charge injection. Voltage is usually applied to the drain and gate electrodes and source terminal usually is grounded. The flow of charge carriers (electrons or holes) from the source to the drain is controlled by the voltage applied on gate terminal which affects the size and shape of the conductive channel as shown in figure 2.8. In order to accumulate electrons in the channel positive voltages on both the drain and gate terminals are applied and similarly in order to accumulate holes, negative voltages are applied on drain and gate electrodes.

The number of accumulated charges at the semiconductor-dielectric interface (channel) is determined by the specific capacitance of the dielectric and the gate voltage applied. Nonetheless, the presence of of traps would not allow all accumulated charges to be mobile. This introduces the threshold voltage, which is the minimum amount of the gate voltage that need to be applied in order to fill the traps before the transistor can be switched on. Hence the effective

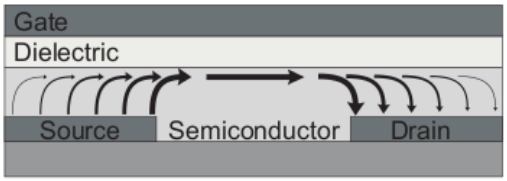

Figure 2.8: Schematic diagram of a typical top gated bottom contact transistor, showing the channel at the semiconductor-dielectric interface through which prominent current flows [136].

gate voltage is $(V_g - V_{th})$ where V_g is the gate voltage and V_{th} is the threshold voltage. Charge trapping is strongly dependent on the semiconductor-dielectric interface. Impurities, built in dipoles and interface states contribute towards the threshold [128].

In a linear regime of the transistor ($V_{ds} \ll V_g$), the current (I_d) through the transistor is directly proportional to V_{ds}. The potential within the channel increases linearly between the source-drain electrodes. When $V_{ds} = V_g - V_{th}$ the current starts to saturate. While the gate voltage is the voltage that controls the accumulation of the charge carriers, the potential difference across the source and drain draws the current due to the accumulated charge carriers. While $V_{ds} = V_g - V_{th}$, the corresponding drain current is the maximum drain current that can be obtained through the channel for the corresponding accumulated charges. This means if V_{ds} is further increased, where $V_{ds} \gg V_g - V_{th}$, the current can not be increased as the number of charge accumulated is defined by corresponding $V_g - V_{th}$.

The current-voltage characteristics of a FET in different operating regimes can be described using gradual channel approximation. The gradual channel approximation means, assuming the rate of variation of the lateral field within the channel is much smaller than the rate of variation of the vertical field and the channel potential is assumed to be a gradually changing as function of position. This is a valid approximation for transistors with long channel lengths [120]. If the specific capacitance of the gate dielectric is C_i, for a given gate voltage (V_g) and threshold voltage (V_{th}) the induced mobile charge density, Q is given by,

$$Q = C_i \cdot (V_g - V_{th}) \tag{2.2}$$

This is when the channel potential is zero. Induced charges depends on the potential along the channel, V_x. Hence,

$$Q = C_i \cdot (V_g - V_{th} - V_x) \tag{2.3}$$

Now, the drain current $I_d(x)$ can be obtained by neglecting the diffusion current,

$$I_d(x) = W \cdot \mu \cdot Q \cdot E(x) \tag{2.4}$$

where $E(x) = dV(x)/dx$ is the electric filed, W is channel width, μ is mobility. The drain current through the channel of length L, can be obtained by integrating the above equation from $x = 0$ to $x = L$, i.e $V(x) = 0$ to $V(x) = V_d$,

$$I_d = \frac{W \cdot C_i}{L} \cdot \mu \cdot \left((V_g - V_{th}) \cdot V_{ds} - \frac{V_{ds}^2}{2} \right) \tag{2.5}$$

In linear regime, where $V_{ds} \ll V_g$, the equation simplifies to,

$$I_d = \frac{W \cdot C_i}{L} \cdot \mu \cdot (V_g - V_{th}) \cdot V_{ds} \tag{2.6}$$

In this regime, the drain current is directly proportional to gate voltage and mobility can be calculated by,

$$\mu_{lin} = \frac{\partial I_d}{\partial V_g} \cdot \frac{L}{W \cdot C_i \cdot V_{ds}} \tag{2.7}$$

In saturation regime, while $V_{ds} = V_g - V_{th}$, the channel is pinched off, and the drain current saturates. In this regime, the saturation current can be calculated using the equation,

$$I_d = \frac{W \cdot C_i}{2L} \cdot \mu \cdot (V_g - V_{th})^2 \tag{2.8}$$

And the saturation mobility can be calculated using the equation,

$$\mu_{sat} = \frac{\partial I_d}{\partial V_g} \cdot \frac{L}{W \cdot C_i \cdot (V_g - V_{th})} \tag{2.9}$$

Thus, using the gradual channel approximation, current-voltage characteristics of an FET in both linear and saturation regimes can be described and the

corresponding mobility values can be calculated.

2.3.4.1 Charge Transport Models for Organic Semiconductors

Though organic semiconductor polymers posses most of the semiconducting properties of inorganic semiconducting materials, they are distinctly different. The charge transport in organic semiconductor polymers for example is a matter of debate till date. Whether it is a band-like transport in these materials or hopping mechanism is involved is for example not concluded. Several models have been proposed to explain the charge transport mechanism in organic semiconductors. Although we do not make an attempt to review all proposed models, in this section briefly mentions a few.

A band-like transport theory has been proposed to explain the charge transport in certain semiconductors. Coupling between the conjugated molecules is due to weak van-der-Waals forces and π-π^*-interactions and is easily broken by phonons and lattice disorder. Band-like transport indicated by an increase of mobility with decreasing temperature (phonon-scattering) has been reported with high purity organic single crystals such as naphthalene[115], anthracene[67] rubrene and pentacene[103] [95]. However, most conjugated organic semiconductors possessing high degree of disorders rule out the band-like transport.

A hopping model for a doped inorganic semiconductor at low temperatures that explains the temperature dependence of the mobility[87] was developed by Miller and Abrahams. In order to address the hopping over larger distances (larger compared to distance between the neighboring sites) this model was further extended by Mott[90]. This is called variable range hopping model(VRH), where carriers can hop over longer distances with low activation energy or short distances with a high activation energy.

Bässler disorder model takes into account of disorder associated with conjugated polymers. Variation in conjugation lengths and interaction energies leads to a distribution of transport sites rather than delocalized energy bands. In this model, the temperature dependence of the mobility is not Arrhenius-like but follows $\ln \mu \propto T^{-2}$.

In spite of many different proposed models, the quest for a single model that

explains charge transportation universally in organic semiconductors remains an active research area.

2.3.4.2 Light Emitting Field effect Transistors

Light Emitting field effect transistors are the light emitting diodes with the modulation of gate voltages. In addition to the transistor action there exists the electroluminescence as well. Achieving the electron transportation in organic semiconductors with right choice of metal electrodes for the charge injection and the right dielectric leading to the clean semiconductor dielectric interface has been difficult until recently [17]. First ever reported light emission [56] in transistors therefore were unipolar light emission in these devices where the prominent hole transportation overtakes the limited or no electron transportation and the recombination zone occurs in the proximity of the electron injecting electrode.

The unipolar light emitting transistors hence suffer from low external quantum efficiency due to the unbalanced hole and electron pairs. Moreover, since the location of the recombination zone is in the vicinity of the electron injecting electrode, absorption of the emitted light from the metal electrodes also contributes towards a reduced light emission out of the device.

A comparable hole and electron mobility in a same transistor however has been achieved in recent years [137] [17] and because of the comparable speed of the charge carriers, it is possible to see the recombination zone in the middle of the channel. Moreover, with gate and drain source voltage variation favoring either more holes or electron transport, it is also possible to move the recombination zone in these devices from one electrode to the electrode. These devices are interesting as those are in fact transistors which can be used as switches meanwhile, as light emitting diodes as well. Since the location of the recombination zone can be moved throughout the channel, and it's possible to have it in the middle of the channel, there is no absorption of the light emitted by the charge injecting metal electrodes. Figure 2.9 shows the schematic of ambipolar light emitting transistors. Due to the comparable mobility in holes and electrons, and also, the light emission happens in the ambipolar regime where the current through the channel is less, these light emitting field effect transistors possess high external

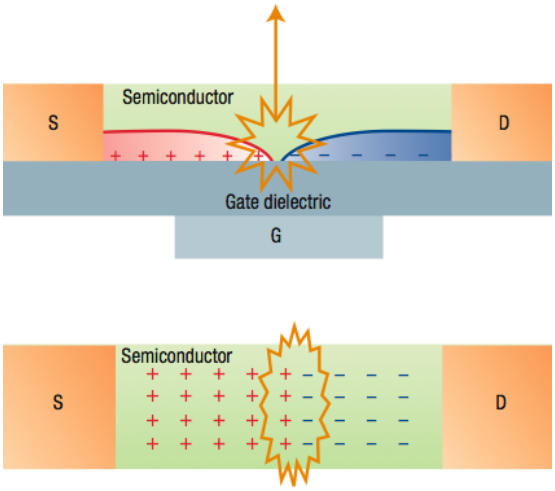

Figure 2.9: Scheme of a light-emitting field-effect transistor. a, Side view. b, Top view. In a simple model, the device can be thought of as a sort of two-dimensional forward-biased p-n junction. Electrons and holes are injected from the drain (D) and source (S) contacts and recombine within the channel in a position controlled by the gate (G). With permission from reference[91]

quantum efficiency. However, the operating voltages of these devices are high such as 40 -100V. This causes a serious shortcoming from the application point of view.

2.4 Low Voltage Field Effect Transistors

2.4.1 Polymer Electrolyte Field Effect Transistors

Gate dielectric plays significant role in determining operating voltage of a transistor. This is due to the capacitance that controls the charge accumulation at the semiconductor- dielectric interface. In addition to controlling operating voltage of a device, the clean interface between the dielectric and semiconductor is of prime importance since this plays a significant role in charge transportation which mostly happens in the very proximity of the interface.

Capacitance of the dipole polarization driven traditional gate dielectrics such as SiO_2 or benzocyclobutene (BCB), poly(ethylene) (PE), poly(methyl methacrylate) PMMA, poly (4-vinylphenol) (PVP) etc depends on the thickness of the

layer. Capacitance, $C = \epsilon.\epsilon_0/d$ where d is the thickness of the dielectric layer and ϵ is the dielectric constant of the material. In order to get high capacitance ultra thin dielectric layers are necessary. The capacitances of these systems approach 1 $\mu F/cm^2$, which compares favorably with typical ceramic dielectrics; for example, a 150 nm thick layer of SiO_2 has a capacitance of 20 nF/cm^2. Solid polymer electrolytes offer a different approach to the gate dielectrics due to the the electrical double layer capacitance[71] which is independent of the thickness of the layer and possess high specific capacitance. The higher the specific capacitance at the interface, the higher is the charge accumulation at the interface, $Q = C_i.(V_g - V_{th})$ where, C_i is the capacitance per unit area of the gate dielectric and V_g is the gate voltage applied and V_{th} is the threshold voltage for the charge accumulation. Thus having the high interface capacitance with high dielectric constant dielectrics would accumulate larger charge carrier concentration for small voltages.

High operating voltages are due to the small specific capacitance of the gate dielectrics used. In order to increase the capacitance at the polymer and dielectric interface, many different approaches have been made[53] [28] [4] [69] [98]. With the traditional dipole polarization driven capacitance, the key in order to get the high capacitance is to reduce the thickness and hence increase the capacitance. Polymer electrolytes offer a solution, however the capacitance is driven by a different sort of mechanism (refer figure 2.10) , which does not depend on the thickness of the dielectric layer but depends on Debye length. Electrical double layer(EDL) capacitance is the capacitance at the interface due to the ions layer at the dielectric layer and corresponding layer of the charges in semiconductor which is independent of the thickness of the dielectric layer[71].

Several groups have demonstrated that solution processable solid polymer electrolytes[76], such as polyethylene oxide (PEO) with dissolved Li salts, can be used as gate insulator materials in transistors[60] [61] [52] [98] [110] [121] These systems have even larger specific capacitances(10 $\mu F/cm^2$). PEO/LiClO_4 films, for example, have been used to gate organic single crystals, organic semiconductor thin films, and carbon nanotubes.

High on currents and low voltage operation are achieved using PEO/LiClO_4, however a significant disadvantage is the relatively slow polarization time of this

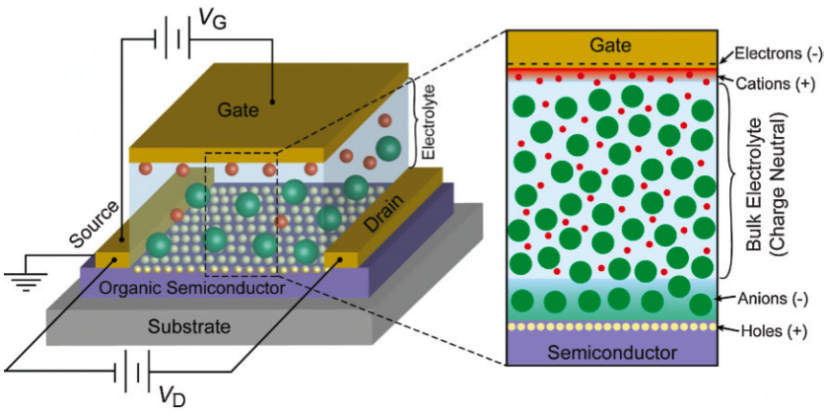

Figure 2.10: Schematic showing the electrical double layer capacitance formation at the semiconductor dielectric interface in a polymer electrolyte or ionic liquid/gel gated field effect transistors on the application of gate voltage. With permission from reference [97]

solid electrolyte. The polarization is limited by ionic conductivities, typically on the order of $10^{-4} - 10^{-5}$ S/cm. For polymer electrolyte gated transistors, the slow polarization time results in low transistor switching frequencies, usually a few hertz, greatly limiting potential applications.

2.4.2 Ion Gel Gated Field Effect Transistors

Ionic liquids, on the other hand are another interesting class of materials which resolve the slow switching issues due to their high ionic conductivities, while retaining the high specific capacitance advantage, similar to solid polymer electrolytes (specific capacitance of ion liquid or ion gel dielectrics is comparatively higher than typical polymer electrolytes).

Ion gels are the mixture of block copolymers (which helps gelation) with ionic liquids. Unlike solid polymer electrolytes, which are obtained by the dissolution of salts by ion-coordinating polymers [44], gel electrolyte is formed by gelation of block copolymer into a room temperature ionic liquid. H. Cho et al have investigated ion gels primarily based on ionic liquids from imidazolium family with triblock copolymers for gelation [16] and have shown that the gelation of the ionic liquid with triblock polymer is possible without scarifying the high ionic conductivities of the ionic liquid [16]. Hence the high capacitance such as 41

$\mu F/cm^2$ at 10 Hz[72] was obtained, that typically is far greater than an inorganic or organic dielectric layers. This further allow us to work with gel materials as opposed to liquids without loosing the ionic conductivity significantly[34]. These ion gels are also thermoreversible due to the micellaisation of block co polymers ions move freely in confined channels[77].

Faster response time and high specific capacitance and hence low operating voltages is of the primary attraction in using ion gels as gate dielectric materials. There has been different reports of p-chanel, n-channel and ambipolar[117] [139] FETs using different kinds of ionic liquids and ion gels as gate dielectric materials.

Nonetheless, there were not any reports of the light emission form polymer ion gel gated transistors which would be very interesting from the application point of view due to their low voltage operations compared to LEFETs and LEDs which operate at slightly higher side of the voltage range. Moreover, when a device is light emitting, the fraction of emitted light is usually absorbed by the thin gate dielectric layer and the gate electrode. Even though, the dielectric layer and the gate electrodes are thin enough, they would surely be contributing towards the absorption of light to some extent. Ion gels on the other hand are transparent[30]. So the absorption factor due to the dielectric layer can easily be removed. Also, due to the virtue of ion gels, the electrical double layer capacitance results due to the movement of ions and this allows us to have the gate dielectric elsewhere. The gate electrode does not necessarily need to be on the top of the channel. It can be either offset from the channel or even, it can be on the same plane as source and drain electrodes provided the polymer is patterned suitably as we discuss in chapter 4.

Hence in this work, the motivation was to get the light emission in the transparent ion gel gated, lower voltage operating polymer semiconductor transistors. However, when there is the presence of ions in dielectric layer, the system is quite complicated compared to the dipole polarization driven traditional dielectrics based FETs. This further necessitates to study the mechanisms behind the light emission in these systems as well.

2.4.2.1 Electrostatic and Electrochemical Operation

Such exceptionally high capacitance is believed to come from the diffusion of mobile ions to the dielectric/organic semiconductor interface on the application of a gate voltage, resulting in the formation of an electrical double layer with nanometer thickness. This high capacitance is the cause behind very low gate voltage in switching a FET from the off-state to the on-state, as reported by a number of groups for FETs based on organic single crystals [125] and small molecule or polymer [72] semiconductor thin films.

From the application point of these devices, due to the proven advantages of these dielectric materials, the operating mechanism is not of prime importance. However, the fundamental question of interest is whether the ions stopping right at the polymer semiconductor and gate dielectric interface to a high degree of accuracy or not. From the study of the charge transportation under the high charge density in FETs, it is desired that the polymer semiconductor be at it's pristine state throughout. Hence the fundamental question of interest that concerns is the mechanism of the charge injection, whether gating is purely electrostatic or to some extent electromechanical too.

Electrostatic operation regime is the regime where the polymer semiconductor is free of ions, absolutely. The electric double layer formation at the interface would lead to an electrostatic operation of the FET whereas, if on the application of the gate voltage, rather than ions stopping their movement completely at the interface, if some of them penetrates in to the polymer layer, the system becomes electrochemical.

During a pure electrostatic operation, the charge injection at the metal electrodes happen the usual way, not assisted by any external factors, but purely based on the HOMO-LUMO matching of the polymer with the work function of the metal electrode used. Whereas in case of electrochemical contribution, few ions which get into the polymer layer assemble next to the respective electrodes and in turn help the charge injection. The incorporation of ions near the polymer backbone also changes the transportation of charge carriers through the semiconductor compared to its pristine counterpart.

Reports by Kaake et al [63] [64], Mills et al [88] for example are the reports that

question the possibility of pure electrostatic operation in such gel gated or polymer electrolyte gated polymer transistors. While high gate voltages cause the ion penetration into the active polymer semiconductor layer, applying smaller gate voltages for a longer duration of time would also lead to the same effect [73].

Nonetheless, it is indeed interesting to unfold the working mechanisms behind these special dielectric gated transistors, especially when the transistors are light emitting. Unfolding the working mechanism can solve fundamental questions concerning the polymers with association of ions which might lead to enhanced properties similar to doped polymer semiconductors. While a pure electrostatic operation is desired in order to study the charge transportation mechanism in a system, the enhanced optical and electrical properties of the doped polymer semiconductor can not be overlooked [74] and are of great significance.

Chapter 3

Materials and Experimental Methods

In this chapter we briefly discuss the polymers, dielectrics and ion gel materials used in this work. The chapter also provides a detailed description of fabrication process employed for preparing the semiconductor devices used in this study. We also document the methods and apparatus used for the characterization and measurements of the fabricated devices.

3.1 Materials

3.1.1 Organic Semiconducting Polymers

Organic polymers having energy gaps corresponding to the visible region of the electromagnetic spectrum, such as poly(9,9'-dioctyl fluorene-co-benzo thiadiazole) (F8BT, E_g = 2.6 eV), poly(9,9-dioctyl fluorene-alt-bithiophene) (F8T2, E_g = 2.4 eV), poly(9,9-dioctyl fluorene)-2,7-diyl-alt-[4,7-bis(3-hexyl thiophen-5-yl)-2,1,3-benzo thiadiazole]-2',2"-diyl) (F8TBT, E_g = 2.2 eV) and poly(2-methoxy-5-(3,7-dimethyl octoxy)-p-phenylene vinylene) (OC1OC10-PPV, E_g = 2.2 eV) are used in this work. The chemical structures of these polymers are shown in figure 3.1.

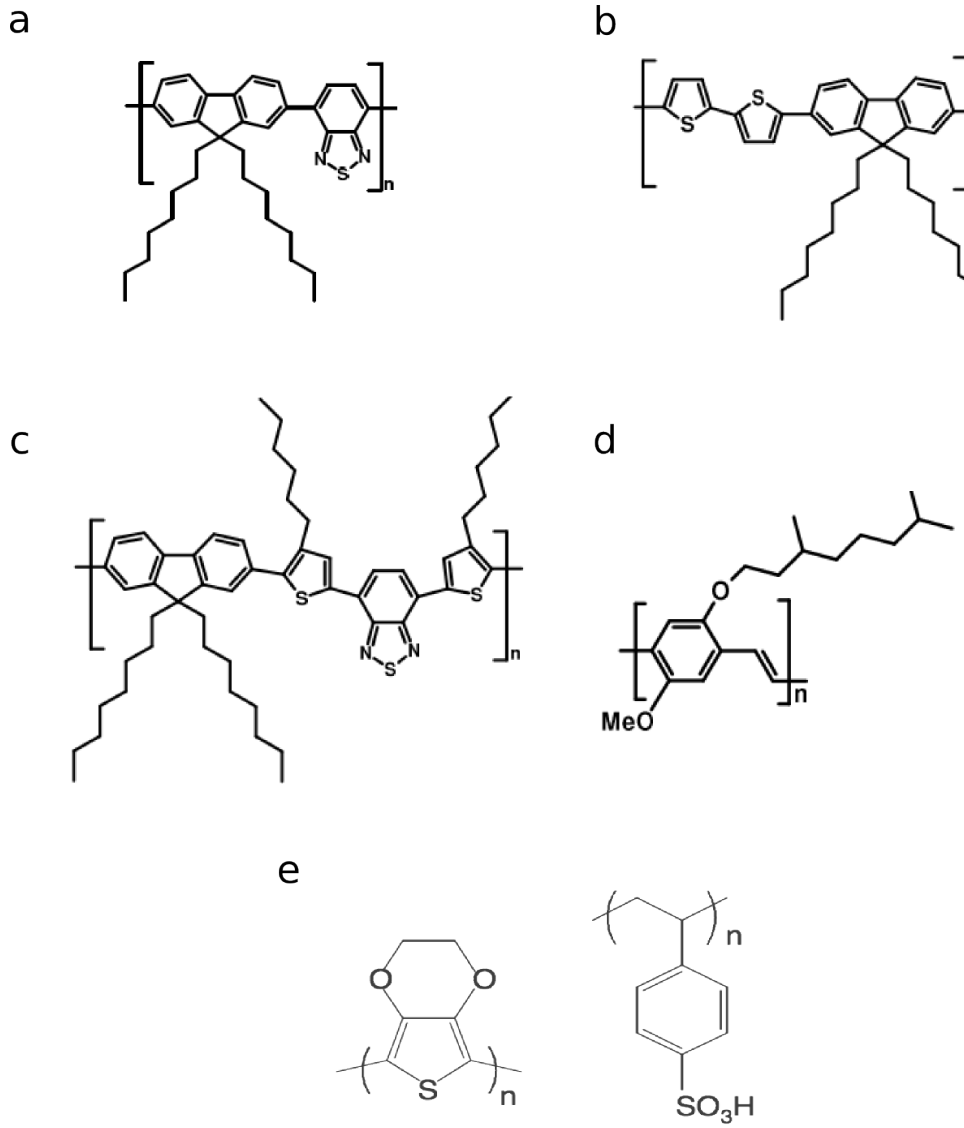

Figure 3.1: Molecular structure of (a) poly(9,9'-dioctyl fluorene-co-benzo thiadiazole) (F8BT), HOMO: 5.9 eV, LUMO: 3.3 eV. (b) poly(9,9-dioctyl fluorene-alt-bithiophene) (F8T2) HOMO: 5.5 eV, LUMO: 3.1 eV. (c) poly(9,9-dioctyl fluorene)-2,7-diyl-alt-[4,7-bis(3-hexyl thiophen-5-yl)-2,1,3-benzo thiadiazole]-2',2"-diyl) (F8TBT) HOMO: 5.4 eV, LUMO: 3.2 eV (d) poly(2-methoxy-5-(3,7-dimethyl octoxy)-p-phenylene vinylene) (OC1OC10-PPV) HOMO: 5.0 eV, LUMO: 2.8 eV (e) the conducting polymer poly(3,4-ethylene dioxythiophene) poly(styrene sulfonate (PEDOT:PSS) which can be used as gate electrode.

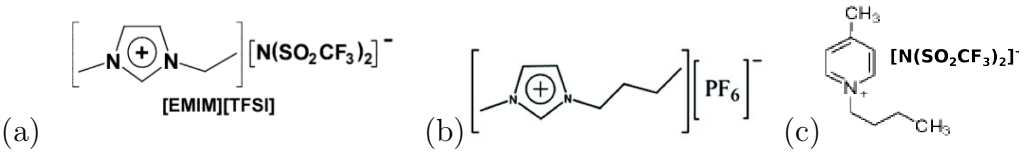

(a) (b) (c)

Figure 3.2: (a) Ionic liquid 1-ethyl-3-methyl imidazolium bis(trifluoromethyl sulfonyl)imide (EMIM-TFSI) (b) 1-butyl-3-methyl imidazolium hexafluorophosphate (BMIM-PF6) (c) 1-butyl-4-methyl pyridinium bis(trifluoro methanesulfonyl)imide (BMPY-TFSI)

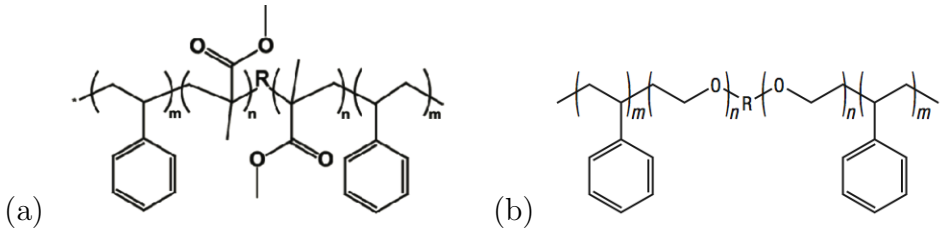

(a) (b)

Figure 3.3: Triblock copolymers used for gelation with ionic liquids (a) poly(styrene-block-methyl methacrylate-block-styrene) (SPMMA) (b) poly(styrene-block-ethylene oxide-block-styrene) (SOS).

3.1.2 Gate Dielectrics

Ionic liquids 1-ethyl-3-methyl imidazolium bis(trifluoro methyl sulfonyl) imide (EMIM TFSI) 1-butyl-3-methyl imidazolium hexa fluoro phosphate (BMIM-PF6) and 1-butyl-4-methyl pyridinium bis(trifluoro methane sulfonyl)imide (BMPY-TFSI) are used as gate dielectrics. In order to get the gels of these ionic liquids tri block co-polymers, either poly(styrene- block- ethylene oxide- block- styrene) (SOS) with PS block molecular mass $10 kgmol^{-1}$ and PEO block with $40 kgmol^{-1}$ or poly(styrene- block- methyl methacrylate- block- styrene) (SPMMA) purchased from Polymer Source Inc are used. The chemical structures of ionic liquids and tri-block copolymer used are shown in figure 3.2 and figure 3.3 respectively.

3.2 Fabrication Process

Transistors were fabricated on cleaned (sequential ultrasonic treatment in H2O, acetone and isopropyl alcohol and oxygen plasma) glass substrates. Source and drain electrodes defining the channel length of 40 μm and width of 2cm were pat-

terned by photolithography. The thickness of gold for source and drain electrode was about 30-35 nm.

3.2.1 Photolithography, Evaporation and Lift off

Two photoresists were used. LOR 5B and Shipley 1813. This results in a slight undercut of the photoresist to prevent a continuous layer of gold being deposited over the edge onto the substrate. LOR 5B was spin coated on oxygen plasma treated clean glass substrates (4000 rpm, 30 s, acc 20) and then annealed for 5 minutes at 190^0 C. This is followed by spin coating Shipley photoresist with same spin rates and annealing samples at 120^0C for 2 minutes. This is followed by exposing the UV through the suitable mask with standard power for about 14 seconds followed by developing the samples for about 25- 27 seconds in developer followed by cleaning using distilled water and oxygen plasma for about 2-3 minutes with 250 W power, to remove any photoresist from the contact area.

This is followed by thermal evaporation of chromium (for adhesion, 0.7nm thick) and gold (30-35nm thick) with the vacuum levels of 10^{-6} mbar. The lift off was done using N-Methyl-2-pyrrolidone (NMP), which then is followed by cleaning the substrates in NMP, acetone and IPA and oxygen plasma in that order.

Polymer solutions with suitable concentrations (for example F8BT 4mg/ml of anhydrous xylene for film thickness of approximately 40 nm (1000 rpm spin speed)) were then spin coated on the photo-lithographically patterned substrates in inert atmosphere. The polymer film was annealed at 290^0C for about 30 minutes and then quenched to room temperature to get the polycrystalline F8BT films and to remove traces of any solvent, inside the glove box. Before spin coating the gel solution, the annealed polymer layer was kept in the glovebox overnight to make sure that F8BT is at room temperature and in its solid form in order to avoid the possible mixture of the polymer with ion gel solution. Further, an orthogonal solvent is used for ion gel solution to avoid the mixing of two layers.

Ionic liquids were purchased from sigma Aldrich. Tri block copolymers, poly (styrene- block- ethylene oxide- block- styrene) (SOS) or poly(styrene- block- methylmethacrylate- block- styrene) (SPMMA) were purchased from Polymer

Source Inc. Ionic liquids and triblock copolymers were used as received without any purification. The ion gel solution (triblock copolymer: Ionic liquid: Solvent :: 0.7 : 9.3: 90 wt %) in orthogonal solvents, anhydrous acetonitrile or ethyl acetate, was spin coated on the top of dry, room temperature, polymer film of thickness $\approx$ 40 nm and annealed to 70^0C for about 15 hours. Conductive polymer ink PEDOT: PSS was used for gate electrode. PEDOT:PSS from Baytron is used as received. The device is exposed to air for 2-5 minutes on a pre heated hot plate for PEDOT printing to remove the water from the PEDOT. The device was then annealed at 70^0C for 15 hours, in the glovebox. Similarly, gel solutions (for example, triblock copolymer: Ionic liquid: Solvent to 0.7 : 9.3: 90 wt %) in orthogonal solvent (to F8BT), (anhydrous acetonitrile) were spin coated on well dried polymer layer.

3.3 Top Offset Gate, Bottom Contact Transistors

For the top gate, either offset gold electrode (60 nm or more thick) or PEDOT:PSS drop cast electrodes were used. In case of gold electrodes, the device is not exposed to air during the entire process whereas with PEDOT:PSS gated devices, the device was exposed to air for about 2-3 minutes in order to dry the PEDOT:PSS outside the glovebox. There has not been any difference observed in hole accumilation in Au gated or PEDOT:PSS gated devices. Nonetheless, FETs did not work well in n-type, electron accumulation mode with positive gate voltage with the devices with Au top electrodes without any exposition to air at any stage. Moreover, from the p-channel point of view, thick PEDOT:PSS drop casted electrode gated devices reproducibility is higher than the gold gate electrode, as the surface of the gel layer is very rough and usually it requires a extremely thick evaporated gate electrode(refer figure 4.2 and figure 4.3)

Without any surface modification, with top offset gate, bottom contact gold electrodes, we get clean hole transportation (p-channel) transistors with ion gel dielectrics.

In order to enhance the electron solution processed [49] ZnO patterned modified

gold surfaces were used.

3.4 Morphology and Thickness

3.4.1 Atomic Force Microscopy

Thin films of the polymers were spin coated on Si/SiO_2 substrates with the same conditions that applied with real devices. Atomic Force Microscopy (AFM) in tapping mode with DimensionT M 3100 scanning probe microscope (Digital Instruments) was used to study the morphology of the films.

3.4.2 Profilometry

Dektak Surface Profiler was used obtain the thickness of the polymer film or the metal electrode thickness on the substrates. A homogeneous surface of polymer film was scratched using the cocktail stick and the height of the film was thus measured.

3.5 Electrical Characterization

A Semiconductor Parameter Analyzer (SPA) Agilent 4155B was used for electrical characteristics. The SPA was controlled by standard Labview software from National Instruments, interfaced with computer using general purpose interface bus cable. Current probes which were connected to device using standard x,y,z control probes with sharp needles for connection were used. The devices were tested in nitrogen glovebox.

3.5.1 Capacitance Measurements

Capacitance measurements were done using HP 4192A Impedance analyzer (5 Hz to 13 MHz) inside the glovebox both as a function of frequency and voltage controlled by the Labview software. The applied ac modulation bias amplitude used was 100 mV.

3.5.2 Vacuum Measurements

Vacuum measurements were done under the vacuum of 10^{-6} mbar in Desert Cryogenics TTP4 probe station using Agilent SPA 4155B semiconductor parameter analyser. Before doing the measurements, the device was left under the vacuum overnight, in order to dry any moisture present. There has not been significant difference in transistor characteristics under vacuum compared with the same under nitrogen atmosphere.

3.5.3 Low Temperature Measurements

Low temperature experiment was carried out in order to see, until what temperatures the modulation in the gate voltages can be seen. Since the capacitance is due to the movement of ions, once the temperature falls below the glass transition of the ion gel, we can not get the high capacitance at the semiconductor and gel dielectric interface. Transistor measurements at low temperatures were carried out under the vacuum of 10^{-7} mbar vacuum in Desert Cryogenics TTP4 probe station. Liquid nitrogen flow and controlled stage heater together were used to control the temperature. The transistor characteristics were recorded using Agilent SPA 4155B at each stabilized temperature values till we stop seeing the gate modulation which is about 230 K.

3.6 Electroluminescence Studies

Electroluminescence intensity measurements were done using a Hamamatsu S1133-01 silicon photo diode, with sensitivity of 0.3 A/W around $\lambda = 560$ nm under reverse bias (3V) and directly holding the photodiode on top of the light emitting device. The dimensions of the photodiode matched well with the dimensions of the device.

3.6.1 Calculation of the External Quantum Efficiency

External quantum efficiency of a light emitting device is the ratio of the number photons of a given wavelength emitted to the number of electrons flowing through

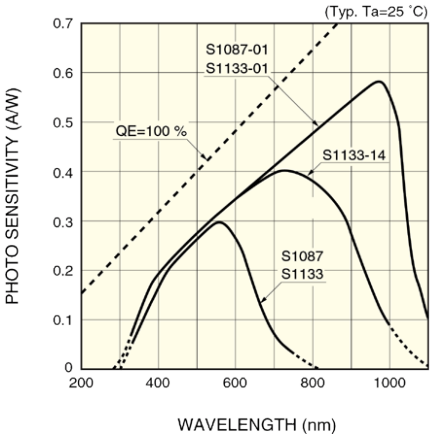

Figure 3.4: Graph showing the photosensitivity with wavelengths for photodiodes [25]

the external circuit. EQE values were calculated from the measured values of the photocurrent due to the electroluminescence and the drain current values, while taking into the account of photo sensitivity of the photodiode used (0.3A/W). Taking into account the photo sensitivity of the diode, the light output,

$$P = I_{ph}(A)/0.3(A/W) \tag{3.1}$$

which represents the wavelength integrated detected light power. $E = hc/\lambda$, is the energy of the emitted photon with wavelength λ, where c is the velocity of the light and h is the Planck constant. The ratio of the light output and the energy of photons, P/E is the number of the photons emitted (N). Since the electroluminescence spectrum is continuous P/E must be weighted with the normalized EL spectrum, $EL_{norm}(\lambda)$ and integrated over all wavelengths in order to calculate the total number N of emitted photons per second.

$$N = \frac{P \int \lambda EL_{norm}(\lambda) d\lambda}{hc \int EL_{norm}(\lambda) d\lambda} = X.P \tag{3.2}$$

Number of electrons per second is given by the ratio of the source drain current with elementary charge I_d/e. Therefore the external quantum efficiency (EQE) is,

$$\eta_{ext} = \frac{N}{I_d/e} = X \frac{P}{I_d/e} \tag{3.3}$$

Using the peak normalized EL spectrum we can calculate the value of X. Taking into account also the sensitivity of the photodiode (figure 3.4)[25], the external quantum efficiency can be simplified to

$$\eta_{ext} \approx 1.5377 \times \frac{I_{ph}}{I_d} \tag{3.4}$$

The external quantum efficiency values are calculated using the above simplified equations, based on the photocurrent, I_{ph} and drain current, I_d of the device[14].

3.6.2 Photoluminescence and Electroluminescence Spectra

Photoluminescence spectra of polymer films were measured in a nitrogen purged integrating sphere at room temperature by excitation from an argon ion laser.

Electroluminescence spectra were recorded using an Ocean Optics HR4000 spectrometer. Images and videos were recorded using a digital camera. All measurements were done in nitrogen atmosphere.

3.6.3 Variation of EL with voltage

In order to see whether the recombination zone of the light emitting device moves with voltages, the whole set of measurements were video recorded using ULead video studio software interfaced with the charge couple device camera with single single objectives directly attached to the camera (20x, 50x).

3.6.4 Recombination Zone Profiles

Recombination zone profiles are obtained by analyzing the reference images and images taken while the devices are emitting light. Origin Pro data analyzing software is used to analyze the pixels of images and hence to analyze the exact location of the recombination zone.

3.6.5 UV-illumination for Doping Zone Studies

Fluorescence probing of the working device was done under nitrogen atmosphere, with excitation from UV-illumination on the working device in a chamber with constant purging of nitrogen, under the microscope, at room temperature. An Olympus BX60 microscope equipped with a UV lamp to excite fluorescence was used to take fluorescence images.

3.7 Charge Modulation Spectroscopy Studies

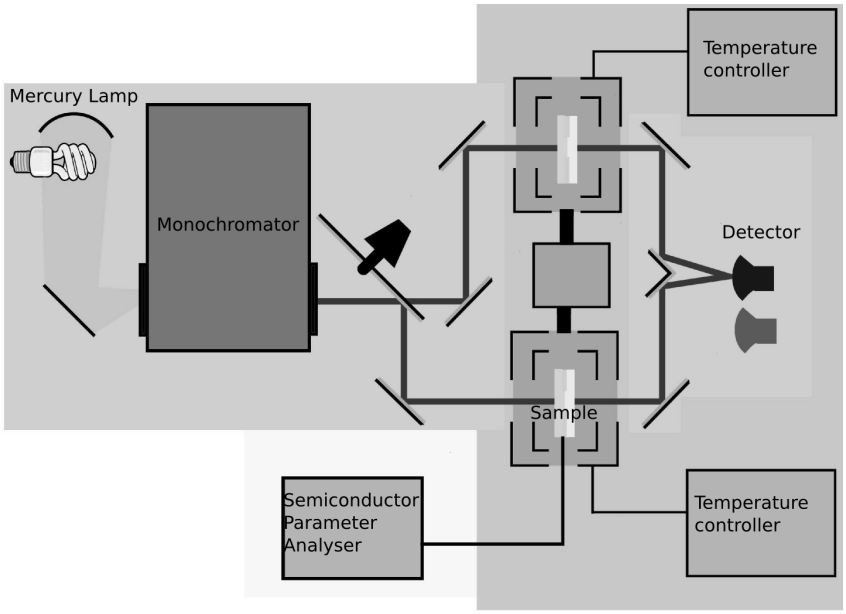

Figure 3.5: (a) Shchematic diagram of the UV-Vis spectro photometer.

The optical spectroscopy measurements were performed using a Cary 6000i double beam spectro photometer (wavelength range 175 nm to 1800 nm)[26] equipped with a controlled atmosphere sample holder. A Keithley 2612 dual channel source measure unit was used to bias the transistor while taking the absorption spectra. Figure 3.5 shows the schematic of the spectro photometer.

Agilent Cary 6000i is a double beam spectro photometer which enables to put a reference sample in another sample holder, howerver, in our experiments only

one of the sample holders was used while the other was left empty. Measurements were done with typical offset gated device with source and drain electrodes grounded and voltage applied to the gate electrode. The measurements were done in-situ in nitrogen atmosphere or in vacuum while the sample holder was maintained at 300K.

Chapter 4

Ion Gel Gated Field Effect Transistors

4.1 Introduction

Ionic liquids[122] [3] [77] and ion gels[16] are an interesting class of dielectrics materials in organic semiconductor transistors. Ion gel or liquid gated single crystals[94] [93] [125] and polymer semiconductor[73] [15] transistors with high carrier mobilities and low voltage operation have been reported. Recent reports of hole[72] [15], electron[126] and ambipolar[66] charge transport with different semiconductor materials and ion gel dielectrics, makes these transparent, environmentally friendly, high capacitance dielectric materials even more versatile.

The ion gel gated field-effect transistor (FET) system could be an ideal system to study the charge transport physics under high charge carrier density[96], provided that the transistor operates in an electrostatic mode due to the electric double layer[97] at the semiconductor and gate dielectric interphase. Nevertheless, the possibility of the penetration of ions from the dielectric material to the organic semiconductors layer on the application of the gate voltage makes the system complicated. There have always been debates[63] [88] about the penetration of ions into the polymer layer depending on the magnitude of the gate voltage[73] and the measurement conditions whenever ion gels or polymer electrolyte systems are used as dielectric material.

Whether the transistor is operating in an electrostatic or electrochemical mode determines the interpretation of measurements and the device physics. For example, in the electrochemical mode the photoluminescence of the organic semiconductor is quenched even in the bulk[57] and the injection of the charge carriers at the source-drain contacts is enhanced[119]. In pure electrostatic operation, the organic semiconductor remains in its pristine state and the charge carrier mobility can be calculated in linear and saturated regimes using the standard field effect transistor equations[137]. Having the ions in dielectric layer with the possibility of the penetration of ions to the organic semiconductor layer on the application of the gate voltage complicates the interpretation as the bulk ion concentration is generally not known.

Due to the low voltage operation and high current densities achievable with ionic liquid or polyelectrolyte gated FETS, they are also of interest for the realization of high performance light-emitting field-effect transistors. It remains to be demonstrated that they can be operated in an ambipolar mode where electron and hole accumulation layers can be formed simultaneously in different regions of the channel[66] and that high electroluminescence efficiencies can be achieved in the recombination zone between these two accumulation layers. A potential application of such high current density LFETs could be in electrically pumped organic laser. In this respect, transparent ion gels, which also offer the flexibility of having the gate electrode not necessarily on top of the channel[15], present another key advantages over other traditional dielectric materials.

However, the possibility of penetration of ions from the dielectric layer to the polymer layer on the application of gate voltage also leaves the possibility of the device operating in a mode that is more akin to that of a light emitting electrochemical cell (LEC)[119][113] than that of an electrostatically gated unipolar or ambipolar light emitting FET.

In this chapter, we study ion gel gated semiconductor devices in the following configurations and report their characteristics.

- Ion Gel Gated F8BT Transistors
- Ion Gel Bilayer Devices

In this chapter, we report light emission from an 1-ethyl-3-methyl imidazolium

bis(trifluoro methyl sulfonyl)imide/ poly(styrene- block- ethylene oxide- block-styrene) EMIM-TFSI/SOS ion gel gated poly(9,9'-dioctyl fluorene-co-benzo thiadiazole) F8BT polymer semiconductor p-channel transistors. We distinguish two separate regimes, one in which the drain source voltage (V_{ds}) is well below the energy gap (E_g/e) of the polymer (where e is the elementary charge), where the device behaves as a stable FET with a well defined current saturation regime, and the other when the $V_{ds} > E_g/e$ the current starts to increase rapidly where we observe corresponding light emission from the channel.

Based on the increasing drain current at constant V_{ds} and V_g values in the output characteristics and large hysteresis in transfer characteristics of the transistor, we investigate the role of ions behind this light emission carefully. Using the charge modulation spectroscopy (CMS) we study the gate voltage dependent ion diffusion from dielectric layer to the polymer semiconductor layer, which increases the charge accumulation dramatically. We see a clear gate voltage dependence of negative ion ($TFSI^-$) diffusion into the polymer layer under hole accumulation (negative gate voltages) which increases with increasing gate voltage.

We do not see a clear evidence for gate voltage dependent diffusion of $EMIM^+$ ions under the electron accumulation regime which is consistent with the fact that we do not observe clear electron transport with this system and the location of the recombination zone is in the proximity of the electron injecting electrode.

Moreover, two terminal bilayer devices (without any gate voltage) emit light at room temperature, with similar increase in the current values and corresponding light emission in $V_{ds} > E_g/e$ regime. In this planar devices, without the third modulating terminal (gate terminal), the potential difference between the source and drain electrodes helps ion displacements and diffusion which eventually lead to light emission similar to the work by Sandstrom et al.[113] at high temperatures. These results independently suggest that ion-gel gated FETs operate akin to planar bilayer LECs when $V_{ds} > E_g/e$.

4.2 Ion gel Gated F8BT Transistors

We study ion gel gated transistor devices with F8BT as the semiconductor material and a EMIM-TFSI/SOS ion gel as the dielectric material. The devices were

fabricated by spin coating the semiconductor and the ion gel layers as described in chapter 3 with a photolithographically patterned channel length of 40 μm and width of 2 cm. The thickness of gold for source and drain electrode was about 30 nm.

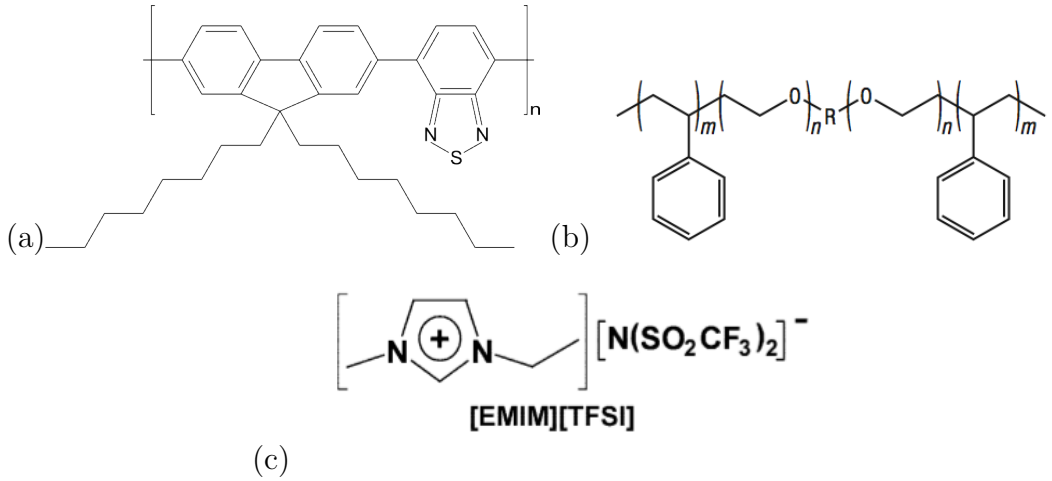

Figure 4.1: Molecular structure of (a) The semiconductor polymer, Poly(9,9'-dioctylfluorene-co-benzothiadiazole) (F8BT), (b) Triblock copolymer, poly(styrene-block- ethylene oxide-block-styrene) (SOS), (c) Ionic liquid, 1-ethyl-3-methylimidazolium bis(trifluoromethylsulfonyl)imide (EMIM-TFSI)

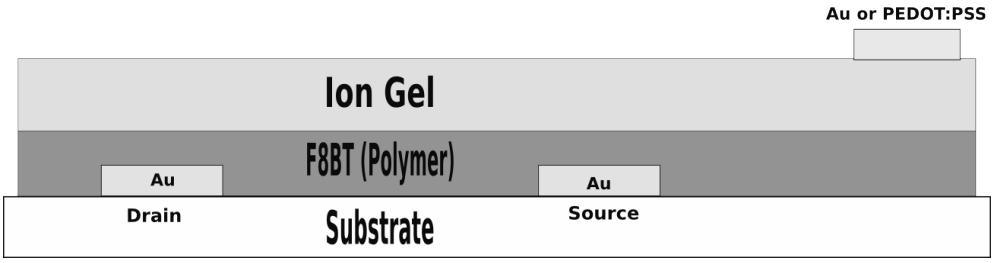

Figure 4.2: Cross sectional device structure of top gated, bottom-contact transistors. The gate electrode is off set from the channel by approximately one millimeter.

Chemical structures of materials used in this study are shown in figure 4.1. Figure 4.2 shows the schematic of transistor device structure. A bottom contact top gated transistor structure with the gate electrode offset by about 1mm away from the edge of the interdigitated source-drain pattern was used. The schematic of the transistor and microscope image of the transistor along with polycrystalline F8BT AFM images are shown in figure 4.2 and figure 4.3 respectively.

(a) 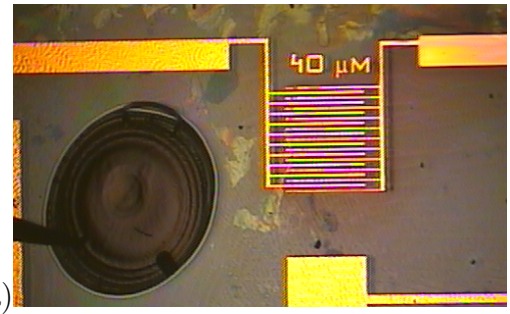

(b) 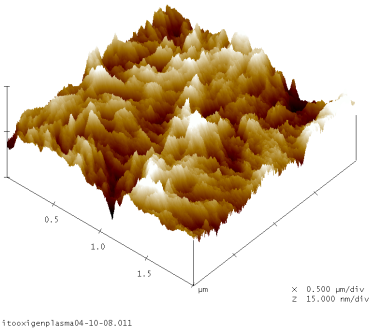

Figure 4.3: (a) Microscope image of a transistor. The gate electrode (PEDOT:PSS) is offset from the channel about a mm away. (b) AFM image showing the polycrystalline surface of F8BT film which was annealed at 290^0C.

4.2.1 Variation of Capacitance

The dependence of capacitance of the devices with frequencies and voltages was studied. Studying this variation can provide useful insights that help to determine whether the device is operating in an electrostatic mode or electrochemical mode. Measurements were done on the device structure shown in figure 4.2 with source and drain grounded and voltage applied to the gate electrode.

The variation of capacitance with frequency at various DC voltages on gate electrode is shown in figure 4.4(a). Capacitance increases by nearly one order of magnitude at -2 V on gate electrode compared with -1 V or no DC bias, indicating the increase in charge carrier concentration from $10^{12}/cm^2$ to $10^{13}/cm^2$. It is interesting to note that in the low frequency regime, below 100 Hz, capacitance value for -3 V and -2.5 V is less than that for -2 V.

Figure 4.4(b) shows the capacitance variation with voltage at 50 Hz, with oscillation amplitude of 100 mV. Systematic increase in capacitance with increasing voltages, starting around -1 V can be seen. Interestingly, the absolute value of the highest capacitance in capacitance-voltage scan compared to the capacitance-frequency scans, is lower by an order of magnitude for the same device. Capacitance-voltage measurements were carried out subsequent to capacitance-frequency measurements. Decrease in the value of the capacitance with successive measurements does not indicate a stable electrical double layer capacitance but a pseudo capacitance[18]. A pseudo capacitance is the capacitance measured

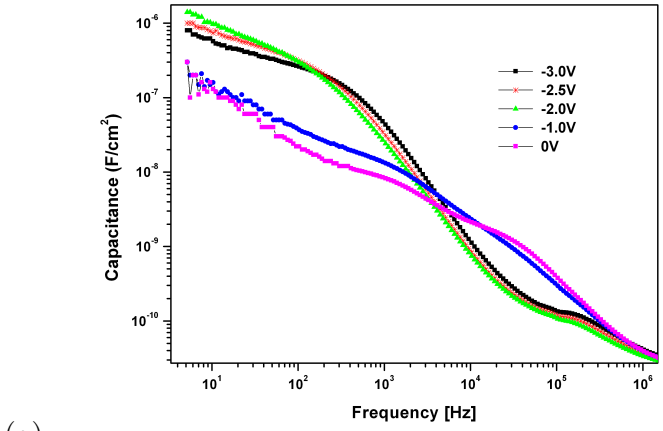

(a)

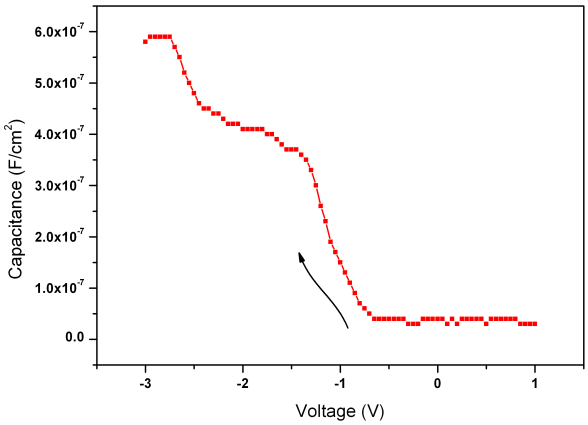

(b)

Figure 4.4: (a) Frequency dependence of the capacitance at various DC voltages on gate electrode, with source-drain electrodes grounded. (Oscillation amplitude 100mV) (b) Capacitance variation with Voltage at 50 Hz.(100 mV Oscillation amplitude)

when ions have penetrated into the active polymer layer as opposed to the capacitance measured (electrical double layer) when ions are stopped at the polymer-dielectric interface. A stable electrostatic capacitance due to electrical double layer[71] does not decrease between successive measurements and this alludes to the presence of electrochemical capacitance.

The capacitance at the interface, irrespective of whether it is completely electrical double layer capacitance[97] or the pseudo capacitance[18], it is due to the movement of ions from the bulk of the gate dielectric to the interfaces with the

semiconductors and the gate electrode, respectively, until the bulk of the gate dielectric is field-free[97] [73] [15]. Since the capacitance is due to the movement of ions, this allows the gate electrode to be spaced away[71] from the channel unlike conventional gate dielectric relying on a thickness dependent dipole polarization derived capacitance.

Having the gate electrode offset introduces certain advantages, primarily when the device is light emitting, as there is no absorption of the light by the gate electrode. The gate-offset configuration is ideal for CMS studies (section 4.2.8.1) as well, as incident light beam does not have to pass through the gate electrode thus reducing potential interference artifacts.

4.2.2 Transistor characteristics

To further understand the electrical characteristics of these ion gel devices, we study their transistor characteristics. Figure 4.5(a) and 4.5(b) show the transfer and output characteristics of the transistor with sweep rates of 5 mV/s and 20 mV/s respectively.

Transfer characteristics show an increase of drain current around -1.2 V and its saturation around -3 V of V_g, while V_{ds} was kept constant at -1 V. On-off ratio is of the order of 10^5. Considerable hysteresis can be seen in the transfer characteristics as the gate voltage is swept. The onset voltage is around -1.2 V during the forward scan and it approaches -0.3 V during the backward scan. However, clear linear ($V_{ds} \leq V_g - V_{th}$) and saturation ($V_{ds} \geq V_g - V_{th}$) regimes with less hysteresis can be seen in the output characteristics (V_{ds} sweep with fixed V_g).

Transfer characteristics were taken with slow (5 mV/s) sweep rates with continuous V_g and V_{ds} voltages without any pulsing. During the measurement of output characteristics, V_{ds} is pulsed with pulse period and width of 0.5 s and 20 ms respectively (20 mV/s sweep rate) with constant V_g.

We note that the pulsed gate voltage during the transfer scan did not help in reducing the hysteresis in transfer characteristics, unlike the pulsed voltages on V_{ds} with fixed V_g which did result in lower hysteresis in output characteristics. Inability of gate voltage pulsing to reduce the hysteresis might be due to

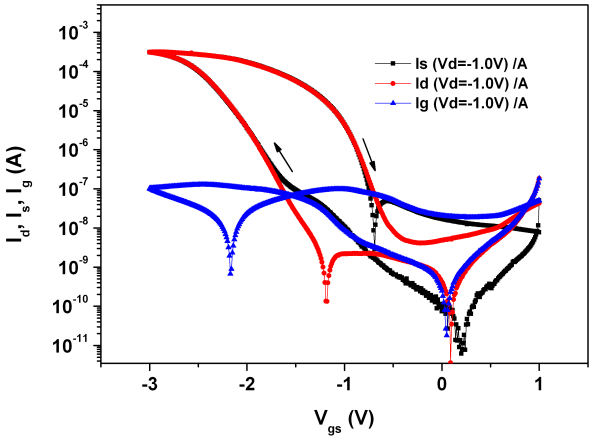

(a)

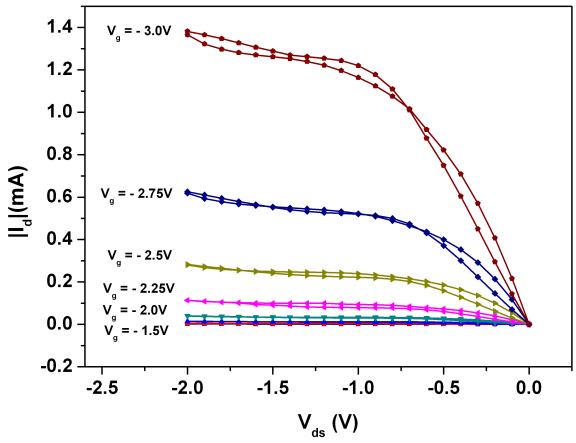

(b)

Figure 4.5: (a) Transfer characteristics of a transistor with gate electrode offset about a millimeter, with channel length, L= 40 μm and width, W= 2 cm at V_{ds}= -1 V. Sweep rate 5 mV/s (b) Output characteristics, with pulsed voltage on V_{ds} and constant voltage on V_g, Sweep rate 20 mV/s. V_g starts at -1.5 V and goes up to -3V in steps of 0.25 V

the response time of ions movement. This further supports the electrochemical hypothesis because a pure electrical double layer capacitance driven device would exhibit a faster response time.

Interestingly, whenever contact resistance feature appears in the first sweep of the output characteristics, it disappears in successive sweeps as discussed in section 4.2.5 (see figure 4.10).

Systematic increase in drain currents with subsequent sweeps with same set of drain source and gate voltages and disappearing feature of saturation to ohmic variation is an evidence towards increasing conductivity of the polymer film with time. The fast measurements with pulsed voltages helps reducing the hysteresis in the output characteristics certainly, but the increase in the levels of the drain current with consecutive sweeps are evident, which is later discussed in section 4.2.5.

4.2.3 Electroluminescence

We report the light emission in ion gel gated polymer transistors when drain source voltage V_{ds} exceeds a certain value.

Figure 4.6 shows the V_{ds} sweep to higher voltage, up to -3.6 V with two fixed V_g values. The variation of the drain current in low V_{ds} regime shows saturation behavior which is more of a typical transistor character but deviates from a typical transistor characteristics at higher voltage regime.

In the high V_{ds} regime, drain current suddenly starts to shoot up deviating from a typical transistor behavior and this is accompanied with an instantaneous light emission. In the light emitting regime, the variation of I_d with V_{ds} follows an approximate power law with power 4. The equation $I_d = b + k(V_{ds} - V_{onset})^c$ has been fit for the drain current variation, where k and b are arbitrary constants, $c = 4$ is the power that best fits the data and V_{onset} is the onset voltage that corresponds to the sudden increase in drain current.

Based on the power law fitting for the variation for I_d, in the light emitting regime, during the forward scan, in figure 4.6(a) the onset voltages for the sudden increase of drain current, V_{onset} at V_g = -3 V is -2.62 V and the same at V_g = -2.9 V is -2.42 V. While the current density in the transistor channel starts to increase when V_{ds} is approximately around the energy gap of the polymer we see the light emission in this regime. The electroluminescence increases with increasing V_{ds}.

Figure 4.6(b) shows the successive measurement where, V_{ds} is swept up to -3.2 V. The beginning of the rapid increase of the drain current in high V_{ds} regime can be seen which corresponds to the light emission in this regime.

Figure 4.7 shows the current voltage characteristics for further sweeps on the

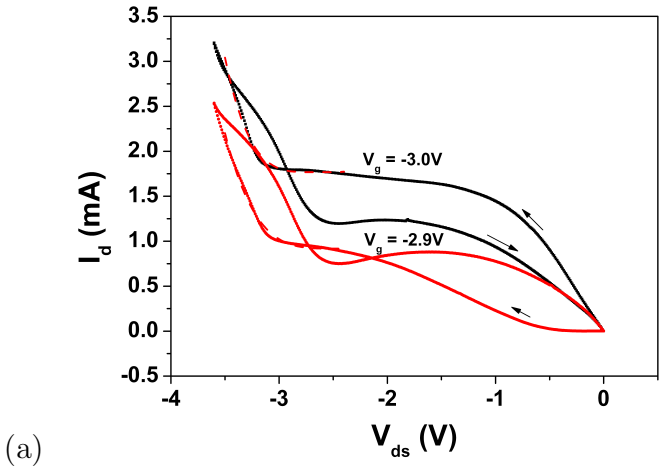

(a)

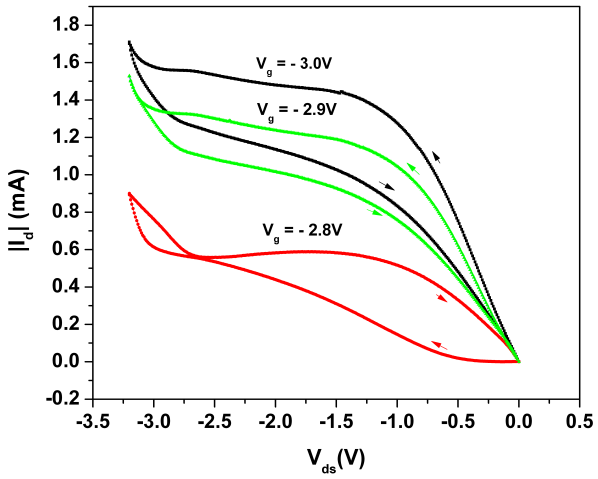

(b)

Figure 4.6: (a)I_d variation with V_{ds} while V_{ds} is swept up to -3.6 V. (b) Successive sweep with the same device, where I_d variation with V_{ds} shown for three different gate voltages, V_{ds} is swept up to -3.2 V. Light emission is observed corresponding to the shooting up of the drain currents in both cases. The contact resistance feature with the first applied gate voltage in both sweeps can be seen.

same device with corresponding electroluminescence results. While recording the current-voltage characteristics, a photodiode is placed directly on the top of the light emitting channel, and the synchronized photocurrent along with the drain current during the V_{ds} sweep have been recorded.

We can observe that the transistor characteristics start to disappear with a

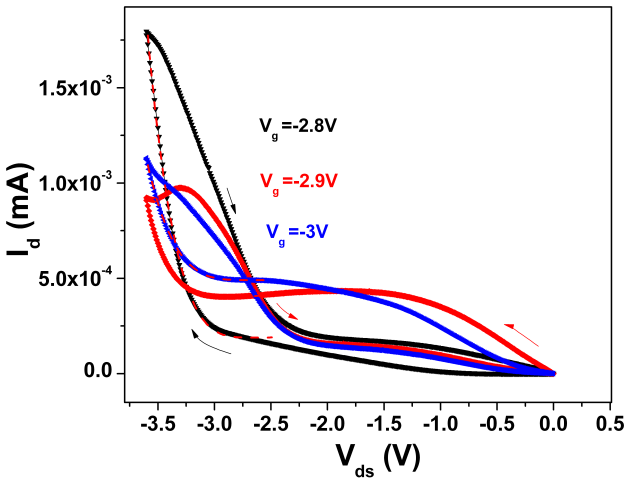

(a)

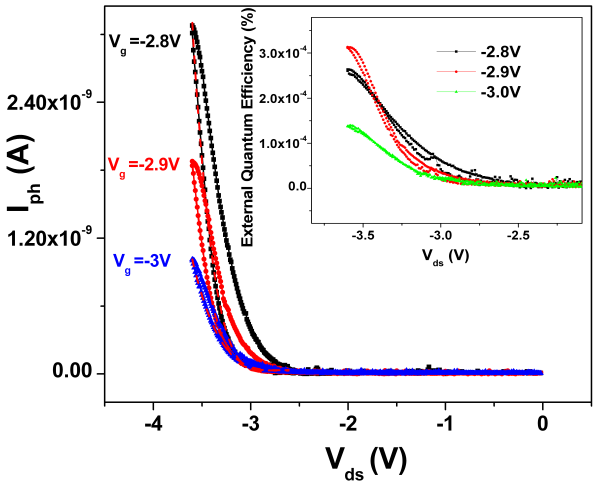

(b)

Figure 4.7: (a)V_{ds} sweep up to -3.6 V at three different gate voltages, -2.8 V, -2.9 V and -3.0 V. (b) Photocurrent (electroluminescence) variation with V_{ds} shown for the same. The red dotted line represents the power law fit for both drain current and electroluminescence in the light emission regime during the forward scan. Inset shows the external quantum efficiency (EQE) as a function of V_{ds}. (V_{ds} sweep rate 60 mV/s)

lack of clear saturation current gradually. However, in the light emission regime, the sudden increase of the drain current and the light emission are well correlated. Figure 4.7 also shows the corresponding photocurrent (electroluminescence) variation with V_{ds} and inset shows the EQE variation with V_{ds} for three different gate

voltages. The red dotted line in the light emitting region, during the forward scan, represents the power law fit for both drain current and electroluminescence. Correlation of the light emission with the drain current increase is unambiguous. Table 4.1 lists the onset voltages for both drain current and electroluminescence for three different gate voltages based on the curve fitting in the light emission regime during the forward scan. From the table, it is unambiguous that the onset voltages for both drain current and electroluminescence are very well correlated.

Gate Modulation Dependency			
V_g (V)	V_{onset} for I_d (V)	V_{onset} for I_{ph} (V)	EQE at V_{ds}= -3.6V(%)
-2.8	-2.62	-2.77	$2.64\text{x}10^{-4}$
-2.9	-2.82	-2.76	$3.12\text{x}10^{-4}$
-3	-2.65	-2.55	$1.37\text{x}10^{-4}$

Table 4.1: Dependence of V_{onset} for the sudden increase of drain current, V_{onset} for light emission and EQE at V_{ds} = -3.6V, for different gate voltages are tabulated.

Figure 4.7(b) inset shows the external quantum efficiency (EQE) as a function of V_{ds}. External quantum efficiency, $\eta_{ext} = 1.538 \times \frac{I_{ph}}{I_d}$ where I_{ph} is the photocurrent due to EL, I_d is the drain current and the numerical factor 1.538 is derived from taking into account of the photo sensitivity of the diode[14].

Increasing EQE with increasing V_{ds} can be seen from the graph. However, V_{ds} values are not swept further in order to remain within the electrochemical window of the ion gel used. Electrochemical window for the pure ionic liquid, 1-ethyl-3-methylimidazolium bis (trifluoromethylsulfonyl) imide is -3V to 2.5V[11]. However, for the ion gel, which is the mixture of the tri-block polymer with ionic liquid, the pattern of voltage limits we applied follows the reference[15] which is an extensive report on in gel gated transistors.

We can see from table 4.1 and inset of figure 4.7(b) that the external quantum efficiency at V_{ds} = -3.6 V increases from V_g = -2.8 V to V_g = -2.9 V. Increasing of the EQE with gate voltages might indicate that the polymer film is still in the initial doping levels. The possible explanation has something to do with the spatial doping levels of the polymer film (for more details see chapters 5 and 6). While only a small number of ions penetrate into the film, they would arrange themselves next to the respective electrodes and help injecting the charge carriers.

This makes the contacts ideal but leaves the rest of the channel undoped which would probably allow us to see both phases, transistor and the light emission simultaneously. However, the gradual doping of the whole film eventually plays the significant role in determining the external quantum efficiency values as discussed in section 4.2.6. Increasing of EQE with high gate voltages does not last for longer duration of time due to the the gate voltage dependent ion diffusion into the polymer as explained later in section 4.2.8.1.

We can see that the contact resistance feature present with the first applied gate voltage (V_g = -2.9 V) disappears later for further gate voltages (see figure 4.6(a) and (b)). This disappearance of the contact resistance feature for the successive scans (see also section 4.2.5) indicates the presence of ions helping the charge injection.

The drain current increases during the backward scan for V_g = -2.9 V (see figure 4.6(a)), which also is an indication of the ion penetration into the semiconductor polymer layer resulting the enhancement of current. However, the direction of the hysteresis reverses for the next gate voltage, for example with V_g = -3 V. In the latter case drain current decreases during the backward scan. We are unsure if this alludes to device degradation, as we have observed the same trend with different successive sweeps. The same trend of disappearing contact resistance feature for higher gate voltages and the reversal of the hysteresis can be seen from figure 4.7.

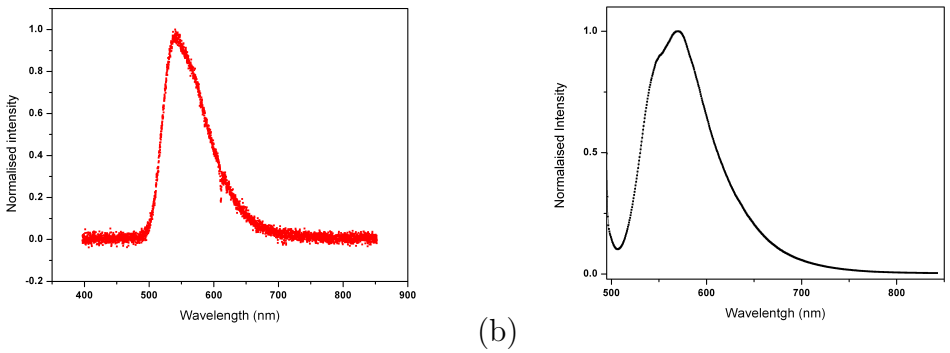

(a) (b)

Figure 4.8: (a) Electroluminescence spectra from the device (b) Photo luminescence of F8BT film.

Figure 4.8, shows the electroluminescence spectra recorded using the Ocean

Optics HR4000 spectrometer which was held directly on the top of light emitting device. The electroluminescence spectrum is similar to the F8BT EL-spectrum [138] from light emitting field effect transistor with conventional gate dielectrics (free of ions). This may be an indication of light coming from F8BT with unchanged HOMO and LUMO (due to the presence of ions). The photoluminescence spectrum of the F8BT film is shown in figure 4.8(b).

4.2.4 Recombination Zone Profile

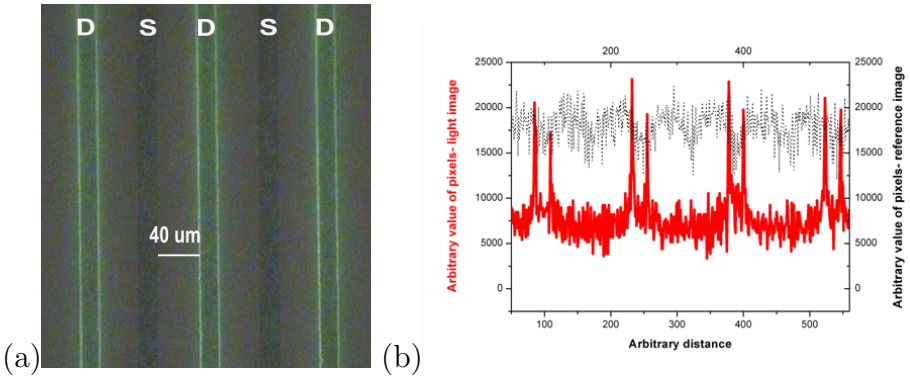

Figure 4.9: (a) Microscope image of the light emitting device, superimposed on the reference image of device (b) Cross sectional profile of reference image (black) and light emission(red). The recombination zone is in close proximity of the electron injecting electrode and overlaps with the edge of the electrode.

Figure 4.9 is a microscope image of the light emitting device superimposed on the reference image of the device taken before any voltage application. The channel length is 40 μm. It can be observed from the figure that the light emission occurs in close proximity to the electron injecting electrode. Apart from the fact that the light intensity becomes higher and the width of the recombination zone gets slightly broader with higher drain source voltage, the recombination zone does not move. This observation is consistent with the fact that we have not seen any clear evidence for n-type FET characteristics when operating the FET with positive gate and drain voltages. The recombination zone full-width-at-half-maximum is about 4 μm at V_{ds} = -3.6 V.

Observing 4μm wide recombination zone starting from the electron injecting electrode, indicates the existence of trapped electrons in that region with

which holes recombines radiatively, as these devices are electron transport limited. Nonetheless, this indicates electrons traveling up to 4 μm far from the electron injecting electrode.

Holes injected into the HOMO of F8BT from the source electrode travel through the channel till the electron injecting drain electrode, where few of the incoming holes and the injected electrons form excitons in the vicinity of the electron injecting electrode. In this respect the operation of ion gel gated polymer FET is similar to electron transport limited unipolar LEFETs[56]. Nonetheless, light emission in ion gel gated polymer FETs is different from a unipolar LEFETs due to the sharp increase in the drain current corresponding to the light emission in high V_{ds} regime, indicating a different mechanism behind light emission in these transistors.

4.2.5 Enhanced Charge Injection

While the perfect electrical double layer capacitance at the dielectric- semiconductor interface can make this system ideal for the study of charge transport at high charge carrier densities, penetration of ions into the polymer layer would render this system non-ideal. Pulsed output characteristic measurements (fast measurements) of the same device at fixed voltages repeatedly can provide a clue about the presence or absence of penetrated ions into the semiconductor layer.

Figures 4.10 and 4.11 show the output characteristics of a typical ion gel transistor, where V_{ds} is swept from 0 V to -1.5 V, in steps of 0.1 V with pulse period and width of 0.5 s and 20 ms respectively with a sweep rate of 20 mV/s. Gate voltages (continuous) are varied from -3.0 V to -3.4 V in steps of 0.1 V. Three different curves show the same but consecutive sweeps taken. Significant increase in the range of drain current can be observed. At V_{ds} =1.5V and V_g = -3.4 V, with the first sweep, the drain current reaches nearly 4 mA. With the second immediate sweep with same voltages, drain current goes up to 8 mA and with the third sweep it more than 10 mA at the same values of V_{ds} =1.5 V and V_g = -3.4 V.

Also, we can clearly see the change in the shape of the output characteristics. The variation of the drain current with V_{ds} becomes almost ohmic by the third

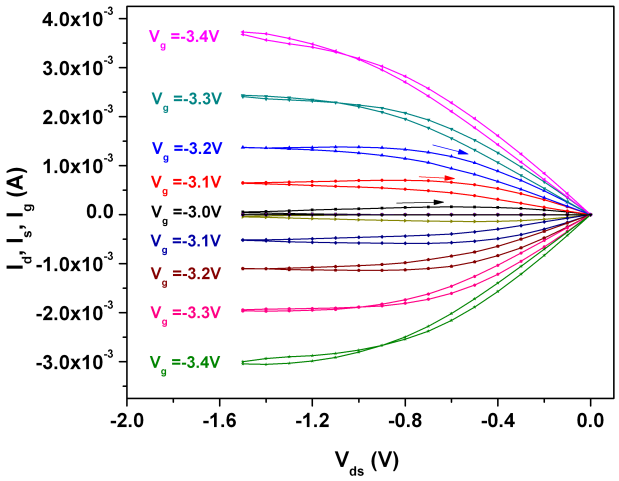

(a)

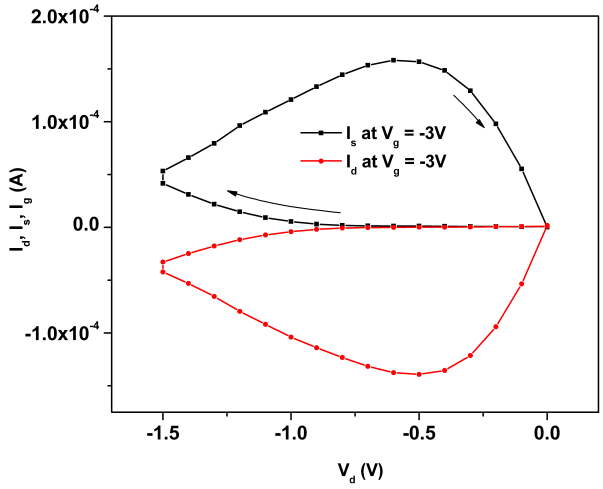

(b)

Figure 4.10: Output characteristics, with gel gated F8BT transistors with pulsed measurements on V_{ds} in order to show how the saturation behavior of the transistor disappears during successive measurements (a) Sweep:1 (b) Sweep:1 - To a different scale, showing the prominent contact resistance feature that is present at V_g=-3.0 V. Arrow marks show the sweep directions. This feature is present in all successive sweeps as well for the first applied gate voltage. See figure 4.11 for the successive sweeps.

sweep (4.11(b)), which otherwise was well saturated in the first sweep (4.10(a)). Increase in the drain current and the gradual transformation into ohmic variation of the current with consequent sweeps indicates the increasing conductivity levels

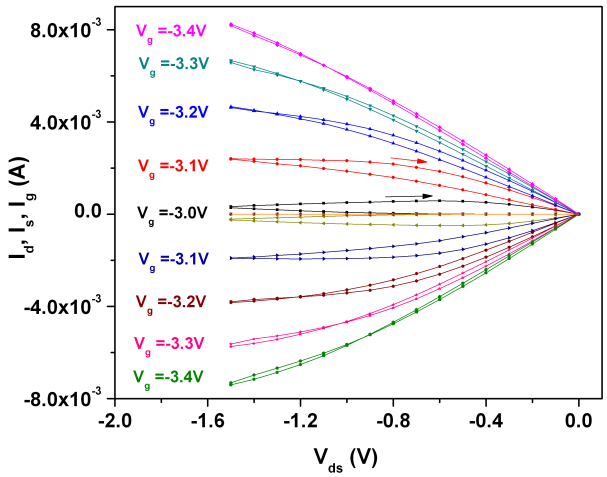

(a)

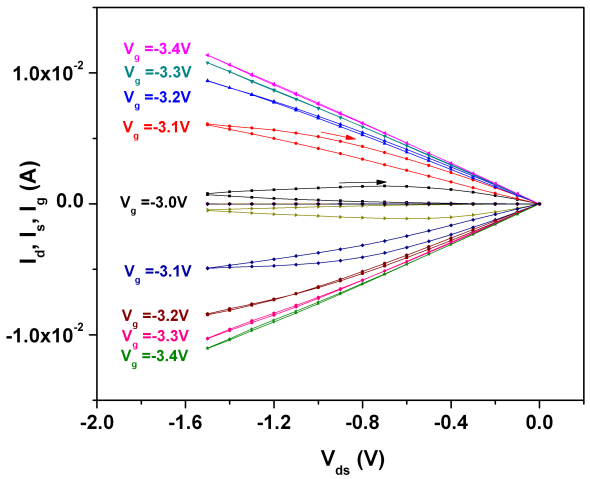

(b)

Figure 4.11: Output characteristics of the device with same voltage conditions in successive sweeps (refer 4.10 (a) Sweep:2 (b) Sweep:3 - Disappearance of the saturation regime from the previous sweeps and ohmic variation of I_d with V_{ds} is evident.

of the polymer slab.

In addition to this, we also observe the contact resistance feature which appears for the first applied gate voltage in each set of sweeps (see figure 4.10(b)) disappears for higher gate voltages. Figure 4.10(b) shows one of such a prominent contact resistance feature present initially that later disappears.

Figures 4.12(a) and 4.12(b) sum up the how the increase in the drain current

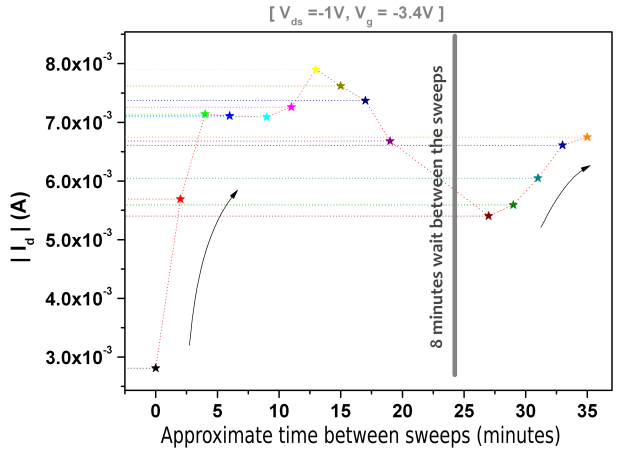

(a)

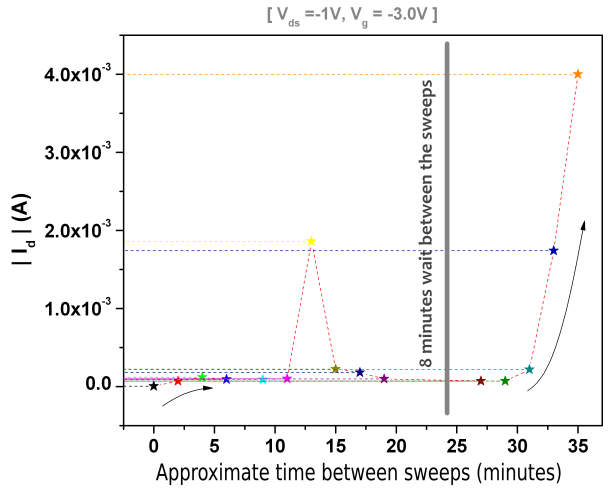

(b)

Figure 4.12: Plots showing increasing drain currents at V_{ds} = -1 V with consecutive sweeps at (a) V_g = -3.4 V and at (b) V_g= -3 V. The time along the X axis shows how the drain current increases with consecutive sweeps, as shown in figure 4.10, at a fixed V_g and V_{ds}.

happens with such sweeps at V_g = -3.4 V and V_g= -3 V. Given some waiting time between sweeps (8 minutes as shown in figure), drain currents starts from lower values again. However, the increasing trend of drain current promptly returns with the resumption of further sweeps.

The increase in drain current at V_g = -3.4 V is more pronounced than the same at V_g = -3 V during the initial sweeps. However, a prominent increase in

the drain current at V_g = -3 V during the later sweeps can be seen. A higher increase in the drain current even at a lower gate voltage is due to the effect of previously applied higher gate voltages in the preceding sweeps. This alludes to gate voltage dependent ion diffusion into the polymer active layer which could be the cause behind the increasing drain current at fixed values of voltages with consecutive sweeps.

4.2.6 Decay of the EL with V_g

In this section we study the decay of electroluminescence with gate voltage through successive measurements on a side gated device. The device structure for a side gated bilayer device is shown in figure 4.19(b).

Figure 4.13 shows electroluminescence with different gate voltages and the corresponding current variation at different gate voltages. The higher the gate voltages, the higher is the hysteresis. The direction of the hysteresis with sweep direction is shown with arrow marks. During the forward scan the drain current increases and during the backward scan it decreases rapidly leaving a large hysteresis. Compared to the hysteresis in drain current, hysteresis in electroluminescence is in same direction, yet the latter is comparatively small. Figure 4.14 shows the low hysteresis for low gate voltages. We note that the higher is the gate voltage the higher is the hysteresis.

Table 4.2 lists EQE dependency with V_g at V_{ds}= -4 V. The intensity of light emission increases with increasing V_g initially and gradually deceases at higher gate voltages. However, the external quantum efficiency of the devices does not follow the same trend. Figure 4.15 shows an exponential fall of the external quantum efficiency with gate voltage.

Decreasing onset voltages (discussed in chapter 5, section 5.3.3) and increasing electroluminescence with increasing gate voltages show the effect of gate modulation in th electrochemical regime. However, the systematic decrease in the external quantum efficiency values raises questions about the effectiveness of the gate voltage in the electrochemical light emitting regime. The decrease in the EQE with increasing gate voltages can be due to the amount of ions in the polymer being proportional to the applied gate voltages. The dependence of ion pene-

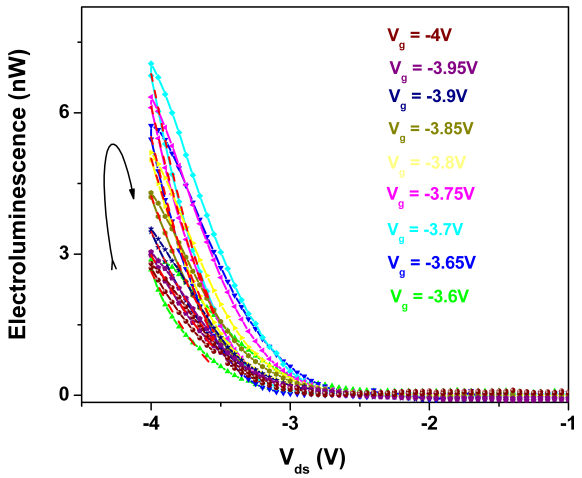

(a)

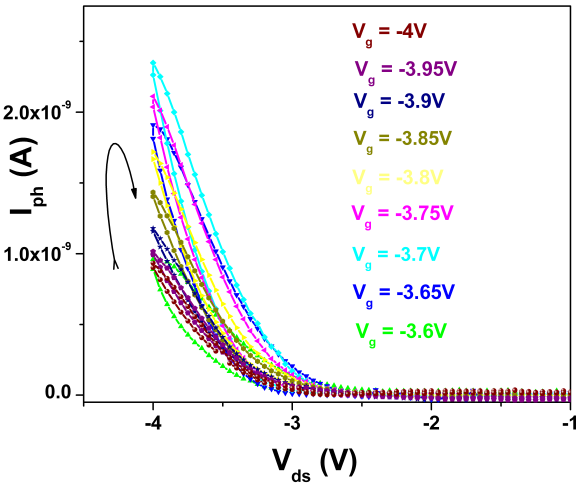

(b)

Figure 4.13: (a) The variation of photocurrent (electroluminescence) with V_{ds} with continuous set of gate voltages varying from -3.6 to -4 V in steps of -0.05 V. V_{ds} is swept up to -4.0 V. (b) The corresponding variation of I_d with V_{ds}.

tration on gate modulation is discussed later in section 4.2.8.1. The higher the gate voltage, the higher is the ion concentration in the semiconductor polymer layer. Ion associated photoluminescence quenching[57] can be a cause behind the decreasing EQE with higher gate voltages.

Figure 4.16 presents how electroluminescence starts to fall with higher gate

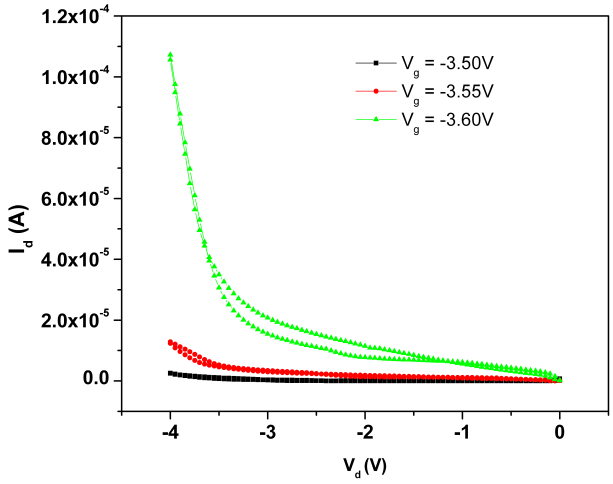

Figure 4.14: Variation of I_d with V_{ds} to a different scale for the data shown in 4.13(b), for low gate voltages showing lower hysteresis.

Gate Voltage Dependency	
V_g (V)	EQE (%)
-3.60	1.29x10^{-3}
-3.65	6.18x10^{-4}
-3.70	3.40x10^{-4}
-3.75	1.75x10^{-5}
-3.80	9.79x10^{-5}
-3.85	6.65x10^{-5}
-3.90	4.85x10^{-5}
-3.95	3.88x10^{-5}
-4.00	3.47x10^{-5}

Table 4.2: V_{onset} and EQE dependency with gate voltages at V_{ds}=-4.0 V from figure 4.13

voltages. The same figure presents the variation of corresponding I_d values at V_{ds} = -4 V. While the drain current is still increasing, a fall in the EL of the device around V_g= -3.7 V clearly indicates the effect of high gate voltages on the electroluminescence.

While the device is yet in its initial phases of doping the gate voltage can

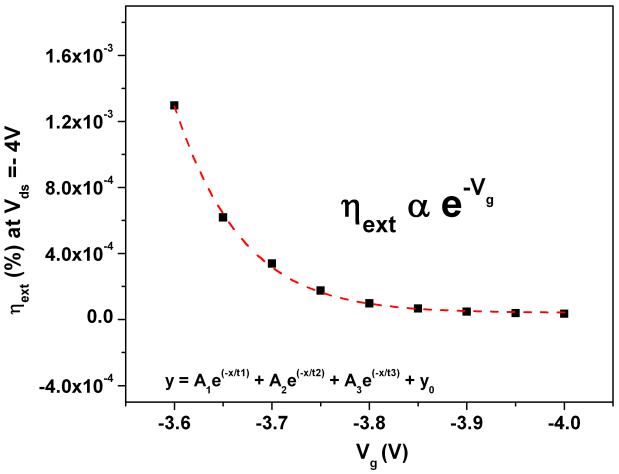

Figure 4.15: Exponential fall of the external quantum efficiency with continuous gate voltages in the light emitting regime, at V_{ds} = -4.0 V

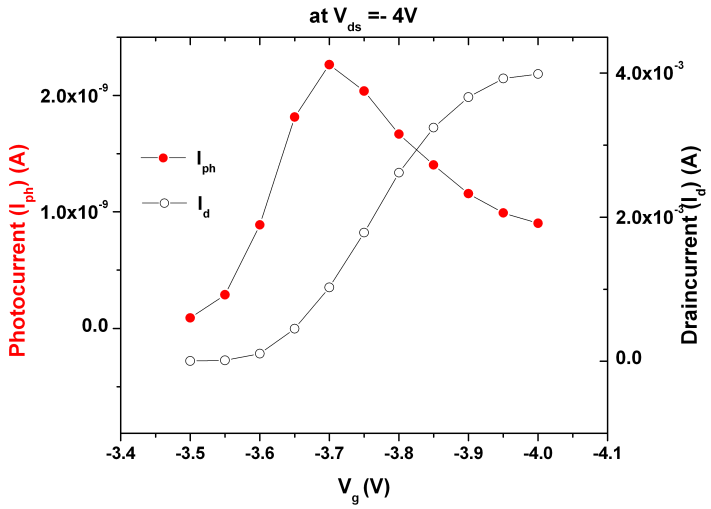

Figure 4.16: The variation of drain current and photocurrent (EL) corresponding to the data shown in figure 4.13 at V_{ds} = -4.0 V

contribute positively towards the external quantum efficiency of the device as discussed in section 4.2.3. But after prolonged operation and doping [108], beyond which no more ions are necessary for the charge injection, the influx of ions continues and just contributes towards photoluminescence quenching [57]. Beyond this point gate voltage modulation does not seem to be useful in increasing the EQE.

4.2.7 Vacuum measurements

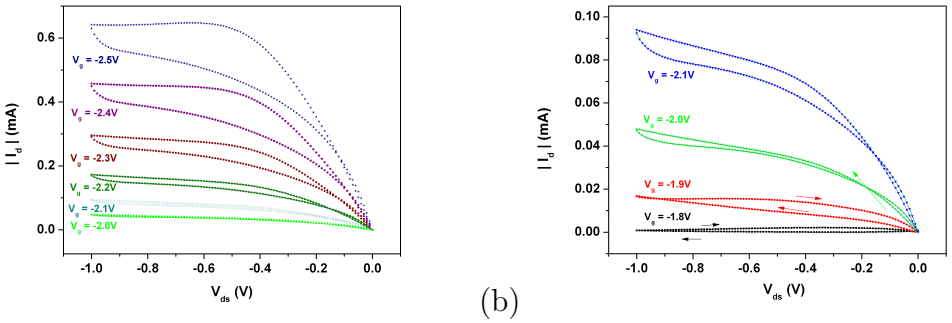

(a) (b)

Figure 4.17: (a) Output characteristics of a typical device under vacuum (b) Disappearing feature of the contact resistance present at lower gate voltage can be seen.

As seen from the location of the light emission next to the electron injecting electrode (figure 4.9) and the lack of observation of electron transport under the positive applied gate and drain source voltages we can say these transistors operate only a p-channel mode and are electron transport limited.

In order to investigate the possibility of presence of moisture resulting in a lack of electron transport in ion gel gated polymer transistors, we carried out measurements in vacuum. The device was heated at 360 K overnight under vacuum (10^{-7} mBar) to eliminate moisture. While the measurements were carried out, the device was cooled down to room temperature under the same vacuum. Figure 4.17 shows the output characteristics under vacuum of (10^{-7}mBar).

The disappearing feature of the contact resistance that present with the first applied gate voltage remains the same under the vacuum as shown in figure 4.17(b).

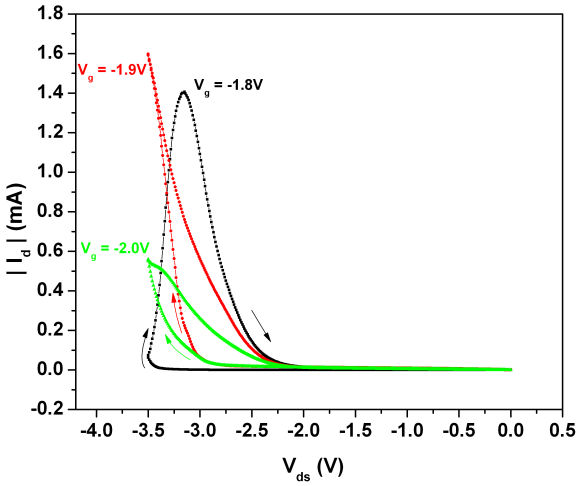

(a)

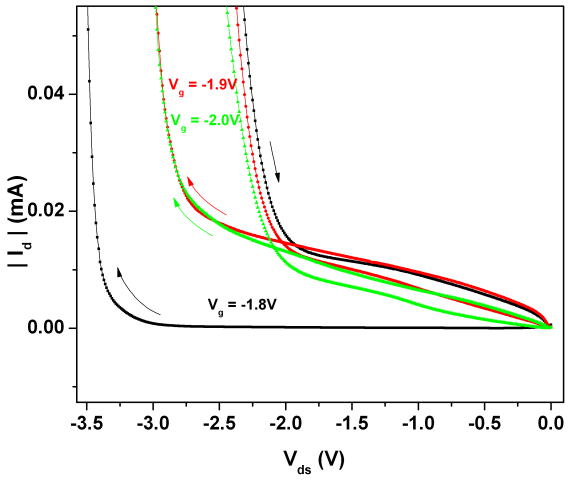

(b)

Figure 4.18: (a) Light Emitting Regime under vacuum (b) The contact resistance feature with V_g = -1.8 V and ohmic increase if I_d for higher gate voltages in low V_{ds} regime.

The light emission is in the similar fashion under vacuum and occurs near the drain electrode and we have not observed any electron transportation for operation with positive voltages in vacuum either. Figure 4.18(a) shows the shooting up of the drain current at different gate voltages. Figure 4.18b shows the same with a different scale. We can clearly see the drain current increasing

only when V_{ds} is around approximately the energy gap of the transistor, with $V_g = -1.8V$, whereas for the subsequent gate voltages we see the ohmic increase of the drain current with V_{ds} in the regime where, $V_{ds} < E_g/e$.

4.2.8 Gate Dependent Ion Diffusion

4.2.8.1 Charge Modulation Spectroscopy Studies

In order to understand the gate voltage dependent ion penetration into the semiconductor film on the application of the voltages, we carried out Charge Modulation Spectroscopy (CMS) measurements.

This technique allows detection of the changes in the transmission coefficient of the semiconducting film due to charge accumulation, in this experiment due to the application of the gate bias. These measurements differ from CMS measurements reported previously[51], where a lock-in modulation technique was used to detect only mobile charges which can respond to the frequency of the gate voltage modulation, which is typically in the range 10-100Hz[51] [54]. The present technique is also sensitive to trapped charges as well as to charges induced by electrochemical doping, because no lock-in amplification is employed to detect the changes to the transmission coefficient. The transmission spectra are recorded using a high sensitivity spectrophotometer, which is able to track the changes in the spectrum upon application of a dc bias to the gate electrode.

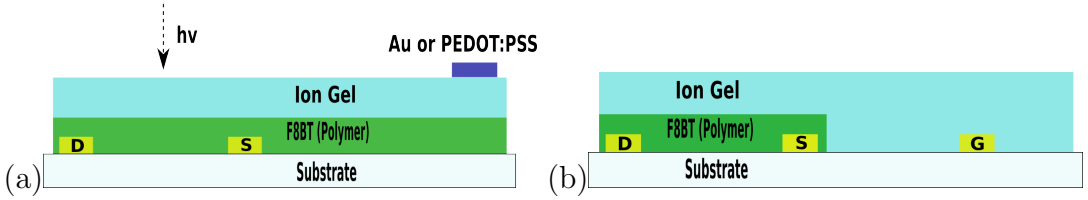

Figure 4.19: Schematic of the devices used for the CMS studies (a) Top offset gate electrode with bottom contacts pattern, (b) Side gated devices with gate on the same plane as source and drain electrodes with patterned polymer.

4.2.8.2 Hole Accumulation Regime

These in-situ measurements were done in a nitrogen atmosphere with either offset gate or side gate (figure 4.19(a) and (b)). Topologically having the offset gate

electrode on the top of the gel (figure 4.19(a)) is equivalent to having the gate electrode in the same plane as the source and drain electrodes provided that the polymer is suitably patterned (Figure 4.19(b)). There are minor quantitative differences in the magnitude of the CMS spectra and of the voltages needed to observe the same intensity values on the CMS spectra, but there is no qualitative difference in the behavior of the devices. The results presented in the following section however are with an offset top gated device with the voltage application on the gate electrode while the source and drain electrodes are grounded.

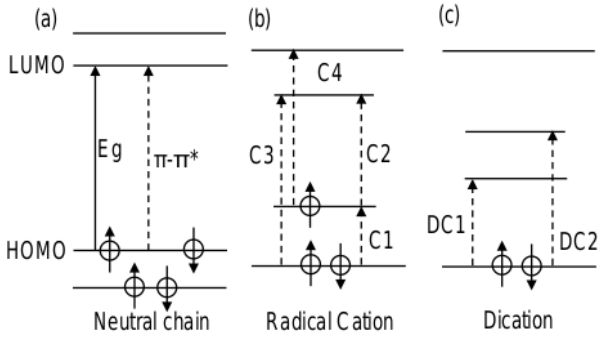

Figure 4.20: Schematic of one-electron energy level diagram and optical transition of (a)neutral, (b) singly charged (polaron) (c) doubly charged (bipolaron) organic polymer semiconductor. Only C1, C2 and DC1 optical transitions are allowed in the polaron and bipolaron energy diagram,as the rest are symmetry forbidden [19].

The energy diagram of the neutral molecule is shown in figure 4.20. The diagram shows the changes to the electronic energy levels when a charge is induced in the molecule. The HOMO - LUMO transition energy levels are shifted while new sub-bandgap transitions appear inside the HOMO - LUMO gap. The intensity of the neutral transition of an F8BT film would be decreased by inducing charges in the transistor and new transitions can appear at lower energies.

The variation of the optical transmission spectrum when negative gate voltage is applied is shown in figure 4.21. All the spectra are referenced and normalized to the transmission spectrum of the grounded device ($V_g = 0$ V), by plotting $\frac{T_{Vg} - T_{0V}}{T_{0V}}$ for different gate voltages. The output curve of the transistor, taken after each optical measurement, is shown in figure 4.23. The two measurements have been taken successively: after setting the gate voltage, the optical spectrum was taken,

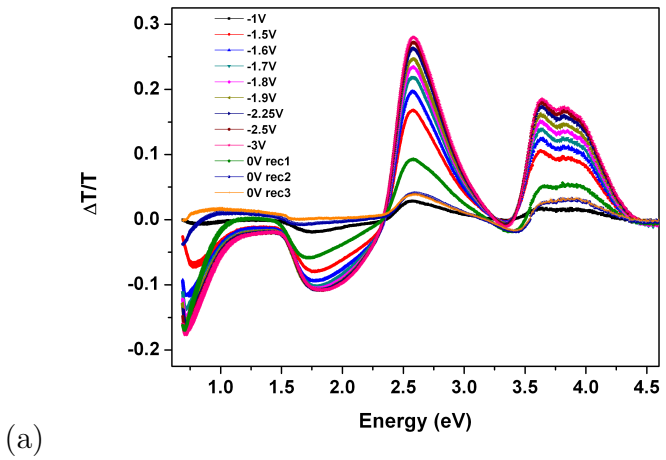

(a)

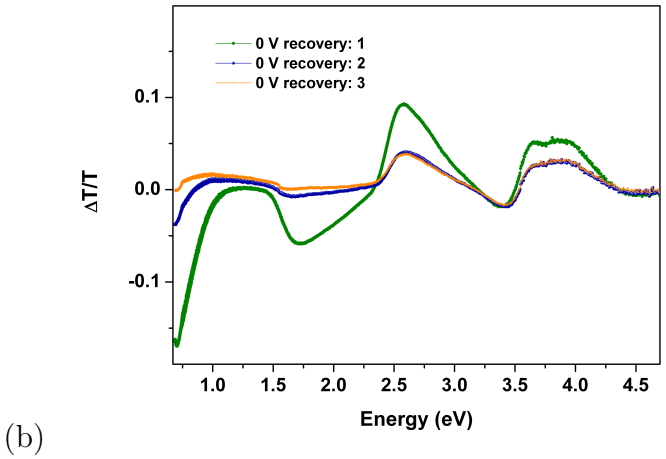

(b)

Figure 4.21: (a) CMS Spectra in the hole accumulation regime: Variation of $\Delta T/T$ with Energy at different gate voltages starting from -1V to -3V are shown. (b) After the removal of gate voltage, three 0V recovery spectra are shown separately.

and the V_{ds} sweep for that particular voltage was acquired. This way the output curve can be directly correlated to the optical measurements.

The CMS spectrum shows three broad induced absorption (negative $\Delta T/T$) features, at 0.7 eV, 1.8 eV and 3.4 eV, and two bleaching features (positive $\Delta T/T$) at 2.6 eV and 3.8 eV. The induced absorption at 0.7 eV and 1.8 eV and the bleaching at 2.6 eV and 3.8 eV are associated with the characteristic charge-induced absorptions from charge species in F8BT and the associated bleaching of the neutral $\pi - \pi^*$ transitions[31] [6]. This is due to the shift in the allowed

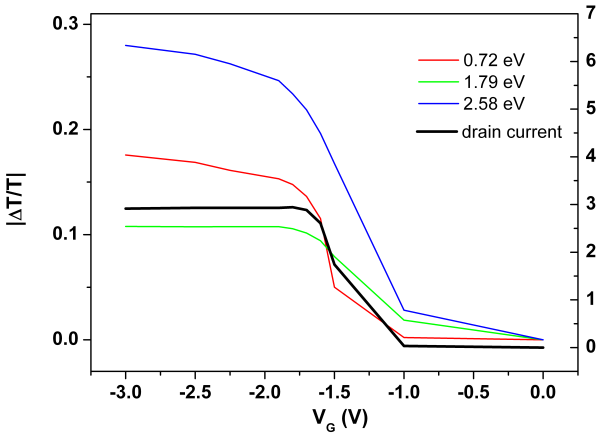

Figure 4.22: Variation of $\Delta T/T$ with gate voltages at different energies(0.7 eV, 1.8 ev and 2.6 eV). The graph also shows the variation of the drain current with V_g.

transitions in the molecule when a charge is accumulated on it, as explained earlier. These features are already present with V_g = -1 V, and increases with increasing gate voltages.

I_d versus V_{ds} curves obtained after finishing the optical scan, show no saturation of the current. The current magnitude follows the increase in the polaron induced absorption (PIA) and bleaching for gate voltages below -1.9 V. Once the gate voltage exceeds -1.9 V the current saturates and does not increase anymore, while the CMS signals keep increasing.

Moreover, the dynamics of the induced absorption at 0.7 eV and 1.8 eV follow different trends. The latter is the first to increase with the voltage, while the low energy one increases at a later stage. This could be due to the formation of bipolarons in the device when the charge concentration is sufficiently high (given the higher energy needed to create a bipolaron a high polaron concentration is needed for the bipolaron to be stable)(see figure 4.22)

The week induced absorption feature at 3.4 eV might involve the polaronic (higher energy transition) energy levels. It is possible that its identification might be hindered by the overlap of the bleaching features.

The increase in the bleaching suggests that new charge is injected when the gate voltage is increased beyond -2 V. Since the concentration of polarons is

unaffected by the increase in voltage (the 1.8 eV induced absorption saturates at -2 V) it indicates all charges injected would form bipolarons (the increase in the 0.7 eV induced absorption). The saturation in the current is an indication that bipolaron mobility is orders of magnitude lower than polaron mobility.

By applying the Beer-Lambert law, to a semiconducting film with both charged and neutral molecules, the $\Delta T/T$ signal can be expressed as:

$$\Delta T/T = \exp^{[(\sigma_N(E)\Delta n_N)+(\sigma_P(E)n_P)]t_0} - 1 \tag{4.1}$$

Where $\Delta n_N = n_N{}' - n_N$ (n'_N being the density of neutral site in the charged film, $n_N = 7.7 \times 10^{20} cm^{-3}$ being the density of neutral sites in pristine film, as determined by x-ray measurements on F8BT films); $\sigma_N(2.6eV) = 2 \times 10^{-16} cm^2$ is the optical cross section for the neutral absorption, determined measuring the optical transmission of a F8BT film of known thickness [32]; σ_P is the optical cross section for the polaron absorption and n_P is the density of polarons in the charged film. t_0 is the thickness of the polymer film, about 40 nm.

From previous work on charge transfer doping of F8BT it was possible to estimate a cross section for the polaron absorption of $\sigma_P(1.8eV) = 2 \times 10^{-16} cm^2$ [31], and a number of bleached F8BT units per polaron of 1, measured in the case of charge transfer doping of F8BT films with MoO_3 giving a high localization of the polaron over just one repeating unit [32].

If we consider the polaron cross-section to be zero where we have the bleaching maximum, it is possible to estimate the amount of F8BT site that are bleached upon application of the gate bias, from the intensity of the bleaching.

For the maximum gate voltage of -3 V, the peak value for the bleaching is $\Delta T/T = 0.28$, which gives a density $n'_N = 4.6 \times 10^{20} cm^{-3}$, 60% of the density of the pristine film ($7.7 \times 10^{20} cm^{-3}$ being the density of neutral sites in pristine film, as determined by x-ray measurements on F8BT films). The rest 40% of repeating units are bleached because charged.

The polaron induced absorption at 1.8 eV, gives a density of polarons in the film of $n'_N = 1.5 \times 10^{20} cm^{-3}$, and given the estimate for the polaron delocalization from charge transfer doping, these account for half of the bleached F8BT repeating units. This correlates well with the observation that the 0.7 eV absorption is

due to bipolarons, in which case the rest of the bleached F8BT repeating units could be in the bipolaron state. This is confirmed by the increase of the 0.7 eV feature beyond V_g = -2 V, together with the increase in bleaching, while the 1.8eV feature is saturated.

After sweeping the gate up to -3 V, the gate is grounded, and subsequent scans are taken to study the evolution of the charge accumulated in the device. As can be seen from figure 4.21(b) after the first recovery scan, most of the charge is still present in the channel of the transistor, and it decreases down to 10% in about 15 minutes . The high amount of film charged upon application of the gate bias (40%) and the long response time to the removal of a gate bias, clearly shows that doping of F8BT due to diffusion of the $TFSI^-$ ions into the semiconducting film is taking place.

Moreover, the differential absorption values obtained for ion gel gated polymer transistors are two orders of magnitude higher than that for normal transistors[132] [140]. This is not compatible with the formation of a thin charged layer at the interface with the dielectric, due to electrostatic effects only. Using a capacitance value of $1\mu F/cm^2$ for the ion gel, we can estimate a charge density of $1\times10^{13}cm^{-2}$. When the device is operated in the pure electrostatic filed effect mode, this charge density would only give a bleaching peak value of 5×10^{-3} as calculated using the Beer-Lambert law.

The current values before the scan with the application of -1 V on V_g were one order lower than the one taken after the scan (after the application of 5 minutes -1V) which is consistent with increasing I_d with time as discussed in section 4.2.5. Each scan (while obtaining the spectra over the energy range shown) takes 5 minutes. This necessitates the application of the gate voltage during this interval of time that corresponds to entire scan. Each gate voltage is hence applied on the transistor for 5 minutes. All scans were performed from lower to higher energies. Since the output characteristics shown were taken after each optical scan, there is no sign of saturation which is expected with these transistors. (See section 4.2.5).

We note that we haven't seen any changes in the absorption spectra without applying the gate voltage.

This experiments demonstrates the gate voltage dependent ion diffusion into

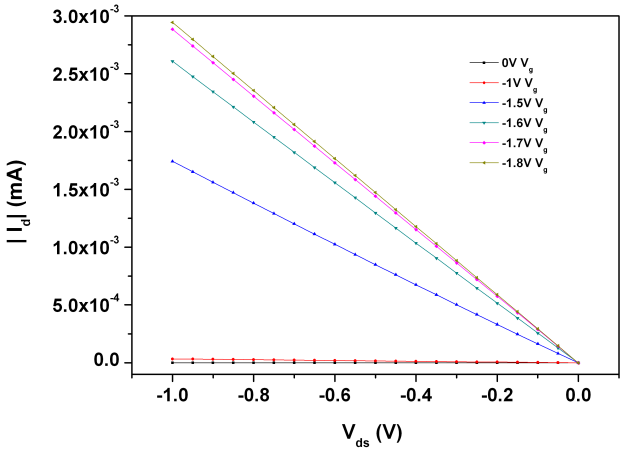

Figure 4.23: The output characteristics showing the variation of I_d with V_{ds} taken each time after the spectrum scan at different gate voltages that correspond to respective CMS spectra. For gate voltages higher than V_g = - 1.8 V, the I_d variation with V_{ds} overlaps with the same at V_g = -1.8 V.

the polymer semiconductor from the ion gel layer in the hole accumulation regime. The increasing intensity features with increasing gate voltages give us an indication of increasing number of ions in the polymer film with increasing gate voltages.

This increase of ion concentration with increasing gate voltages would explain the fall of the external quantum efficiency with higher gate voltages which can only increase the ion concentration in the film contributing towards the photoluminescence quenching of the device as discussed in section 4.2.6.

If the device is completely an electrostatic field effect driven transistor [132] [140] such a charge density would give a bleaching peak value of 5×10^{-3} as calculated using the Beer-Lambert law while in these measurements a bigger increase is already present, of the order of 0.1 $\Delta T/T$, which can be only due to electrochemical doping of the F8BT film and cannot be accounted for by the formation of an electric double layer only.

When the polymer is highly doped, showing such a high carrier density $n'_N = 4.6 \times 10^{20} cm^{-3}$ at -3V, (refer figure 4.21) it is plausible that it would quench the photoluminescence of the polymer which we later show in chapter5 with fluorescence probing of the working light emitting bilayer devices.

4.2.8.3 Electron Accumulation Regime

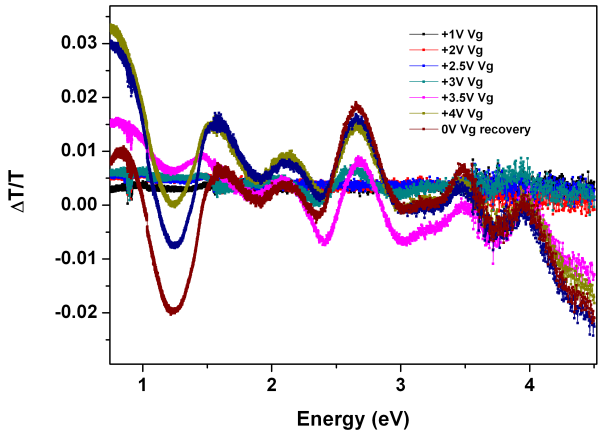

Figure 4.24: CMS Spectra in the electron accumulation regime: Variation of $\Delta T/T$ with Energy at different gate voltages starting from 1 V to 4 V are shown.

The same set of measurements have been done for positive gate voltages and showed no sign of ion induced doping. The result is shown in figure 4.24. No charge-induced absorption characteristic of the radical anion was observed for voltages up to 4 V . The ripples in the $\Delta T/T$ scan might be due to degradation of the device due to the unscreened electric fields present, or, as will be explained later, to the presence of positive ions inside the F8BT film, without the screening effect of the electrons on the F8BT molecules.

In principle it is not possible to exclude the penetration of positive $EMIM^+$ ions in the F8BT layer with positive gate voltages, not balanced by electron injection. Given also the similar threshold for hole and electron injection, and the high local field that would be produced by the unbalanced positive ions inside the F8BT film, the most plausible cause for the lack of electron accumulation is that positive ions cannot diffuse in the F8BT film, as opposed to the negative ions which can more easily penetrate in the polymer matrix. We can not rule out the extreme low diffusivity of the positive $EMIM^+$ ions compared to the $TFSI^-$ ions (refer chapter 5).

However these measurements clearly show the evidence for penetration of $TFSI^-$ ions into the semiconductor under negative gate voltages. Holes injected

to HOMO of F8BT travel through the channel, modulated by gate voltage, till the electron injecting (to LUMO of the polymer) drain electrode, where few of holes and electrons forms excitons, some of which recombine radiatively, in the vicinity of the electron injecting electrode. This is similar to electron transportation limited unipolar light emitting field effect transistors (LE-FETs) except for the doping induced enhancement of holes.

Appendix 7.2 provides further data about the electron transportation in ion gel gated devices.

4.2.9 External Quantum Efficiencies and Enhanced Mobilities

Compared to EQE values of poly-(methyl methacrylate) (PMMA) gated ambipolar transistors (0.5%), EQE values of ion gel gated F8BT transistors are considerably lower (10^{-4}%). The main difference is the balanced holes and electrons mobility with the former, whereas with the latter there is no electron transportation. With the ambipolar light emitting FETs with balanced hole ($\mu_h = 6{\times}10^{-4} cm^2V^{-1}s^{-1}$) and electron ($\mu_e = 5{\times}10^{-4} cm^2V^{-1}s^{-1}$) mobility[138] and the recombination zone in the middle of the channel (without any electrode absorption[6]), higher EQE values (0.5%) result with PMMA gated F8BT transistors.

With ion gel gated F8BT devices, the hole mobility is enhanced (see below) compared to the same in LEFETs[138]. Holes with very high mobility travel faster through the channel and recombine with electrons injected from the drain contact, in the proximity of drain electrode. We assume the electron mobility to be several orders of magnitude lower than the hole mobility as we can see no evidence for unipolar electron transport for positive voltage operation. This could be one reason why lower EQE values are observed with these unipolar, hole mobility enhanced devices. Interestingly, light output in PMMA gated F8BT light emitting FETs and the same with ion gel gated F8BT unipolar transistors are comparable (of the same order). This implies that the number of formed excitons which recombine radiatively in both cases are comparable.

In addition to the limited electron transportation the other factor that contributes to the decrease in the EQE can be the metal absorption of the light

emission due to the presence of the recombination zone in the proximity of electron injecting electrode[5]. The association of ions with the polymer layer and photoluminescence quenching due to ions (see chapter 5) could also be playing significant role in low external quantum efficiencies of the device.

The mobility values that are calculated using the standard FET equations ($\mu_h \approx 1cm^2V^{-1}s^{-1}$) however do not take into the account the presence of any ions in the active polymer film.

This linear mobility value ($V_{ds} < V_g$ regime), calculated from the equation 4.2 does not really match well with the value calculated from polaron density obtained from CMS measurements using the equation 4.3.

$$I_d = \frac{WC_i}{L} \cdot \mu \cdot (V_g - V_{Th}) \cdot V_{ds} \tag{4.2}$$

where I_d is the drain current, $W/L = 500$, with channel width, W = 2 cm and length, L = 40 μm respectively, C_i is specific capacitance, V_{ds} is the drain-source voltage, V_g is the gate voltage and V_{th} is the threshold voltage. The mobility values are of the order of $1cm^2V^{-1}s^{-1}$ are calculated for a transistor showing well behaved saturation characteristics (refer figure 4.5).

From the polaron densities calculated at a fixed gate voltage from CMS studies on a similar device, we can determine the corresponding mobility, using the equation,

$$I_d = P \cdot \mu \cdot \frac{W}{L} \cdot t \cdot V_{ds} \tag{4.3}$$

where $P = 4.6 \times 10^{20} cm^{-3}$ is the polaron density calculated from the charge modulation spectroscopy measurements at a fixed value of V_g= -3 V, where I_d is the drain current, $W/L = 500$, with channel width, W = 2 cm and length, L = 40 μm respectively, t is the thickness of the polymer film, 40 nm, and V_{ds} is the drain-source voltage. Using the equation 4.3, for drain current of 3 mA at V_g= -3 V and V_{ds} = -1 V, we obtain a mobility value of, $\mu = 2.035 \times 10^{-2} cm^2/V.s$.

This in comparison with the mobility value calculated using standard FET equation under the same voltage conditions (with well saturated transistor characteristics) ($\mu_h \approx 1cm^2V^{-1}s^{-1}$) is two orders of magnitude lower.

This implies that it is necessary to account for the presence of ions while calculating the mobility values in ion gel gated transistors and standard FET

equations can not be used without further modifications.

4.3 Ion Gel Bilayer Devices

We report that the ion gel gated transistor devices also exhibit light emission in two-electrode bilayer mode when the gate terminal is absent. We discuss measurements on device structures without a gate electrode in this section. As discussed in earlier sections, when the gate electrode is present, its location does not matter but only the potential applied to it. It then follows that we can apply the potential difference across the gel from top to bottom fashion or on the same plane. Ion gel bilayer devices use the latter configuration and totally eliminate the gate electrode.

Figure 4.25 shows the current voltage characteristics and the corresponding photocurrent due to the electroluminescence of a planar, bilayer device.

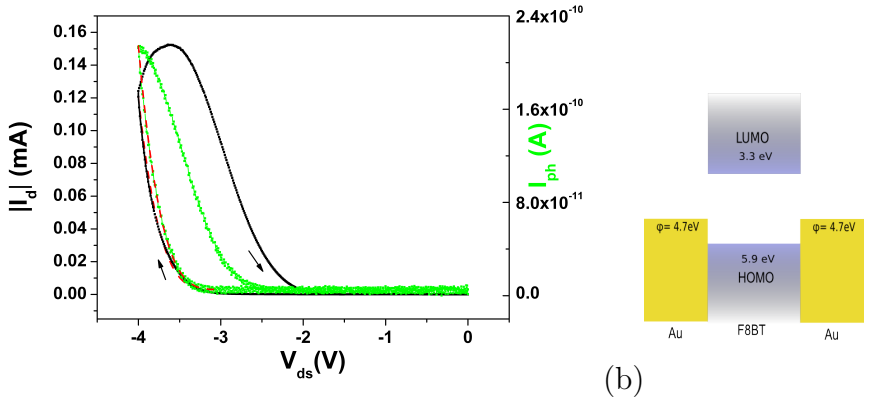

(a) (b)

Figure 4.25: (a) The variation of the drain current and the photocurrent (electroluminescence) with V_{ds}. The red dotted line shows the power law fit during the forward scan in the light emission regime. V_{onset} for the drain current= -2.99 V and V_{onset} for light emission = -2.95 V (b) Schematic showing the HOMO and LUMO of the polymer semiconductor, F8BT and work function of the metal electrodes(Au) used.

Similar to ion gel gated transistors, the variation of I_d and I_{ph} with V_{ds} follows the pattern $I_{ph} \propto I_d \propto (V_{ds} - V_{onset})^c$ where, k is an arbitrary constant, V_{onset} is onset voltage for the increase of drain current or light emission and $c = 4$, the power that best fits the data. The shooting up of current starts with $V_{onset} =$

-2.99 V and the emission of light withV_{onset} = -2.95 V.

These devices without any gate modulation emit light in the similar pattern to transistors. More interestingly, both the increase in current and the light emission gradually build up. For example, the V_{ds} sweep shown in figure 4.25 is the second sweep after the application of voltage, and its previous (first) sweep, with the same voltage conditions shows lower I_d and the electroluminescence values which are an order less than the same in subsequent sweep shown above.

The similar light emission patterns when $V_{ds} > E_g/e$, reveals that with our three terminal devices, we are seeing nothing but the combination of a transistor which is partially electrochemical (at low V_{ds} regime) and an LEC (high V_{ds} regime) with the gate voltage modulation. The modulation of the gate voltage is meaningful when the polymer film is not doped or slightly doped only at the metal electrodes(charge injection region) due to ions penetration and it's possible to have the combination of transistor and LEC simultaneously in the initial stages. As doping increases, the transistor saturation features start to disappear.

Due to the properties of ion gels, whether the voltage is applied along the same plane or different plane has same effects on the movement of ions. The evidence of light emission while V_{ds} is approximately of the order of E_g/e of the polymer within the few seconds of voltage application hence clearly sets the limit also for the gate voltages beyond which the transistor is electrochemical. This answers the fundamental question of operation of transistors under such voltage conditions.

The bilayer devices are investigated in detail in chapter 5 and in chapter 6 we present a numerical model for ion diffusion in polymer-ion gel bilayer, planar LECs.

4.3.1 Light emitting mechanism in Ion gel gated polymer FETs

The prominent role of the (V_{ds}) in the light emission regime, possibility of ion penetration into the polymer on voltage application makes this light emission distinctly different from that observed in ambipolar light emitting transistors with balanced holes and electrons transportation.

As discussed in section 4.2.5, while the device is operated in the transistor regime ($V_{ds} < E_g/e$), the increase in drain current at constant values of V_g and V_{ds}, with consecutive sweeps gives us an indication of ion penetration into the polymer with gate voltage, as opposed to the pure electric double layer effects alone. From the charge modulation spectroscopy study of the device (discussed in section 4.2.8.1) we see a clear evidence for gate voltage dependent ion penetration in to the polymer layer.

The sudden increase of drain current correlated with the light emission with approximately $V_{ds} > E_g/e$, and the evidence for the ion penetration in to the active polymer layer on the application of gate voltage(section 4.2.8.1, also see chapter 5 and chapter 6) and evidence of the light emission in bilayer devices, indicate that the light emitting mechanism is similar to light emitting electrochemical cells rather than the light emission in pure polymer film similar to LEDs.

4.4 Summary and Conclusions

We have demonstrated light emission in ion gel gated polymer transistors when the drain source voltage exceeds above the voltage corresponding to the energy gap of the polymer. We show that the light emission is correlated with drain current and follows the power law with the power 4. Further, through a CMS study and the light emission in the bilayer planar device, we infer that the light emission is due to gate voltage dependent ion diffusion in to the semiconductor layer. This mechanism behind the light emission in these ion gel gated polymer transistors is more similar to the light emitting electrochemical cells than pure field effect light emitting transistors. Since the light emission is associated with the presence of penetrated ions in the polymer layer these devices are similar to light emitting electrochemical cells in the the light emitting regime.

Owing to the properties of ionic liquids and ion gels, having the potential difference across the ion gel, whether it is top-bottom voltage application or the applying the potential difference to the electrodes on the same plane, along the gel is in principle is of no difference. When we see the light emission in bilayer devices with such low voltages ($V_{ds} > E_g/e$), it unambiguously indicates the presence of ions associated with the polymer. We rule out the presence of ions

inside polymer before the application of the voltage, by comparing the polymer absorption spectra with bilayer absorption spectra.

Having the gate modulation in the beginning stages of doping of the polymer, the device exhibits the characteristics of both transistor and light emitting electrochemical cell. However, eventually, having the gate modulation for the longer duration of time only contributes towards reducing the external quantum efficiencies. In addition to this, transformation of saturation regime into ohmic variation of current in the transistor region shows the increasing conductivity of the polymer layer. Because of the fall of the EQE with gate voltage being exponential in this regime, the bilayer without gate modulation proves to be most advantageous from the light emission point of view.

From the LEC point of view, the bilayer approach, as opposed to mixture of polymer and electrolyte or ionic liquid [83], eliminates the phase separation issue. Bilayer LECs due to their simplicity, in principle make it possible to conduct more controlled studies for understanding the electric field distribution [86,102] in LECs which has been the subject of the debate [33] in recent years. Suitable choice of ions with comparable diffusivity with suitable polymer with balanced hole and electron mobility in these planar room temperature light emitting bilayer devices could result high EQEs at lower voltages and would have considerable application potential.

Chapter 5

Planar, Bilayer Light emitting Electrochemical Cells(LECs)

5.1 Introduction

Electroluminescent organic polymer semiconductor OLEDs have been successfully commercialized in small displays[20] [43] [68] [38]. However, realizing their potential in large area display applications has been slow, some of the reasons being the expensive vacuum processing in case of small molecule OLEDs and reactive low work function cathode in polymer OLEDs.

However, the use of dynamically doped organic semiconductors can overcome this problem since doped devices allow high work function electrodes to be used. Doping has traditionally been used extensively in high performance silicon (inorganic) devices and it plays a significant role in their high performance. Yet, the advantages of doped organic semiconductors are being established only recently. Use of the dynamic doping, where mobile ions enhance the charge carrier injection and facilitates high current densities is being increasingly made in organic light emitting electrochemical cells.

Use of the high work function electrodes for both the cathode and the anode is possible because of the dynamic doping in electrochemical light emitting cells[101]. LECs typically are obtained by blending a luminescent semiconductor polymer and an ion conducting polymer electrolyte. These devices emit light on

the application of voltages, at voltages slightly greater than the energy gap of the polymer divided by the elementary charge[101]. The relocation of ions on application of voltage towards respective electrodes, leading to the p and n doping of the polymer in specific regions and allowing easy injection and transportation of holes and electron, makes these devices interesting. However, the blend of hydrophobic polymer semiconductor with hydrophilic electrolyte makes this device unstable due to the phase separation[89] [133] [29] [131] issues which affects the life-time of these devices.

In order to overcome the phase separation issue, Sandstrom et al[113] have recently proposed the bilayer planar LEC approach by separating the ion and electron transport with superyellow and poly(ethylene oxide) (PEO) and KCF_3SO_3 system in vacuum at temperature, T= 360K. In chapter 4 we have shown independently that the electroluminescence in ion gel gated polymer transistors are of this nature.

The same transistor can be used in a bilayer mode. When the third terminal, gate electrode is not present for the voltage modulation across the gel, but the potential difference is applied only across the source and drain electrodes the device acts in a bilayer, planar device mode.

In ion gel gated transistors, the ion gel dielectric facilitates the gate electrode to be offset from the channel. This is possible due to[97] [15] the 'motion of ions' on the application of voltage which leads to the capacitance. High ionic conductivity of the ion gels which leads to high capacitance at the interface enables high charge carrier density in the semiconductor channel.

However, when the motion of ions is not stopped at the ion gel and polymer semiconductor interface but the ions penetrate into the polymer, we have shown in chapter 4 that, these transistors are not purely electrostatic field effect transistors but due to the significant contribution of ions incorporated with the semiconductor, these transistors are electrochemical to an extent.

Further, based on the light emission results with ion gel gated transistors and mechanisms involved with the light emission behind these devices, we explore the bilayer planar LEC devices in this chapter. In this chapter we make use of the unique property of ion gels viz., motion of the ions depending on the potential difference across it irrespective of the location of electrodes[15] in combination

with the feasible ion penetration into the polymer layer underneath. Penetrated ions help in charge injection resulting in electroluminescence being possible at low voltages, while having the source and drain on the same plane makes it possible to have planar light emitting devices possible at room temperature.

To our knowledge, there has not been any report of room temperature bilayer with ion gels' LECs till date. We report that these devices operate at at room temperature at low voltages (of the order of the energy gap of the polymer semiconductor used) and due to the non mixing of ionic liquids[113] with polymers as opposed to ionic liquid LECs[84] the phase compatibility issues have been eliminated.

Further, we show that we can eliminate the absorption of emitted light by the metal electrode, by introducing the ZnO, a transparent electron injecting electrode. By shifting the recombination zone in the middle of the channel we report two orders higher EQEs. Also, we explore the possibility of moving the recombination zone into the channel by changing to a smaller cation in the ion gel. We report EQE values of 0.06% with changed cation in ion gel and show that the recombination zone moves approximately a micrometre away from the electron injecting electrode.

5.2 Polymer- Ion Gel Bilayer Planar LECs

In this section we continue the discussion of Poly(9,9'-dioctyl fluorene-co-benzo thiadiazole) F8BT polymer with 1-ethyl-3-methylimidazolium bis (trifluoro methyl sulfonyl)imide/ poly(styrene- block- ethylene oxide- block- styrene) EMIM-TFSI /SOS ion gel, from chapter 4. The device structure and fabrication method for these device is identical to that of polymer ion gel gated transistors except for the absense of the gate electrode in these devices. The fabrication method is documented in detail in chapter 3.

Figure 5.1 shows the schematic of the device structure of a planar bilayer light emitting device. These are simple planar bilayer devices and as their names suggest, they have electrodes on the same plane (planar) and have two layers (polymer and ion gel). The potential difference is applied across the electrodes. As both of the electrodes are of same metal (Au), either of them can be used as

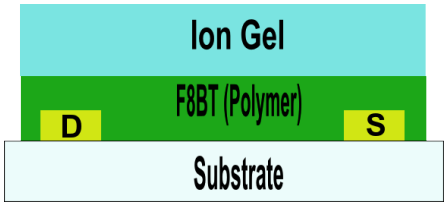

Figure 5.1: Schematic diagram for planar bilayer light emitting electrochemical cell

hole or electron injecting electrode.

The motivation for this study is to further understand the working principles of these bilayer devices, where the light emission occurs due to the presence diffused ions with or without applied gate voltage, as discussed in chapter 4.

5.2.1 Current Voltage Characteristics

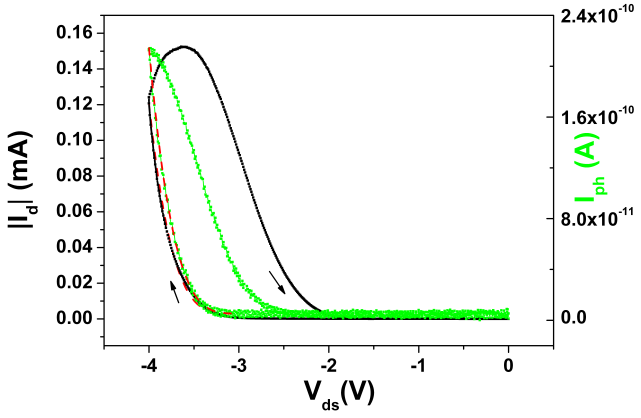

Figure 5.2: Variation of the current, (I_d), through the polymer block of thickness 40 nm and channel length, L = 40 μm, with the voltage (V_{ds}), super imposed with the variation of electroluminescence, with the voltage (green curve). The red line represents the power law fit for photocurrent and drain current with V_{ds}in the light emission regime during the forward scan. The onset voltage for shooting up of the current is -2.99 V and the onset for the light emission is -2.95 V based on the power law fit. (The voltage sweep rate is 25 mV/s).

We revisit the current-voltage characteristics of the bilayer devices in figure 5.2. Channel length of the tested device is L = 40 μm and the sweep rate is 25 mV/s. We can see the increase in current and the corresponding light emission

while the voltage is swept slightly above the energy gap of the polymer used. Increase of the current and the electroluminescence (photocurrent) both varies according to the power law and fits very well with the equation $y = b + k(x - a)^c$, where y is either the drain current or photocurrent, x is the potential difference V_{ds}, a is the onset voltage, $c = 4$ is the power that best fits the experimental data and k and b are arbitrary constants.

Based on the power law fit the onset voltage for shooting up of the current is -2.99 V and the onset for the light emission is -2.95 V. In order to keep the potential difference well within the electrochemical window we have not applied higher voltages across the device.

Since this measurement was carried out with a sweeping voltage, we can not comment on the absolute turn on time of the device at a constant bias voltage. Hence, we choose a voltage, slightly higher than the turn-on voltage and study the initiation and progress of light emission with time. The behaviour under a constant bias voltage is discussed in the following section.

5.2.2 Turn on Time and Lifetime at Fixed Voltage

We subject the device to a constant bias voltage of V_{ds} = -3.5 V, which is slightly higher than the turn-on voltage. At V_{ds} = -3.5 V, the turn on time is around 5 s. We define the turn on time as the time after application of a constant bias voltage where observable light emission occurs for the first time. After the turn on time, the intensity of the light emission gradually increases for some time indicating the continued doping with time until the depletion sets in [109] [37] and a p-n junction is formed within the polymer film.

A video recording of the device was performed starting simultaneously with the application of potential to determine the turn on time of the device and to study the growth of the light emission with time as well as the device's life time. Figure 5.5 show snapshots from the video recording showing microscopic images of the light emitting bilayer device at various time intervals.

Though we start seeing the light emission within 5 s of applying a bias voltage of -3.5 V, it can clearly be seen through these set of images that it takes about 15 minutes to reach the steady state.

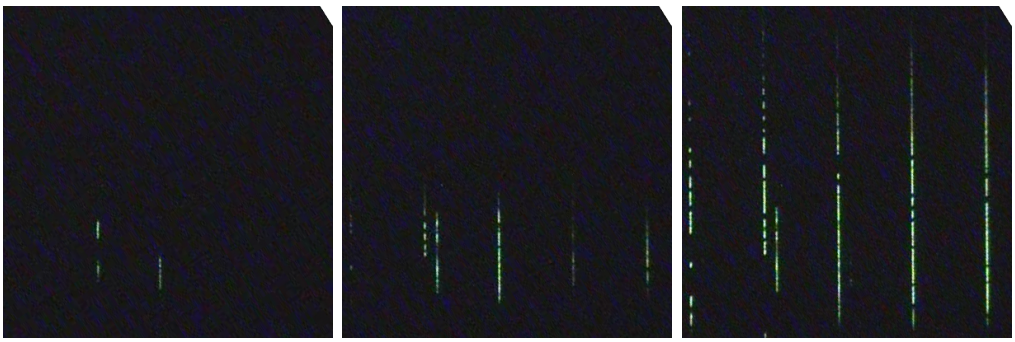

Figure 5.3: (a) Electroluminescence image 32 seconds after the application of 3.5V across the device, (b) 3 minutes 32 seconds, (c) 5 minutes 25 seconds

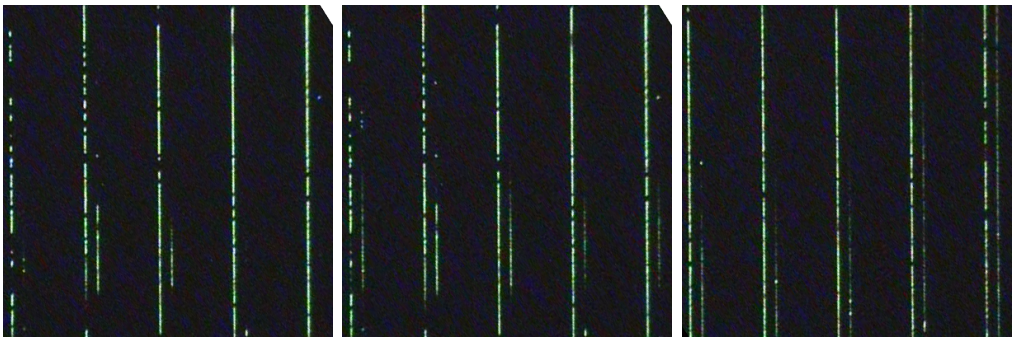

Figure 5.4: (a) 8 minutes 15 seconds, (b) 10 minutes 2 seconds, (c) 11 minutes 29 seconds

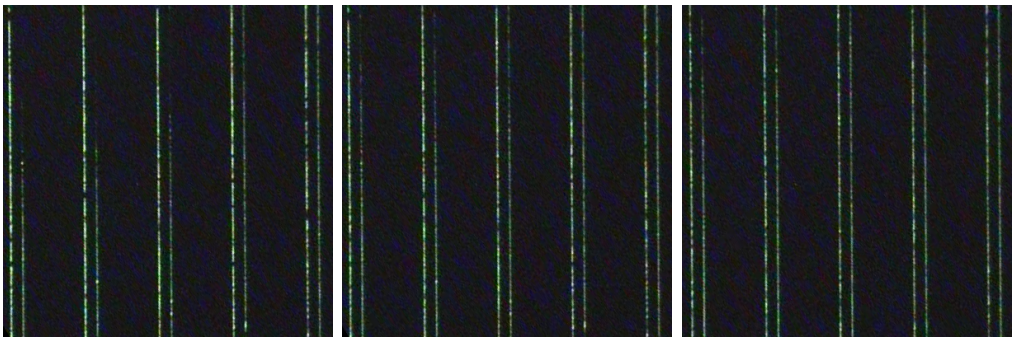

Figure 5.5: (a) 15 minutes 20 seconds, (b) 21 minutes, (c) 30 minutes 26 seconds

Between 15 minutes to 100 minutes the device appears to have attained a steady state. However, if we carefully observe these light emission images of these interdigitated bilayer devices, we see that the light starts growing at one edge of the electrode to start with and the the same follows with the other edge later. While the device starts dying, the same pattern continues, with the light

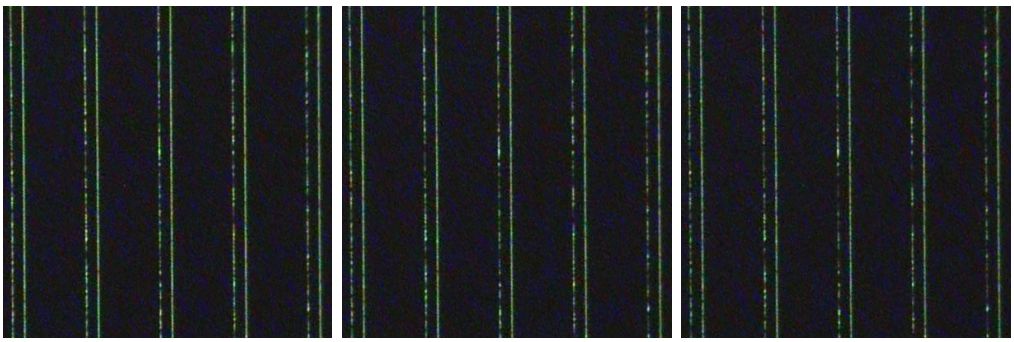

Figure 5.6: (a) Electroluminescence image 60 minutes 10 seconds after the application of 3.5V across the device, (b) 70 minutes 5 seconds, (c) 80 minutes 28 seconds

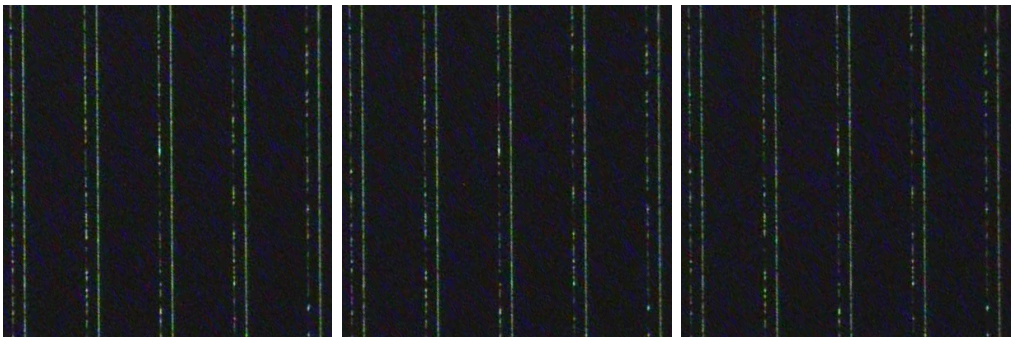

Figure 5.7: (a) 90 minutes 22 seconds, (b) 100 minutes 17 seconds, (c) 110 minutes 11 seconds

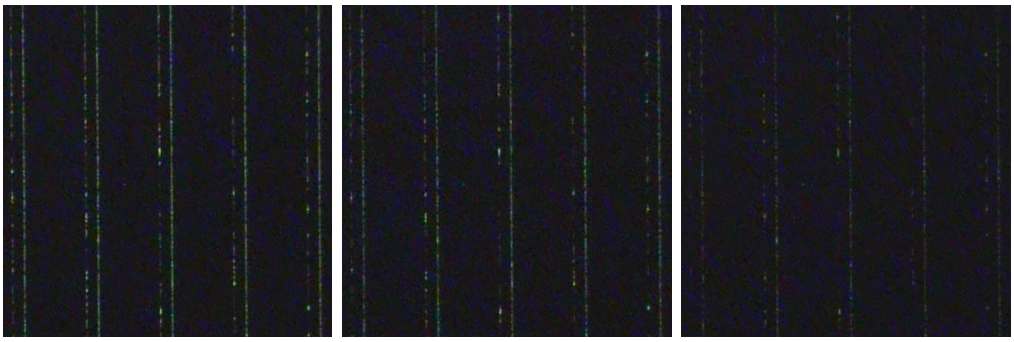

Figure 5.8: (a) 120 minutes 32 seconds, (b) 158 minutes 6 seconds, (c) 196 minutes 53 seconds

near first edge of the electrode reducing in brightness first, followed by the other edge. Building up of the p-n junction initially takes some time, then reaches its steady stage and eventually it dies. Overall, the device was emitting light about 190 minutes at -3.5 V, with steady light emission of around 70 minutes.

Non-uniform electroluminescence near two different edges of the interdigi-

tated metal electrodes might be due to the difference in the morphology of the photolithographically patterned electrodes and the possible dissimilar chemical composition at different edges. While evaporating the metal (Au) electrodes, a slight change in the angle of the surface on which metal is being evaporated can introduce inhomogeneous thickness which in turn introduces the difference in electron injection.

The gradual lowering of the light output can be seen with last couple of images (158 and 196 minutes). Although the device death occurs ultimately, a combination of short turn on time with long build up and steady states makes the useful life of the device relatively long. The death of the device might be due to the high current densities and hence high junction temperatures which might degrade the material resulting in reduction of the light emission. If the degraded devices are tested after several minutes, they resume electroluminescence, further providing an evidence for their thermal degrading. Although in ion gel-polymer bilayer LECs we have overcome the problem of phase separation, compared to OLEDs, the device life time is shorter possibly due to these effects.

Another interesting point worth noting here is that, the higher the voltage applied across the electrodes (with the fixed channel length), the sooner the device turns on. So, there is no absolute turn on time for a device of certain channel length, but it depends on the potential difference across the device significantly. The larger the voltage, the faster is the doping and formation of the p-n junction is quicker. This explains the quicker turn on time with higher voltages. The larger the potential difference across the device, the larger are the current and photocurrent (electroluminescence).

5.2.3 Recombination Zone Profiles

The location of the recombination zone is of prime importance in light emitting devices as it can play a significant role in determining the external quantum efficiency of the devices. When excitons recombine radiatively near the electrodes, resulting in a recombination zone next to the electrode, metal electrodes can cause the absorption of the emitted light, reducing the external quantum efficiency [5]. Conversely, a recombination zone occuring away from the electrode implies a

lower light absorption by the electrodes and hence a higher external quantum efficiency.

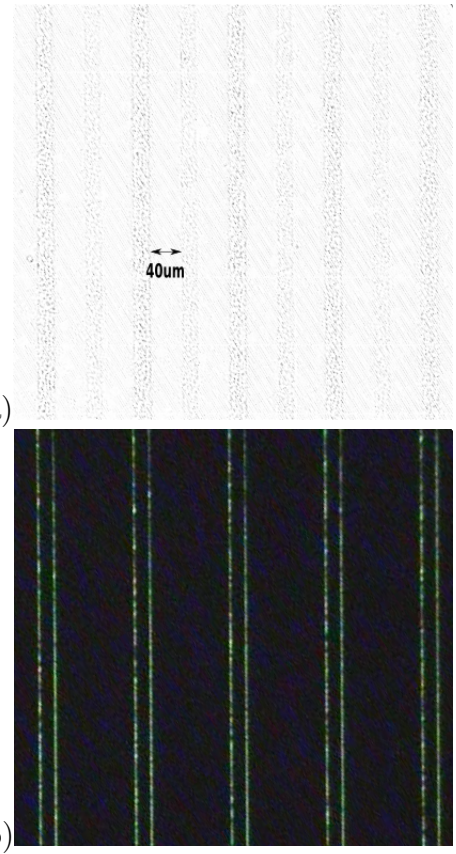

Figure 5.9: (a) Reference image: interdigitated electrode pattern (b) Microscope image of the light emitting device corresponds to the reference image.

With these electron transportation limited devices (refer section **??**), the recombination of holes and electrons happens in the proximity of the electron injecting electrode. Figure 5.9 shows the reference interdigitated electrodes and the light emission image from the same in comparison. The light emission at the edge of the electron injecting electrode can be seen.

Figure 5.10 can be used to analyse the exact location of the recombination zone and the zone width from the above shown images. Figure shows pixel brightness values from the reference image and light emission image on an arbitrary scale. The black curve represents the electrode, the peak area represent the metal electrodes and the flat region being the channel. The red curve is from light emitting

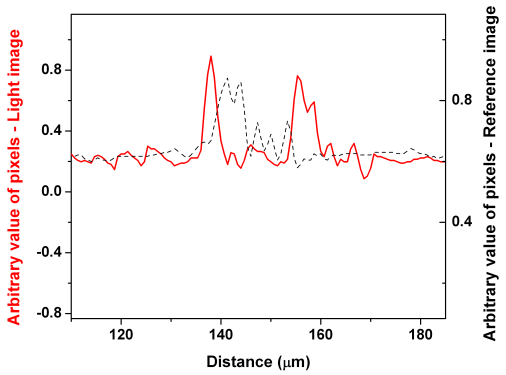

Figure 5.10: The location of the recombination zone: The black dotted curve represents the reference electrodes where the peaks corresponds to metal electrode area and the flat region represents the channel, and the red represents pixels from the light emission image.

image, where the red peaks are the bright pixels representing the recombination zone. The width of the peak at half maximum is about 2 to 3 μm on average at V_{ds} =-3.5 V The figure shows how the light emission starts right next to the electron injecting electrode, falling slightly on the edge of the electrode.

5.2.4 Fluorescence Probing During Device Operation

In order to understand the p-n junction formation and doping of the polymer with the ions penetration, we carried out fluorescence probing during the device operation. We choose the channel length of the device 200 μm, long enough to make the time scales involved in light emission build up and decay more easily observable.

Figures 5.11 through 5.19 shows the fluorescence probing of the bilayer device with inter electrode spacing, L = 200 μm, under the voltage application of constant 3.5 V with time. Within a few seconds of the application of the voltage, the photoluminescence of the polymer next to the hole injecting electrode starts to diminish and the image looks darker in this region. As time increases (with 3.5 V being applied continually) the doped region increases its dimension or in other words, it propagates towards the other electrode. This is conventionally p doping of the polymer due to the penetration of negative ions into the polymer.

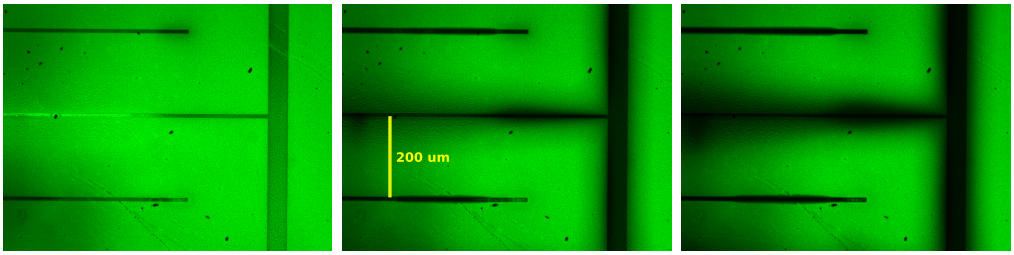

Figure 5.11: (a) Pristine device before application of voltage.(b) 1 second after the application of voltage (the vertical electrode seen in pictures is given a positive voltage of 3.5V (c) After 19 seconds

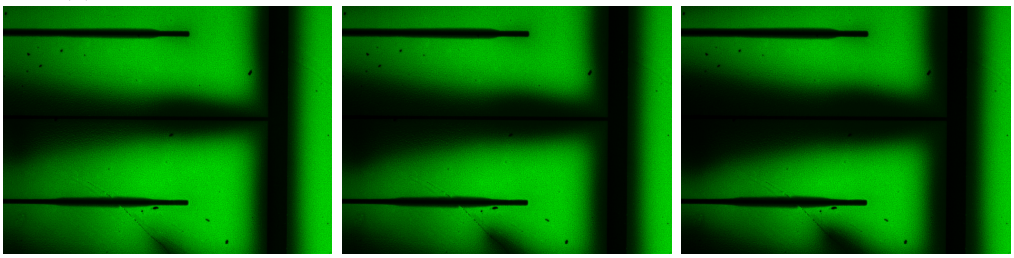

Figure 5.12: (a) 39 seconds (b)57 seconds (c) 73 seconds

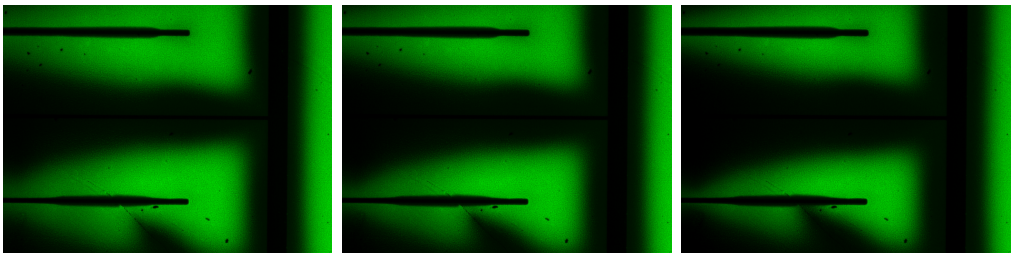

Figure 5.13: (a) 87 seconds (b) 101 seconds (c)125 seconds

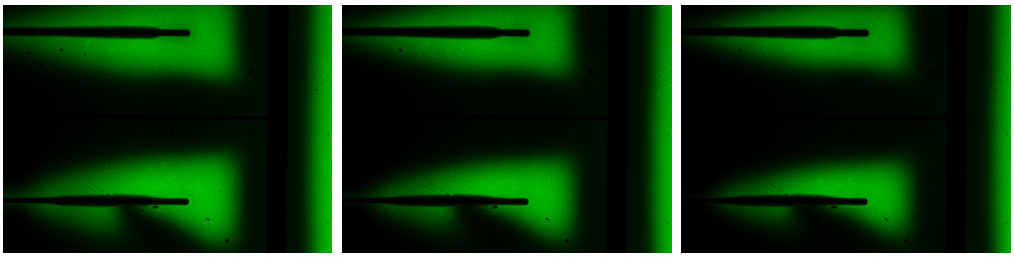

Figure 5.14: (a) 141 seconds (b) 163 seconds (c) 183 seconds

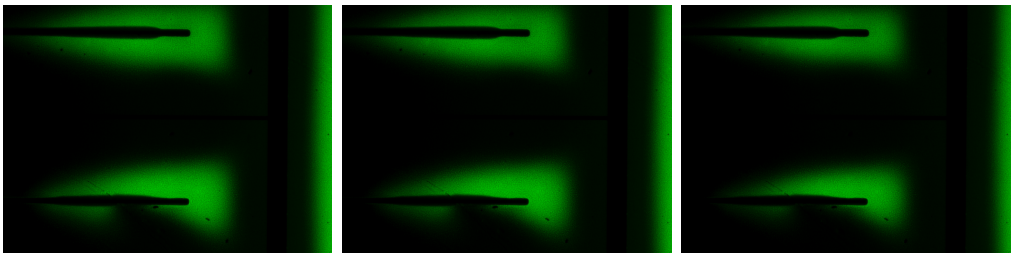

Figure 5.15: (a) 191 seconds (b) 203 seconds (c) 229 seconds

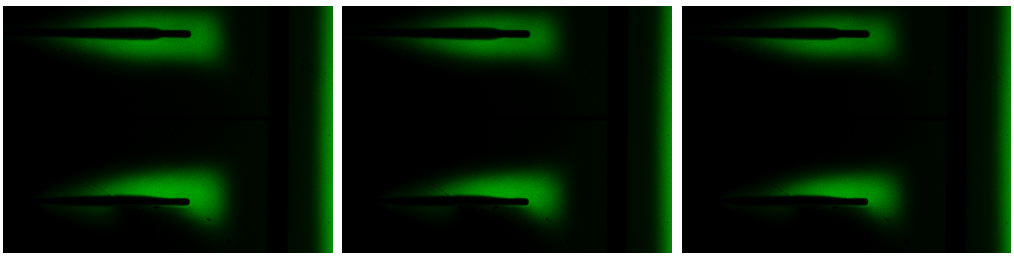

Figure 5.16: (a) 245 seconds (b) 267 seconds (c) 281 seconds

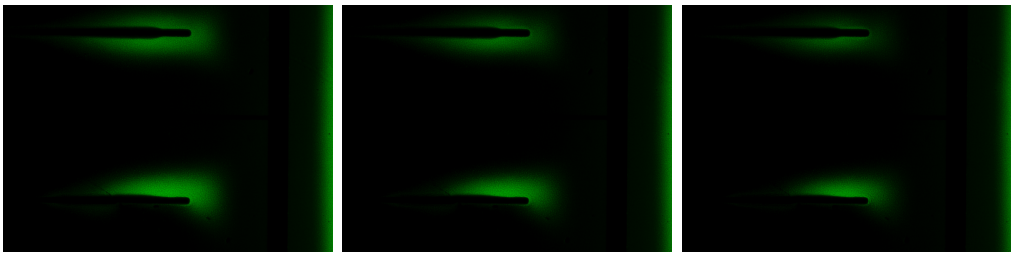

Figure 5.17: (a) 293 seconds (b)319 seconds (c) 341 seconds

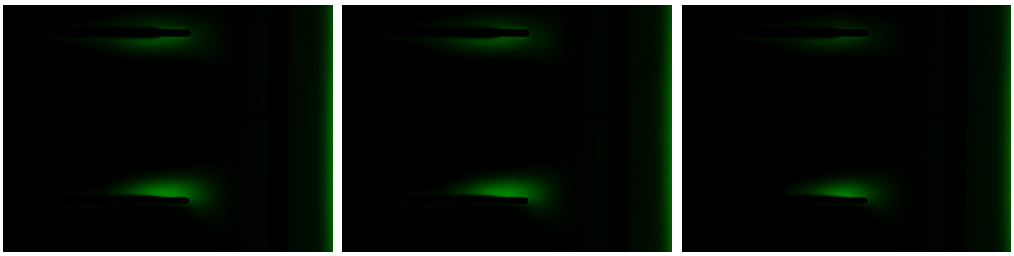

Figure 5.18: (a) 353 seconds (b) 367 seconds (c) 381 seconds

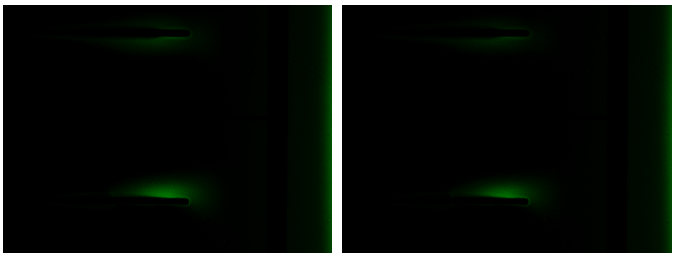

Figure 5.19: (a) 391 seconds (b)407 seconds

This migration in turn induces more and more hole injection and hence more p doping[47].

At the other electrode, PL quenching of extremely small region indicating the presence of few $EMIM^+$ ions in the polymer can be seen and it almost remains constant with time. This does not propagate as fast as the p doping does, with time, indicating a much larger diffusivity of negative ions compared to positive

ions.

$TFSI^-$ions quenche the whole channel (200 μm) in about 7 minutes time with -3.5 V. The device lives for more than three hours indicating that the light emission is coming from the photoluminescence quenched region of the semiconductor. 200 μm channel devices turn on around 130 seconds at V_{ds}= -3.5 V. Analyzing the recombination zone location and width and the PL quenching region next to the electron injecting electrode shows that the light emission is coming from the doped region itself which could be the prominent factor in deciding the quantum efficiency of the device.

We develop a theoretical and numerical model to qualitatively and quantitatively explain the movement of $TFSI^-$ ions within the semiconductor layer. The model and its results are discussed in chapter 6.

With $TFSI^-$ diffusivity being significantly larger compared to $EMIM^+$ (as evident from fluorescence probing, section 5.2.4) ions, hole current shoots up consequently. The hole current increases artificially due to p doping (section 4.2.9). However, the electron current remains mostly intrinsic, though few $EMIM^+$ ions next to the negative electrode do assist the electron injection. $EMIM^+$ ions however, are not helping the electron transport in the bulk as they do not diffuse further into channel. Or in other words, by the time p-doping propagates towards the electron injecting electrode, the n-doping happens only in the very vicinity of electron injecting electrode (See figures 5.11 through 5.19).

This not only shifts the recombination zone towards the cathode but also contributes towards a disproportionate number of holes compared to number of electrons available. Large number of holes and smaller number of electrons might affect the total number of excitons formed and hence the external quantum efficiency of the devices as well.

Presence of a large number of ions within the polymer and consequent PL quenching[57] result in the reduction of EL from this region. However, with the available resolution of PL quenching and origin of EL images, it is very hard to decide whether EL we see originates from thin pure neutral F8BT (p-i-n junction)[101] or not. Rather, it would be meaningful to say the light emission happens where the p and n junctions meet and we are uncertain as to whether it is p-i-n junction[101] or just p-n junction[109].

5.3 Planar Bilayer LECs with Transparent ZnO Electrode

In an effort to increase the EQE by eliminating factors like metal electrode absorption of emitted light we introduce transparent ZnO electrode[39]. ZnO electrodes can be employed to extend the electron injecting electrode well away from the metal electrode. In order to shift the recombination zone to the center of the channel transparent ZnO had been patterned on the top of Au electrode till the middle of the inter electrode space (channel length). Figure 5.20 shows the schematic of the same in the top view.

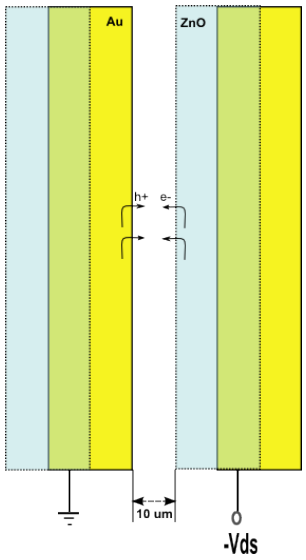

Figure 5.20: Schematic diagram (top view) of ZnO till the middle of inter electrode space which makes effective channel length, L= 10 μm.

Introducing transparent ZnO till the middle of the channel promptly shifts the recombination zone to the edge of ZnO, where the electron injection takes place, from the edge of the electron injecting Au electrode in earlier case. Since the ZnO edge is patterned in the middle of the channel, the recombination zone falls in the middle of the channel. Figure 5.21(a) shows the light emission in the middle of the channel right next to the ZnO electrode.

5.3.1 Recombination Zone Location

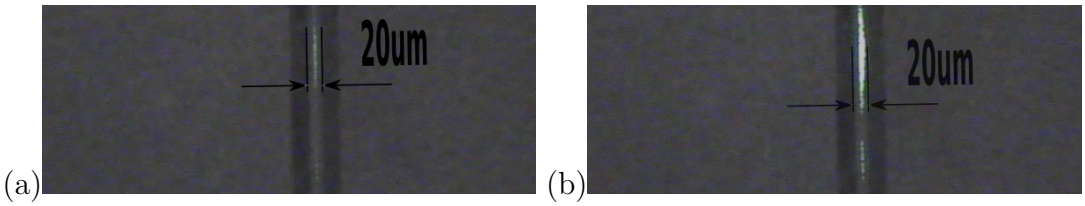

Figure 5.21: (a) Light emission from the middle of the channel in ZnO patterned bilayer device, at lower V_{ds}. (b) Thickening of the light emission towards the hole injecting electrode, with increasing V_{ds}.

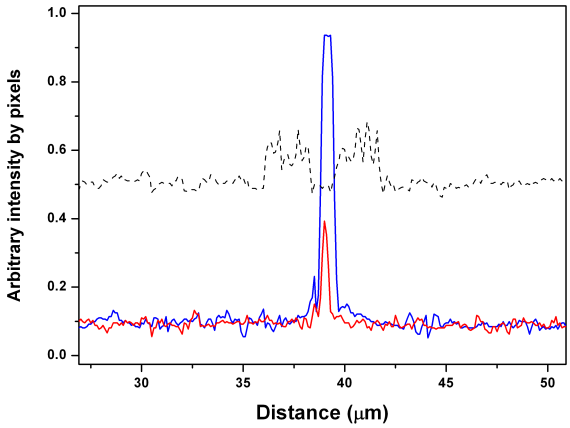

Figure 5.22: The location of the recombination zone analysis, where black dotted curve represents the reference electrodes where the peaks corresponds to metal electrode area and the dip represents the channel of length 10 μm. The blue curve represent the light emitting device images at lower V_{ds} value (during the beginning of the light emission) and red curve represents the light emitting device images at higher V_{ds} value (approximately 4 V) (as shown in figure 5.21(a) and (b) respectively.

The broadening of the width of the recombination zone towards the Au electrode with higher voltage can be seen from the figure 5.21(a) and (b). With the increasing voltage, the recombination zone width increases towards the hole injecting electrode. Figure 5.22 analyses the location and the width of the recombination zone. The black dotted curve represents the reference electrodes where the peaks corresponds to metal electrode area and the dip represents the

channel of length 10 μm. Red curve represents the thin light emission in the middle of the channel, which becomes thicker with the voltage(blue curve). The broadening effect of the recombination zone with higher voltage is evident. The maximum recombination zone width is about 7 μm indicating the presence of trapped electron about 7μm away from the electron injecting electrode.

The external quantum efficiency of the device reaches two orders high (1.27×10^{-2}) (see table 5.1) due to the transparent ZnO as an efficient electron injector[49], compared to bare Au as electron injecting electrode (2.64×10^{-4}). This is presumably due to a combined effect of more balanced electron and hole currents due to better electron injection and lower exciton quenching at the electron injecting electrode.

5.3.2 Current Voltage Characteristics

Figure 5.23(a) shows the current voltage characteristics of the device with electron injection through the ZnO electrode, with the effective channel length, L= 10 μm. Figure 5.23 (b) shows the electroluminescence (photocurrent) variation with V_{ds}. Sweep rates 25 mV/s.

With these bilayer devices of 10 μm inter electrode space as well, the trend of increasing electroluminescence with time can be observed consistently, as shown in figure 5.23. Both current and electroluminescence increase with subsequent sweeps to start with and then gradually the trend reverses. The different rate of growth and fall for drain current and the electroluminescence can be observed. The drain current keeps increasing till the 7th sweep however the electroluminescence intensity reaches its maximum in second sweep and starts falling from the third sweep. The gradual building of the p-n junction and the building of the EL with time is evident.

Figure 5.24 shows the exponential decrease of the EQE with consequtive sweeps. From the first sweep to the second sweep, there is an increase in the value of the external quantum efficiency but then onwards, it falls with subsequent sweeps exponentially. We recall the exponential EQE fall with gate voltages reported in chapter 4.

The table 5.1 lists the onset voltage for shooting of the drain current and

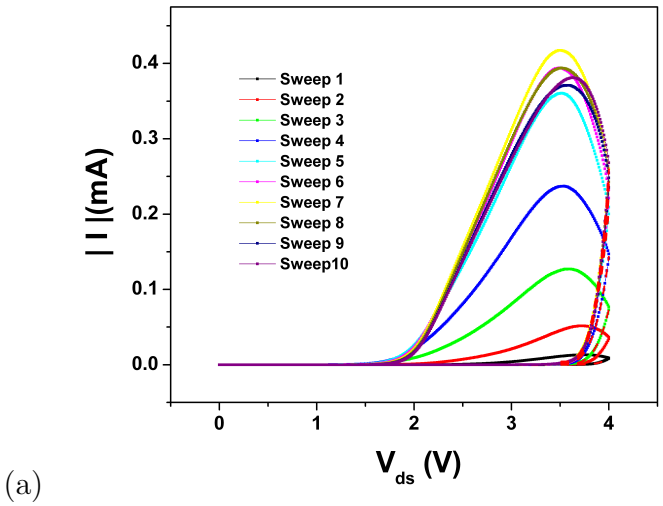

(a)

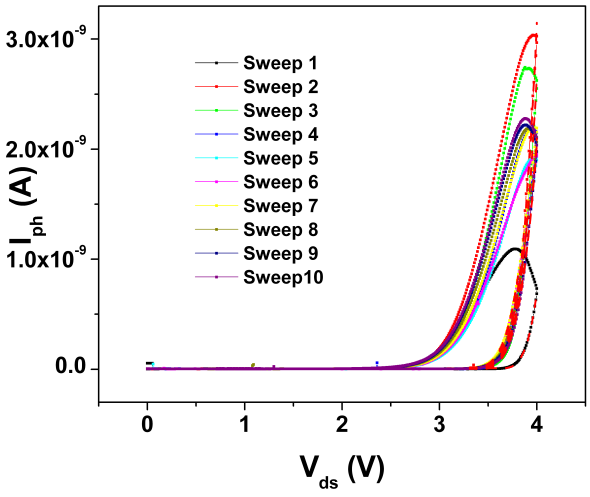

(b)

Figure 5.23: (a) Current Voltage characteristics with different sweeps (b) The corresponding electroluminescence variation with voltage

photocurrent (electroluminescence) based on the power law fit during the forward scan in the light emission regime for different sweeps. This is done in order to compare the parameters with the gate modulation, with same sweep rates. In order to see whether we see a real gate modulation effect in the light emitting regime or whether it is just an artifact of the effect of time that we claim as gate modulation, this is necessary.

Onset Dependency With Different Sweeps			
Sweep	V_{onset} for I_d (V)	V_{onset} for I_{ph} (V)	EQE (%) at 4 V
1	3.58	3.57	1.27×10^{-2}
2	3.52	3.37	1.33×10^{-2}
3	3.48	3.37	5.40×10^{-3}
4	3.41	3.33	2.29×10^{-3}
5	3.40	3.25	1.46×10^{-3}
6	3.42	3.26	1.34×10^{-3}
7	3.42	3.24	1.34×10^{-3}
8	3.44	3.27	1.31×10^{-3}
9	3.47	3.29	1.29×10^{-3}
10	3.46	3.34	1.23×10^{-3}

Table 5.1: Variation of the onset voltages and EQE for consecutive sweeps.

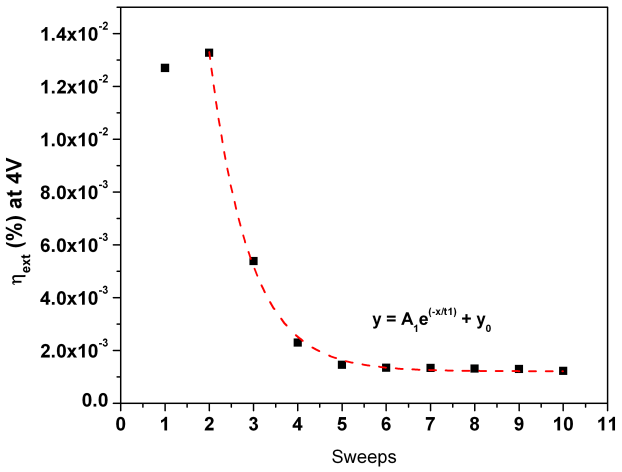

Figure 5.24: Exponential fall of the EQE with subsequent sweeps. From sweep 1 to sweep 2, an increase in EQE however is evident.

In the next section under the gate voltage modulation, the same parameters w.r.t different gate voltages are tabulated. This allows us to investigate clearly whether the onset voltage dependency and external quantum efficiencies really vary with the gate modulation in LEC regime.

5.3.3 Gate Voltage Modulation of Onset Voltage and EQE

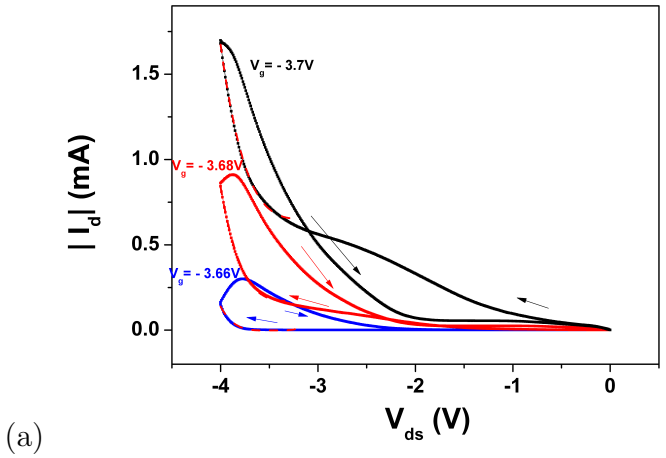

(a)

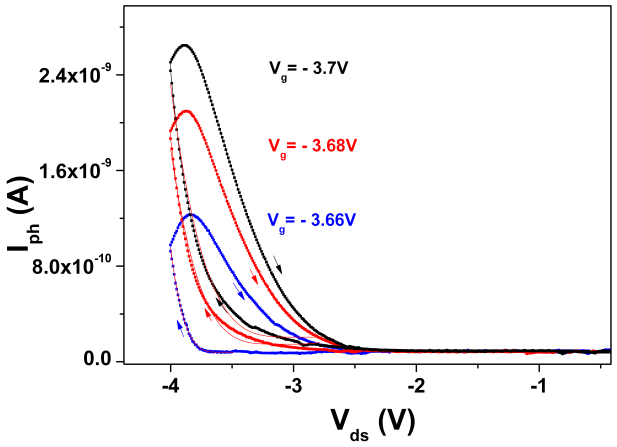

(b)

Figure 5.25: (a) The variation of I_d with V_{ds} in transistor and LEC regime, while the effective channel length, L= 10 μm. (b) The variation of the photocurrent (electroluminescence) under the gate modulation with V_{ds}.

Figure 5.25 (a) shows the variation of I_d with V_{ds} under the gate modulation (with three different gate voltages in hole accumulation regime). Contact resistance feature with the first applied gate voltage (-3.66 V) is evident. This feature disappears with the next gate voltage (-3.68 V) and we see well saturated current below V_{ds} = -2 V. We have discussed that the onset voltage and EQE of these bilayer devices vary with consecutive sweeps. The onset voltage and EQE also

vary with the gate voltage as discussed in chapter 4. Whether the gate voltage is applied or not, since the measurements are carried out with a sweeping voltage, there is also a inherent contribution of time dependent ion penetration in affecting the onset voltages and EQEs. In order to isolate the effect of gate modulation with the effect of time and to establish that the bilayer devices indeed exhibit gate modulation, in this section we report studies of bilayer devices with a gate electrode in comparison.

The device structure used for the these gate modulation comparison studies is identical to the bilayer device with patterned ZnO electrode but an evaporated gold electrode is introduced on the top of the gel layer. The thickness of the evaporated gold electrode was about 70 nm. The location of the gate electrode is offset from the channel to facilitate optical measurements.

1. With Gate Modulation			
V_g (V)	V_{onset} for I_d (V)	V_{onset} for I_{ph} (V)	EQE (%) atV_{ds}=-4 V
-3.66	-3.48	-3.57	9.2×10^{-4}
-3.68	-3.18	-3.08	3.41×10^{-4}
-3.7	-3.02	-2.95	2.3×10^{-4}

Table 5.2: Change in onset voltages and external quantum efficiencies with gate modulation.

Figure 5.25 (b) shows variation of the corresponding photocurrent(electroluminescence) under the gate modulation and table 5.2 lists the dependency of the onset voltages and EQE at -4 V. Figure 5.26 and table 5.3 show the corresponding data for the same device but for subsequent sweeps. The variation in onset voltage and EQE between these data sets can hence be attributed to the inherent time dependent ion migration into the polymer slab.

From comparison of table 5.1, where the onset voltages and EQE values are listed with consecutive sweeps with same sweep rates and from tables 5.2 and 5.3 where the same sweep rates are maintained, it is very clear that the dependency of V_{onset} voltages on the gate voltages is not an artifact of time. Tables 5.2 and 5.3 show the data corresponding to the same device but from successive measurements.

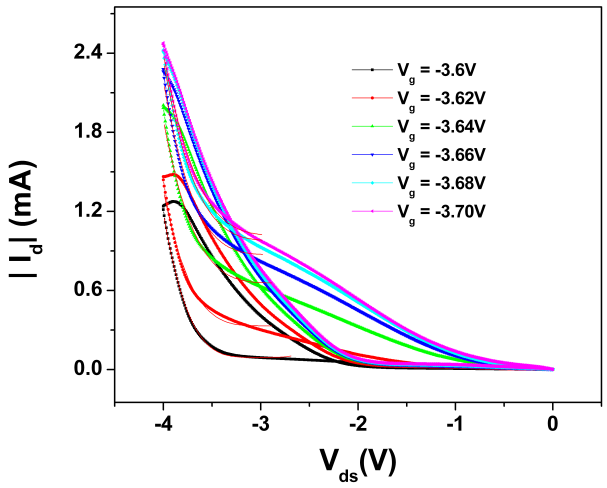

(a)

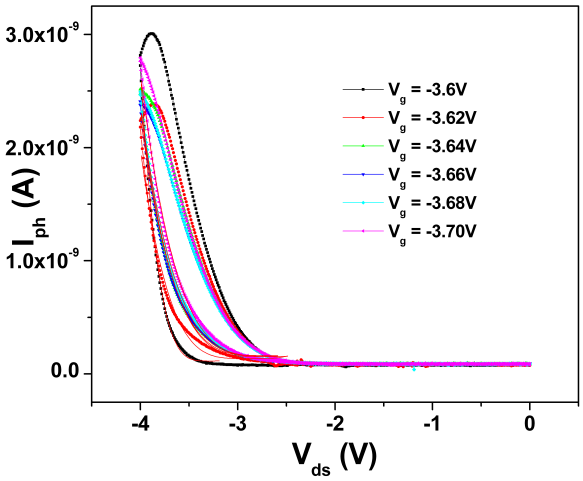

(b)

Figure 5.26: (a) The variation of I_d with V_{ds} and (b) Photocurrent with V_{ds} under the gate modulation in Transistor and LEC regime.

From the first sweep to the tenth sweep, in table 5.1 V_{onset} for the light emission varies not more than by 0.32 volts. Whereas with gate modulation, in table 5.2 V_{onset} for light emission varies 0.62 volts for three gate voltages (equivalent to 3 sweeps) and 0.7 volts for six different gate voltages (6 sweeps), varying in steps of 0.2 V. It is evident that onset voltages can be modulated by using gate terminal even in the LEC regime.

2. With Gate Modulation			
V_g (V)	V_{onset} for I_d (V)	V_{onset} for I_{ph} (V)	EQE (%) at V_{ds}=-4V
-3.60	-2.98	-3.27	3.45×10^{-4}
-3.62	-2.89	-2.87	2.33×10^{-4}
-3.64	-2.75	-2.68	1.93×10^{-4}
-3.66	-2.76	-2.65	1.62×10^{-4}
-3.68	-2.71	-2.59	1.57×10^{-4}
-3.7	-2.64	-2.57	1.72×10^{-4}

Table 5.3: Data from subsequent sweep of the same device for change in the onset voltages and external quantum efficiencies with gate modulation.

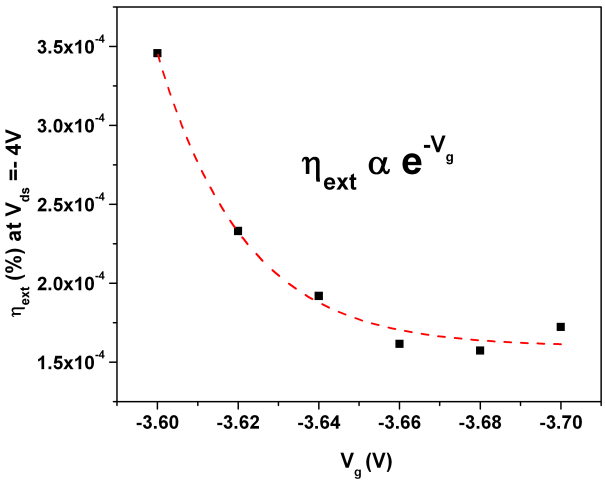

Figure 5.27: The fall of the EQE with V_g.

For EQE, values in table 5.2 are higher compared to the EQE values in table 5.3. This can be explained by increasing doping levels with time reducing the EQE of the devices. The trend of the EQE variation is an exponential fall with (figure 5.27) or without (figure 5.24) a gate voltage, which might be due to associated photoluminescence quenching. The absolute value of EQE is lower with the gate modulation and higher without the gate modulation.

When there is no gate voltage, (table 5.1), the EQE values are 1-2 orders of magnitude higher when compared to the EQE values with a gate voltage modulation (table 5.2 and table 5.3). This implies that the effect of gate voltage is

to increase the doping of the semiconductor and consequently decrease the EQE of the device, when modulated to accumulate holes. The highest values of EQE from the device occur when there is no such applied gate voltage.

5.4 Bilayer LECs with different Cation

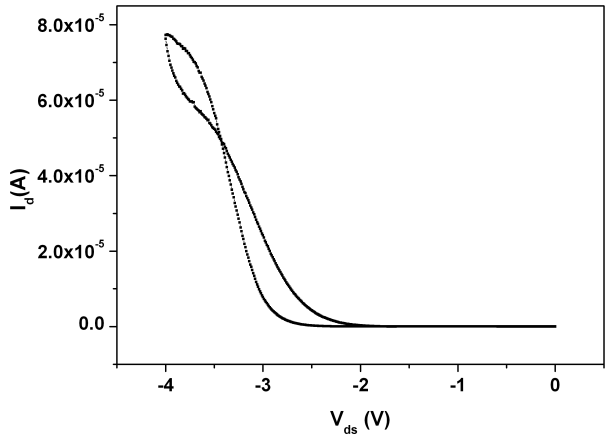

(a)

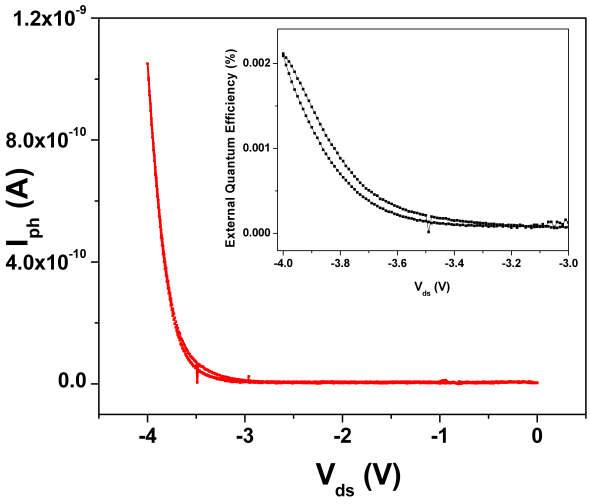

(b)

Figure 5.28: (a)Variation of current and (b) Photocurrent (electroluminescence) with voltage with EQE shown in the inset with maximum value up to 0.002%

In order to increase the external quantum efficiency of these device we experi-

mented with another method by replacing the $EMIM^+$ ions with $BMPY$ ion in ion gel layer in otherwise identical Au-Au electrode devices. The motivation of having the different cation is to have the electron injection and eventually transportation due to the n type doping. This depends on the comparable diffusivity of both cations and anions on the application of the voltage which would then assist the injection of both charge carriers. The semiconductor and ion gel interface that would favour electron transoportaion is also an other key factor. Since the location of the recombination zone strongly depends on mobility of holes and electrons it is very desirable to have them balanced.

In this section we discus F8BT polymer with 1-butyl-4-methyl pyridinium bis(trifluoro methane sulfonyl)imide (BMPY-TFSI)/ poly(styrene- block-methyl methacrylate- block-styrene) SPMMAS ion gel bilayer devices. The fabrication method is documented in detail in chapter 3.

We observe that the trend of initial increase and subsequent decrease of the current continues with these devices and appears to be a common feature of all bilayer LECs.

Figure 5.28 and figure 5.29 shows variation of current and electroluminescence with voltage for two different sweeps. Inset shows corresponding EQEs. EQE goes up to 0.06% from maximum of 0.02% from its earlier sweep. This happens not just because of the building up of the EL but also due to significant fall in the current. This is an interesting feature with BMIM-TFSI/SPMMAS gel bilayer devices as opposed to EMIM-TFSI devices. The drain current fall starts before the fall in the electroluminescence leading to higher EQEs.

The EQE value varies with V_{ds}. The higher the voltage across the device, the higher is the potential drop across the p-n junction and the higher is the diode current and electroluminescence. However, we can not increase the V_{ds} indefinitely, owing to the electrochemical window of the ion gel used. We note that when compared to the EQE of the F8BT EMIM-TFSI devices, this is two orders higher.

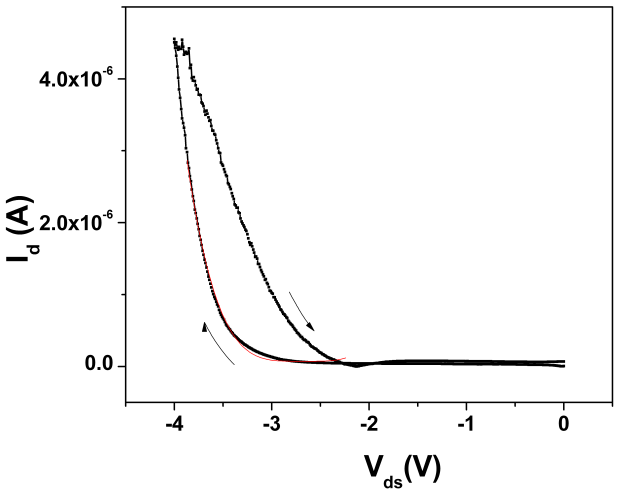

(a)

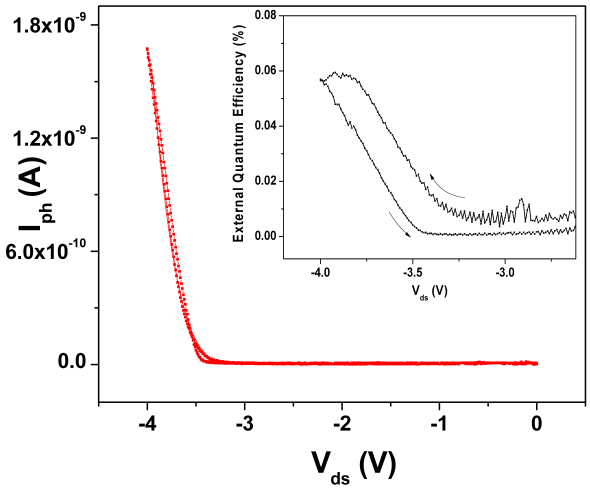

(b)

Figure 5.29: (a) Variation of current and (b) Photocurrent (electroluminescence) with voltage with EQE shown in the inset with maximum value up to 0.06%

5.4.1 Recombination Zone Location

Figure 5.30 shows the light emitting device image superimposed on the reference device image in order to see the location of the recombination zone.

Figure 5.31 shows the location of recombination zones. We note that the recombination zone locations on either edges of an electrode are different. On one side of the interdigitated metal electrodes, the recombination zone falls slightly

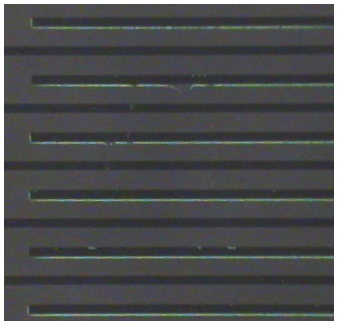

Figure 5.30: Image showing the light emission from the device, superimposed on the reference device image.

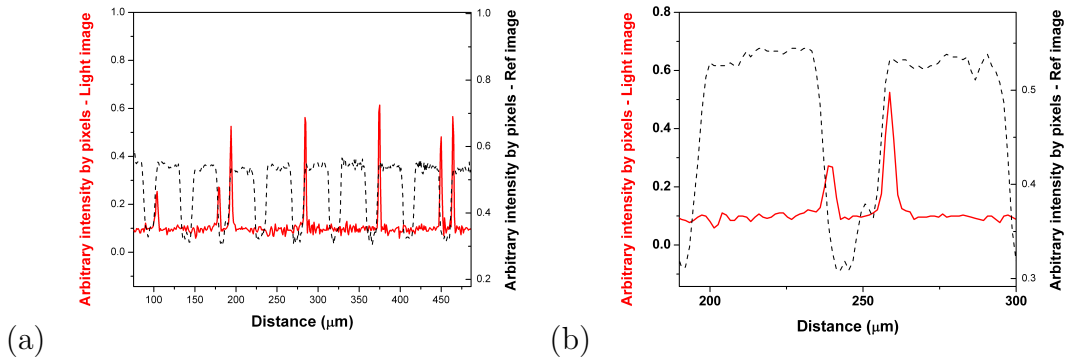

(a) (b)

Figure 5.31: (a) Location of the recombination zone. With Au electrodes. F8BT with BMPYTFSI/SPMMAS gel. Black dotted curve represents the reference electrodes with peaks corresponding to the channel area. (b) To a different scale highlighting the location of the recombination zone $\approx 1\mu m$ from one edge of the electrode whereas the same at the other edge falls on the gold electrode

away from the channel (about a micron as shown in 5.31(b)) and on the other side, if present, it falls on the metal electrode.

The recombination zone on one side of the electrode, contributes towards improving the EQE by falling into the channel approximately a micrometer away from the electrode. This eliminates the absorption of emitted light by the metal electrodes and the effect can be seen in the improved EQE values. The recombination zones on the other side of the electrode have either a diminished brightness or not present at all. When present, the recombination zone falls on the metal electrodes. This indicates that the light emitted from the recombination zone from one side of the electrodes gets absorbed by the metal electrodes, contribut-

ing towards the reduction of the EQE.

5.5 Bilayer LEC with ZnO Electrode and Different Cation

We have seen that by introducing the transparent ZnO as an electron injecting electrode we have increased the EQE of the F8BT, EMIMTFSI/SOS gel bilayer devices two order of magnitude higher. Also, by changing the anion ($BMPY^+$ instead of $EMIM^+$), we have shown that we can get higher EQEs such as 0.06% with F8BT. In this section, we investigate the effect of introducing ZnO for electron injecting layer instead of bare Au, in F8BT, BMPYTFSI/SPMMAS gel system.

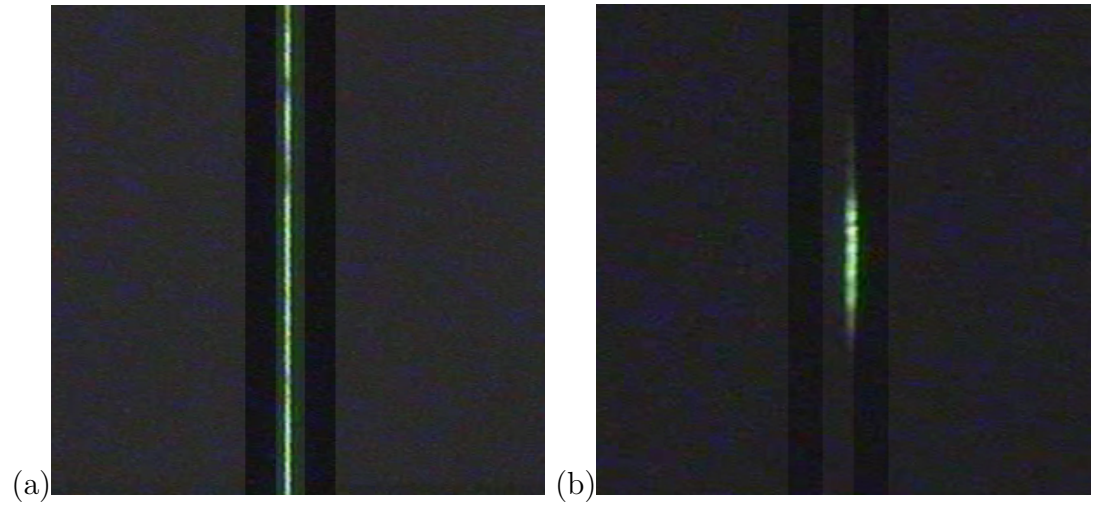

Figure 5.32: (a) Microscope image of light emission from the BMPY-TFSI/SPMMAS and F8BT bilayer device showing the recombination zone in the channel next to the transparent ZnO patterned edge. (b) Same device biased in such a way that holes are supposed to be injected from ZnO side (see appendix 7.2)

Figure 5.32 shows the prompt shift of the recombination zone right next to the region where ZnO has been patterned. The Electroluminescence (photocurrent) values go one order high compared with ZnO patterned F8BT, EMIMTFSI/SOS devices. But unfortunately, there is also a corresponding increase in the current and EQE values are not increased. Moreover, with the second and the third

sweep, device starts to degrade above 3.25 V and EL starts to fall with further sweeps. Table 5.4 shows the EQE values at 3.25 V and the onset voltages with different sweeps. It is quite puzzling why the EQE values are lower in this case by two orders compared to bare gold electrode F8BT, BMPY-TFSI/SPMMAS gel bilayer devices.

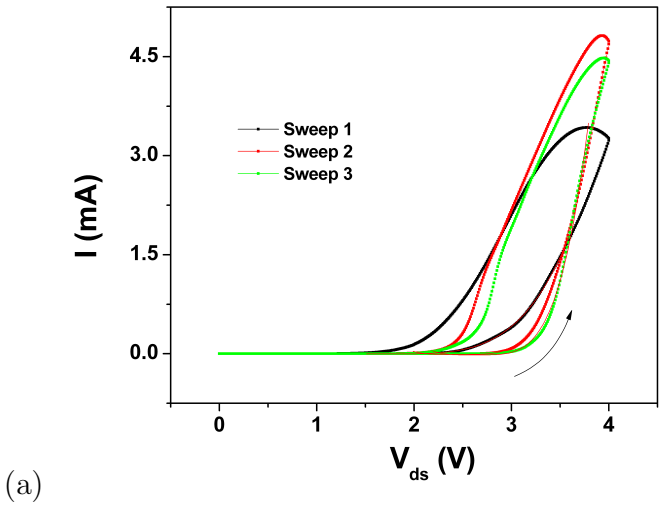

(a)

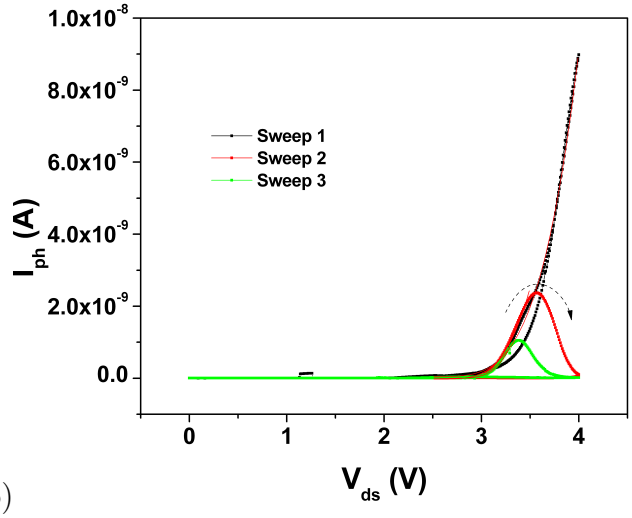

(b)

Figure 5.33: (a) Variation of current and (b) Photocurrent (electroluminescence) with voltage F8BT, BMPYTFSI/SPMMAS gel bilayer at subsequent sweeps. With ZnO as electron injecting electrode.

Onset and EQEs with different sweeps			
Sweep	V_{onset} for I_d (V)	V_{onset} for I_{ph} (V)	EQE(%) at 3.25 V
1	1.64	2.45	1.29×10^{-4}
2	2.45	2.49	2.86×10^{-4}
3	2.62	2.66	4.75×10^{-4}

Table 5.4: Variation of the onset voltages and EQEs at consecutive sweeps.

One possible explanation for this discrepancy is the time scales involved in these measurements. As we have seen with these LECs, electroluminescence builds up gradually, which means EQEs measured at different times can be different. Measuring the EQE with time at a fixed voltage as opposed to the voltage sweep would give us more detailed information about these devices.

5.6 Bilayer LECs with Different Polymers

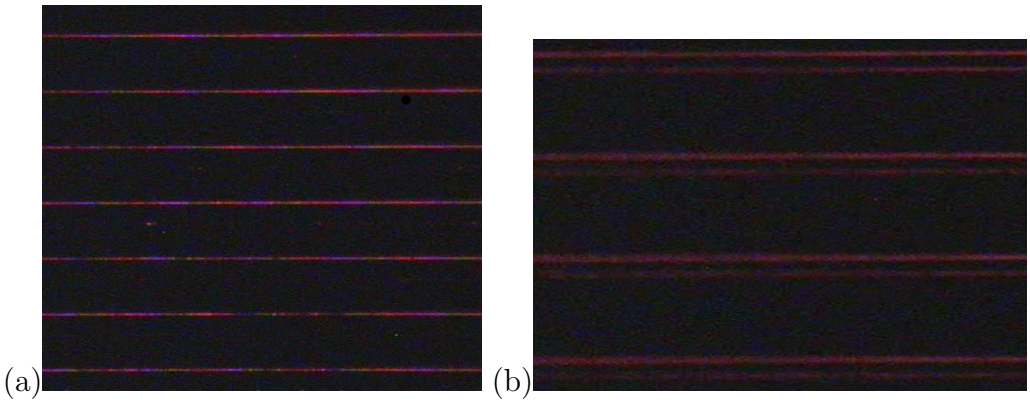

Figure 5.34: Image showing the light emission from the F8TBT polymer, BMPY-TFSI/SPMMAS gel bilayer devices with channel length (a) $10\mu m$ and (b) 40 μm.

Similar to F8BT we have tested F8T2, OC1OC10-PPV and F8TBT bilayer devices with ion gels. All these bilayer systems emit light at room temperature and recombination zone of the light emission is in the proximity of electron injecting electrode in all these cases indicating that it it is possible to achieve low voltage operating planar light emitting bilayer ion gel devices with a wide range

of polymers. Figure 5.34 shows the light emission from a F8TBT polymer gel bilayer device. There is a potential further to study these devices extensively.

5.7 Conclusions

To conclude we have shown that electroluminescence in bilayer of luminescent polymer(F8BT) with ion gel(EMIMTFSI/SOS) at room temperature is possible at very low turn on voltages due to the assistance of ions in charge injection, without any phase separation problem. We have studied the gradual building up of the light emission patterns and its steady state over a period of time and the eventual decrease in the electroluminescence.

We have shown the working mechanism of these devices is based on ion assisted doping which helps to eventually form the p-n junction by studying the fluorescence quenching of an operating device under UV illumination.

Holes move through the conductive doped region, whereas the doping regime is not in favour of movements of electrons for a long distance before forming the excitons that can recombine radiatively. Hence the recombination zone is in the very vicinity of the electron injecting electrode.

Due to the high diffusivity of the $TFSI^-$ ions as opposed to low diffusion or no diffusion of either $EMIM^+$ or $BMPY^+$ cations, the p-n junction formation eventually takes place in the very proximity of the electron injecting electrode. By introducing transparent ZnO as electron injecting electrode, we have shown that we can eliminate the metal absorption factor contributing towards the lower EQE and/or achieve better balance between the large hole current and the smaller electron current.

When we compare these devices with PMMA gated F8BT, LEFETs the photocurrent in both of these devices are the same, indicating the same number of excitons formation that recombine radiatively with both kind of devices. However, with ambipolar LEFETs there exists a balanced hole and electron mobility and the current through the device is at least three orders of magnitude lower. With Ion gel devices the electron current is considerably smaller than the hole current resulting in a significant imbalance, a reduction in the number of formed excitons and low EQE values. In addition, the presence of ions in the polymer

which is in the first instance the cause behind the light emission with these devices at such low operating voltages, itself is the main cause behind the lower EQE of these devices. Due to the presence of ions, drain current (hole current only) increases dramatically and shows its effect with a smaller EQE.

The presence of ions in the polymer quenches the photoluminescence of the device which in turn reduces the EL of the devices. Practically, we can not eliminate the quenching of PL of the polymer associated with the number of ions present in it, as the association of the ions is the driving factor behind the light emission around the voltages that corresponds to the energy gap of the polymer. This also mean that we can not reduce the high current densities that associated with these devices which is the side effect of ions helping the charge injection.

We have further shown that by introducing transparent electron injecting electrode shifting the recombination zone to the middle of the channel is possible which helped in increasing the EQE by the two orders by eliminating the absorption by metal (Au) electrode. Further, we had compared the EQE values with the gate modulation and with different sweeps with same sweeping rates and concluded that gate modulations can really change the onset voltages of the device, it's not just an artifact of time. However, from having the highest external quantum efficiency point of view, gate voltage is not really useful as EQE falls exponentially with gate voltages.

Furthermore, by changing the anion from $EMIM^+$ to $BMPY^+$ in gel layer we have shown the improvement in EQE values. We propose that with the suitable selection of ions in ion gel layer and luminescent polymer materials these room temperature low voltage operating devices with low power, without any phase separation problems have significant application potential.

Chapter 6

A Numerical Model for Ion Diffusion in Planar Bilayer LECs

6.1 Introduction

In a bilayer device with an ion gel layer on the top of a semiconductor layer, doping of the semiconductor occurs due to migration of ions from ion gel into the semiconductor on the application of voltage. We have discussed this behavior in previous chapter. Once the ions start migrating into the semiconductor layer, from the semiconductor and dielectric interface, there is a movement of ions within the semiconductor layer, affecting the local ion concentration and hence the local doping levels. In order to obtain quantitative estimates for the movement of ions into and within the semiconductor it is essential to develop a theoretical model that provides insight into the mechanisms behind the process. We propose a theoretical model to explain the doping of the semiconductor due to drift and diffusion of ions from the ion gel within the semiconductor layer on the application of voltage.

The movement of ions into the polymer layer is governed predominantly by two factors viz.,

1. Movement due to electrostatic attraction experienced by ions due to applied bias voltage, in both x and y directions which can be termed as drift of ions and

2. Motion of ions due to the gradient of their concentration which is diffusion of ions.

Attempts have been made in the past to model a similar phenomenon in case of ion gel gated polymer transistors, albeit by accounting for both these processes with a combined diffusion coefficient [73]. The motivation of the gate voltage dependent ion diffusion modeling by Lee et al is to show at what kind of conditions an ion gel gated transistor can be purely electrostatical (without any ions penetration) or electrochemical (with ion penetration) which is predominantly limited to the transistor regime, in one dimension. While this approach of lumping two effects into one is simple and can satisfactorily explain certain diffusion phenomena, which might be sufficient in deciding the conditions for electrostatic and electrochemical domains it is inadequate to explain the process in more than one dimensions.

Even for one-dimensional models, this approach can only be used to explain measurements which integrate ion concentration over that dimension, essentially disregarding the 1-dimensional variation of the diffused ion concentration. We propose to overcome this limitation by developing the model in two dimensions and investigate the effect of both drift and diffusion of the ions within the semiconductor.

To assess the performance of the theoretical model, in addition to developing it, it is essential to validate it against experimental data. In this work, we develop a two-dimensional computational model to predict the diffusion of $TFSI^-$ ions into F8BT semiconductor layer in a bilayer device and match the results of the model to experimental results at constant applied voltage.

Firstly, we retain the approach of lumping the drift and diffusion in a single diffusion coefficient but extend the model to two dimensions. Later, we develop a model that treats drift and diffusion as independent phenomena. We compare the results of each of these models with experimental results obtained by photoluminescence probing in an F8BT, EMIMTFSI/SOS ion gel bilayer device.

6.2 Diffusion Theory

Diffusion is a process in which a flux of a substance occurs from a location of higher concentration to a location of lower concentration. Fick's first law of diffusion relates the magnitude of flux at a location in space to the concentration gradient at that location through a diffusion coefficient (or diffusivity)[116]. Equation 6.1 provides a mathematical notation of Fick's first law of diffusion.

$$J = -D(\phi, x)\frac{\partial \phi}{\partial x} \tag{6.1}$$

Where J is the flux, D is the diffusion coefficient, ϕ is the concentration and x is a spatial dimension. Fick's second law describes the temporal variation of the concentration with the relation

$$\frac{\partial \phi}{\partial t} = \frac{\partial}{\partial x}\left[D(\phi, x)\frac{\partial \phi}{\partial x}\right] \tag{6.2}$$

Since this is a second order partial differential equation, analytical solutions to this equations might be arrived at using the Green's function approach only under certain special cases. In this work, we hence use a more general numerical method to obtain solutions.

6.2.1 Isotropic Diffusion Coefficient

Diffusion coefficient expressed in equation 6.2 is actually a tensor. In Cartesian coordinates the tensor has nine components D_{xx},D_{xy},D_{xz}....D_{zz}, where D_{ij} is the diffusion coefficient in direction i due to a concentration gradient in direction j. When there is no orthogonal diffusion (i.e., diffusion in direction i due to a concentration gradient in direction j) and when the diffusion coefficients along the concentration gradient are identical in all directions, we call the diffusion coefficient to be isotropic. In other words, for an isotropic diffusion coefficient tensor,

$$D_{ij} = 0 \tag{6.3}$$

$$D_{ii} = f(\phi) \tag{6.4}$$

An isotropic diffusion is a characteristic of several physical phenomena including mass transfer due to diffusion. When the diffusion coefficient is isotropic and constant, the coefficient D can be treated to be independent of the partial derivatives. This makes the equations simpler to solve.

6.3 Numerical Methods

Numerical method refers to the method of obtaining a solutions to equations using numerical and computational techniques as opposed to solving them through analytical process involving only algebraic operations. Although numerical methods can be used to solve equations varying from very simple to very complex, in practice they are employed mostly to solve governing equations behind various physical phenomena. In particular, numerical methods are the method of choice for solving linear and non-linear partial differential equations for conservation of physical quantities. Typical examples include fluid dynamics, electromagnetic radiation, seismic predictions, heat transfer and mass transfer.

When compared to an analytical method, numerical methods offer a more general approach to solving partial differential equations. They also allow the use of modern digital computing power to solve the differential equations and hence make many equations amenable for solution within a reasonable timescale.

However, by their nature, numerical methods offer only an approximate solution to the equations as opposed to an exact solution from an analytical method. Numerical solutions are also affected by numerical artefacts like numerical diffusion, numerical instability etc. These limitations can be minimised to a great extent by careful selection of grid spacing, discretization methods and timesteps.

In spite of their limitations they offer the only reasonable approach to solving many sets of complex non-linear partial differential equations. The convenience and benefits of numerical methods outweigh their disadvantages and for this reason they are very popular in several scientific and engineering fields. In this work we use numerical method to solve the linear partial differential equation governing the diffusion and drift of ions within the semiconductor layer.

6.4 Numerical Model with Lumped Diffusion Coefficient

We first consider a theoretical model with an isotropic lumped diffusion coefficient. This means that the diffusion is uniform in all directions at any given point within the semiconductor as discussed in section 6.2.1. However, the value of diffusivity itself might vary as a function of location.

6.4.1 Governing Equation

For this 2D model, we use Fick's second law (equation 6.2) in two dimensions

$$\frac{\partial \phi}{\partial t} = D(x, y) \left(\frac{\partial^2 \phi}{\partial x^2} + \frac{\partial^2 \phi}{\partial y^2} \right) \tag{6.5}$$

This equation is continuous in both space and time and can hence be discretized in space and time. Moreover, the diffusion equation is linear and separable in spatio-temporal dimensions. Hence it is amenable to a numerical solution using finite differences method. In this work, we use a numerical method to solve the diffusion equation within the semiconductor layer to obtain the time-varying concentrations of $TFSI^-$ ions within the semiconductor.

This equation is a second order equation in space and first order in time and hence requires boundary conditions on all the physical boundaries and an initial condition. These are discussed in section 6.4.3.3.

6.4.2 Assumptions and Approximations

During our attempt to develop a theoretical model and a numerical solution to ion diffusion, we have come across several detailed parameters which are either too complex to be included in the theoretical model we propose or have an insignificant effect on the accuracy of the simulations. We have hence made following assumptions and approximations in order to exclude those parameters from the numerical model.

1. The movement of ions into and within the semiconductor layer is solely due

to diffusion and is hence governed by the diffusion equation.

2. Although diffusivity varies with location, at each location the diffusivity is assumed to be isotropic.

3. Electrode thickness can be neglected and the electrodes can be represented by singular points in a 2D computational domain.

4. Non-linear effects i.e. effect of ion concentration within the semiconductor on the local diffusion coefficient, if any are neglected.

6.4.3 Numerical Model Specification

6.4.3.1 Computational Domain

In this work, we use a rectangular model to approximate a 2D cross section of a bilayer device. The section contains two electrodes with a semiconductor layer between them. An ion gel layer sits on the top of the semiconductor layer. Figure 6.1 shows a schematic representation of the numerical model. The model represents the semiconductor layer approximated in a rectangular domain. X dimension represents the channel width while Y direction represents the thickness of the polymer semiconductor layer. In this study, the model span is 200 microns in X direction and 40 nm in Y direction, in line with the physical device against whose experimental results the numerical results are compared.

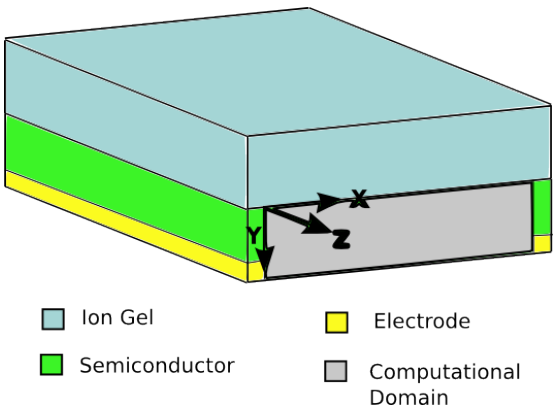

Figure 6.1: Schematic of computational domain and coordinate system

6.4.3.2 Computational Mesh

A numerical solution is calculated on discrete points in the computational domain. The governing equation is discretized over a computational grid of dimensions 101 nodes x 51 nodes in X and Y dimensions respectively. The grid spacing in each direction is constant resulting in an uniform grid with grid spacing in X direction of $2.0 \times 10^{-6} m$ and in Y direction of $8.0 \times 10^{-10} m$. Figure 6.2 shows the schematic of the numerical grid used in this work. At each spatial location, the governing equation is discretized using second order central difference as discussed below.

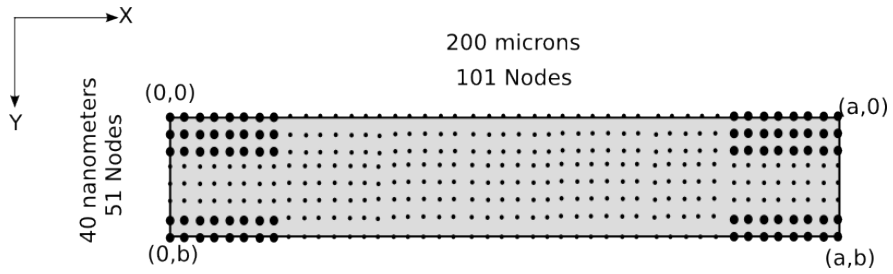

Figure 6.2: Schematic of computational mesh

6.4.3.3 Initial and Boundary Conditions

The governing equation is a second order differential equation. To solve the equation a set of initial conditions and a set of boundary conditions are necessary.

At the beginning of the simulation, (t=0), the semiconductor layer can be assumed to have no diffused ions. i.e. $\phi_{(t=0)} = 0$ We can use this as an initial condition for the simulation.

The top boundary of the numerical model (y=0) represents the interface between ion-gel and semiconductor polymer. Since the ion gel can be assumed to be an inexhaustible source of ions, it implies a constant-concentration boundary condition on this boundary. i.e., $\phi_{(t,y=0)} = constant$

However, there are no precise estimates for the number of ions available for diffusion at the gel-semiconductor interface. We derive an approximation for the value of concentration at this interface using the capacitance value of $1 \mu F/cm^2$ of the bilayer device. The estimated concentration of ions at the interface is $1.0 \times 10^{17} ions/m^2$ (or $1.0 \times 10^{13} ions/cm^2$). However, using this value directly

causes significant numerical instabilities in the numerical code and for stability we are restricted to using extremely small time steps, making the simulation time impractically long. However, since the governing equation is linear, it can be shown that all the solutions to the equation are mathematically self-similar and the value of the boundary condition at the ion-semiconductor interface does not alter the 'shape' of the solutions. We hence normalise the value of this boundary condition nominally as $\phi_{(t,y=0)} = 10^{-10} ions/cm^2$. In addition, we use a normalisation approach described in section 6.10 to enable a comparison to the experimental results, eliminating the significance of precise value for this boundary condition. The only requirement for this boundary condition is that it is a constant.

The bottom boundary represents the interface between polymer semiconductor and the substrate. Since there can not be a flux of ions into the substrate, we can infer a boundary condition at this boundary which implies the gradient of concentration in Y direction is zero. i.e. $\frac{d\phi}{dy}|_{y=b} = 0$

For the left and right boundaries, a similar boundary condition might be used. i.e., $\frac{d\phi}{dx}|_{x=0}$ and $\frac{d\phi}{dx}|_{x=a}$ which implies a symmetry or a periodic boundary condition. The model hence simulates an infinite array of such semiconductor channels in X direction. This approximation is valid since the actual experimental device consisted of several channels in the X direction in the form of an interdigitated pattern.

6.5 Numerical Solution Method

To obtain a numerical solution, we follow the following steps

1. Discretization of the equation in spatial dimensions using second order central difference

2. Time marching using first order forward difference

6.5.1 Discretization

Discretization refers to the process of evaluating a continuous function at several discrete points. Discretization is a key step in a numerical method and the right discretization scheme is necessary to ensure accurate solutions. We discretize the various partial derivatives as :

$$\frac{\partial^2\phi}{\partial x^2} = \frac{\phi(x+\Delta x) - 2\phi(x) + \phi(x-\Delta x)}{\Delta x^2} + O(\Delta x^2) \tag{6.6}$$

$$\frac{\partial^2\phi}{\partial y^2} = \frac{\phi(y+\Delta y) - 2\phi(y) + \phi(y-\Delta y)}{\Delta y^2} + O(\Delta y^2) \tag{6.7}$$

Where $O(\Delta x^2)$ and $O(\Delta x^2)$ indicate the errors due to second order approximation of the derivative. These represent the central difference approximation of the derivatives with an error term of the order of the square of grid spacing. Applied to the numerical grid, these can be written as

$$\frac{\partial^2\phi}{\partial x^2} = \frac{\phi^t_{(i+1,j)} - 2\phi^t_{(i,j)} + \phi^t_{(i-1,j)}}{\Delta x^2} + O(\Delta x^2) \tag{6.8}$$

$$\frac{\partial^2\phi}{\partial y^2} = \frac{\phi^t_{(i,j+1)} - 2\phi^t_{(i,j)} + \phi^t_{(i,j-1)}}{\Delta y^2} + O(\Delta y^2) \tag{6.9}$$

where i,j are the x and y indices for the grid point and Δx and Δy are the distances between grid cells in x and y directions respectively. In this simulation, we have used a grid spacing of $\Delta x = 2.0 \times 10^{-6}$ and $\Delta y = 8.0 \times 10^{-8}$.

For the boundary cells where these central differences are undefined, we use the boundary conditions discussed above to arrive at the local concentrations. Boundary conditions are discretized using first order forward or backward differences.

6.5.2 Time-marching

A first order forward difference is employed for time marching. The time derivative can be discretized using first order forward difference as

$$\frac{\partial \phi}{\partial t} = \frac{\phi^{t+1} - \phi^t}{\Delta t} \tag{6.10}$$

where Δt is the time increment between consecutive time steps. In this simulation, we use explicit time marching scheme and hence for numerical stability, we use a small time-step of 10^{-3} second.

Combining the spatial and temporal discretization described in equations 6.8, 6.9 and 6.10, we can re-write the governing equation (Equation 6.5) as

$$\begin{aligned}\frac{\phi^{t+1}_{(i,j)} - \phi^t_{(i,j)}}{\Delta t} = D \Bigg[& \frac{\phi^t_{(i+1,j)} - 2\phi^t_{(i,j)} + \phi^t_{(i-1,j)}}{\Delta x^2} + O(\Delta x^2) \\ & + \frac{\phi^t_{(i,j+1)} - 2\phi^t_{(i,j)} + \phi^t_{(i,j-1)}}{\Delta y^2} + O(\Delta y^2) \Bigg]\end{aligned} \tag{6.11}$$

Or ignoring the higher order error terms,

$$\frac{\phi^{t+1}_{(i,j)} - \phi^t_{(i,j)}}{\Delta t} = D \left[\frac{\phi^t_{(i+1,j)} - 2\phi^t_{(i,j)} + \phi^t_{(i-1,j)}}{\Delta x^2} + \frac{\phi^t_{(i,j+1)} - 2\phi^t_{(i,j)} + \phi^t_{(i,j-1)}}{\Delta y^2} \right] \tag{6.12}$$

Rearranging,

$$\phi^{t+1}_{(i,j)} = \phi^t_{(i,j)} + D\Delta t \left[\frac{\phi^t_{(i+1,j)} - 2\phi^t_{(i,j)} + \phi^t_{(i-1,j)}}{\Delta x^2} + \frac{\phi^t_{(i,j+1)} - 2\phi^t_{(i,j)} + \phi^t_{(i,j-1)}}{\Delta y^2} \right] \tag{6.13}$$

We employ this discretized governing equation in a computer program and iterate through time steps until desired time duration is simulated.

6.6 Variation of Diffusivity

Since diffusivity coefficient includes the effect of diffusion due to the electrostatic field experienced by the ions within the polymer layer, it can be treated as a func-

tion of local electrostatic potential[73]. We use the numerical model to asses the effect of various profiles (linear, quadratic, cubic, exponential etc.) and identify the distribution that best matches experimental data. Since we assume diffusion coefficient to be a variable across the length of the device, when we specify a diffusivity value in this work, it is nominally specified at the location with highest electrostatic potential.

Initial estimate for the value of diffusivity coefficient was based on the reported value of $10^{-12} cm^2/s$ by Lee et.al.[73]. However, the value of diffusivity constant and its distribution profile were iterated and fine tuned to obtain the best fit with experimental data. The final values are discussed in detail in the results and discussion section 6.11

6.7 Implementation of the Numerical Method

The numerical method discussed above is implemented using a computer program written using C programming language. The program was compiled using a standard GCC compiler and linked using standard C libraries. The simulations were performed on a standard computer with double precision accuracy. The simulation was run for a total simulation time of 451 seconds using a time step of $1.0 \times 10^{-3} s$ and output was written into files at an interval of $1s$. A program listing written in C is provided in appendix 7.2 which implements both lumped model as well as independent drift and diffusivity model. Comments within the listing explain how the code can be easily modified to run either of the models.

6.8 Interpretation of Experimental Data

In order to make an appropriate comparison, we first select the experiments that best match the modeling scenario employed. Fluorescence probing of an operating bilayer device (channel length of 200 μm and polymer thickness of 40 nm) at a constant 3.5V voltage application at different intervals of time is compared with the model. Fluorescence probing images at different intervals of time representing different levels in photoluminescence quenching and hence different ion concentration in the polymer slab are considered. Since the results

from photoluminescence experiment represent the extent of photoluminescence quenching due to the presence of diffused ions in the semiconductor layer, a careful interpretation of experimental data is necessary to compare it against the numerical results. To facilitate the comparison, we follow these steps:

- Selection of location for comparing the experimental results to numerical results
- Correlating photoluminescence brightness to extent of ion diffusion
- Calibration of photoluminescence brightness values
- Normalisation of experimental and numerical results

6.8.1 Selection of Location

Figure 6.1 shows the 3D schematic of the experimental device along with the coordinate system conventions used in this work. Photoluminescence experiments provide images in X-Z dimension where the brightness value can be assumed to be correlated with the integrated ion concentration in Y direction at each X-Z point. Since we propose a 2D numerical model in X-Y plane eliminating Z dimension, we choose a line along X direction to compare the experimental results to the numerical results.

Since we have neglected the variation in Z direction, we should select a region with negligible variation in the Z direction so that 2D approximation is valid. We hence select a region where the end-effects are minimal and the 2D approximation is valid in X-Y plane. Figure 6.3 shows the line along X direction on which the brightness values are extracted.

Figure 6.4 shows the raw values of brightness along the selected X location across a device.

6.8.2 Correlating Brightness to Diffusion

Variation in the brightness is a direct consequence of photoluminescence quenching within the polymer due to the presence of diffused ions from the ion gel. An increased diffused ion concentration results in reduced photoluminescence. Hence,

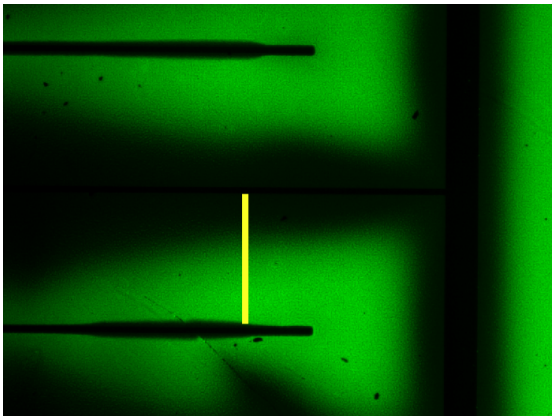

Figure 6.3: Location at which experimental data is selected. The yellow line represents the line along X axis on which the experimental data is measured and compared against numerical results

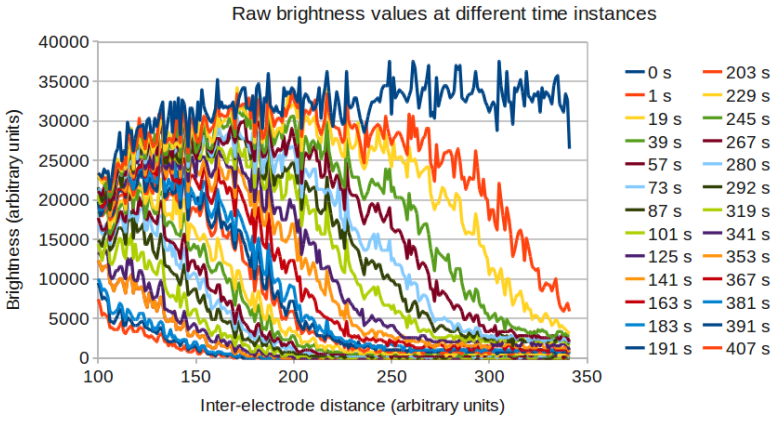

Figure 6.4: Raw experimental data obtained from analyzing the pixels brightness of the pictures from fluorescence probing of the bilayer devices under operation.

we can conclude that the brightness is inversely proportional to the diffused ion concentration. In order to enable comparison with numerical results, we negate the brightness values to obtain the profile for diffused ion concentration along X direction.

6.8.3 Calibration of Brightness

As seen in Figure 6.4, the experimental data contains significant levels of noise due to the limitations of the photo sensor and data extraction. To minimize the effect of noise, we smooth the data with a 10-point moving average at each time step. Figure 6.5 shows the smoothed data.

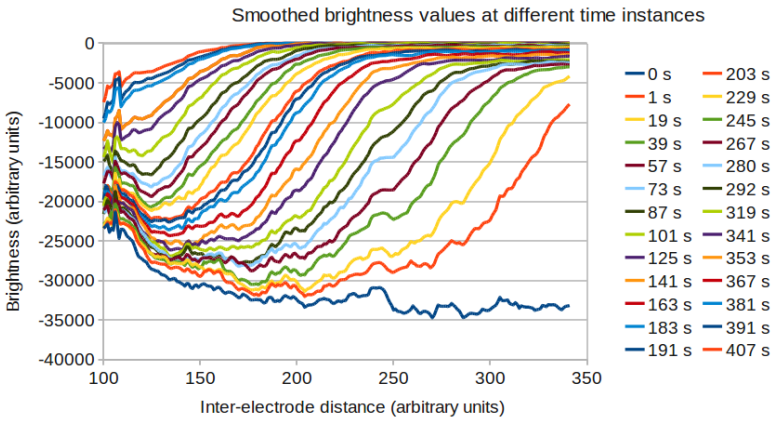

Figure 6.5: Smoothed(10-point moving average) negated data of the raw data shown in figure 6.4.

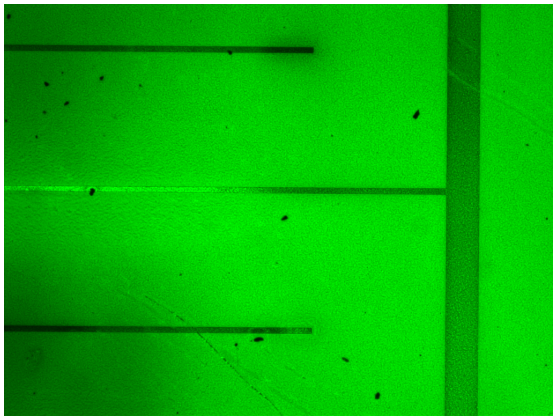

Figure 6.6: Pristine semiconductor before application of voltage. The channel length is 200 μm.

Figure 6.6 shows photoluminescence image of semiconductor in pristine state

before any voltage is applied and ions have started to diffuse. However, we can see a gradient in the brightness of the semiconductor across the device due to the change in surface(metal electrodes), due to variation in the incident angle of UV light as well as the variation in apparent angle on the photographic sensor. This variation can hence be treated as an artifact resulting from the limitations in the experimental setup and can be assumed to be constant across all the time steps.

To compensate for this artefact and to calibrate the actual brightness, at every time step we subtract from apparent brightness the brightness values from the pristine state of the polymer. This ensures that the final value of the brightness can be correlated with the extent of diffusion in the polymer layer. We also note that this calibration is performed on the smoothed data shown in figure 6.5.

Figure 6.7 shows the calibrated data at the selected location.

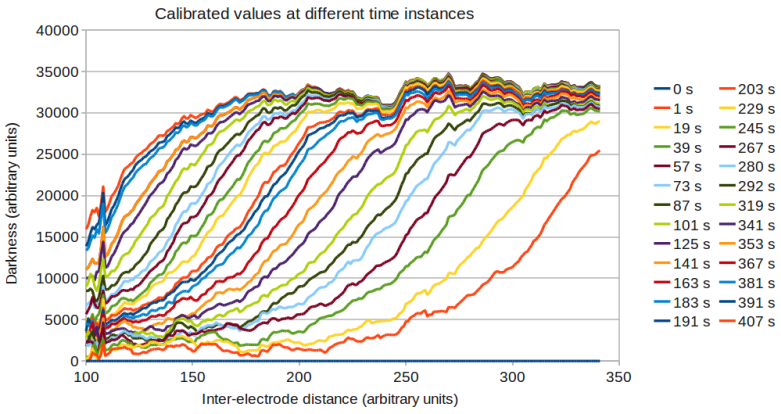

Figure 6.7: Calibrated experimental data

6.9 Interpretation of Numerical Results

Numerical simulations provide the value of ion concentration at each point on the grid on the XY plane. However, as discussed earlier, the experimental results only

provide the value of total amount of diffused ions in Y direction at every point on XZ plane. In order to make a suitable comparison, we must first interpret the numerical results in a similar way.

In order to obtain the total amount of diffused ions, one can integrate the ion concentration profile along Y direction. At every X location, we integrate the concentration profile in the Y direction to obtain the corresponding value for total amount of diffused ions at that X location. We employ numerical integration in the form

$$\int_0^b \phi(x)dy = \sum_{j=1}^{j=ny} \phi(i,j)\Delta y \tag{6.14}$$

The integrated values at each X location then correspond to the experimental results at respective X location.

6.10 Normalisation

There are two obstacles to allow a direct comparison of numerical results to experimental data. Firstly, there is uncertainty over the absolute values obtained from the numerical model since there is uncertainty over the number of available ions at the gel and polymer semiconductor interface. Secondly, although the PL quenching in the experiments is directly proportional to the number of diffused $TFSI^-$ ions, there is no certainty over the constant governing that proportionality.

If a reliable estimate for the concentration of available ions at gel and polymer semiconductor interface were to be available, and the proportionality constant between PL quenching and ion concentration were known, it is possible to compare the results of the numerical model to the experimental results directly.

However, since there are no reliable estimates for either of the quantities, we can compare the results only through a normalization process. Moreover, as discussed in section 6.4.3.3, since diffusion equation (in the form considered here) is not non-linear, the concentration value applied at the top boundary has no bearing on the 'shape' of the diffusion profile. It is hence possible to normalize all the results with respect to an arbitrary value (in this case, the maximum value

within the dataset) and compare different numerical and experimental results. When normalized using the highest value within the dataset, the profiles will always vary between 0 and 1.

6.11 Results From Lumped Diffusivity Coefficient Model

In order to analyze and compare the results, we consider six separate time steps. Figure 6.8 shows contours of doping concentration across the domain at various time instance. We observe that the profile of concentration of diffused ions is in line with the expected profile from a pure diffusion governed process.

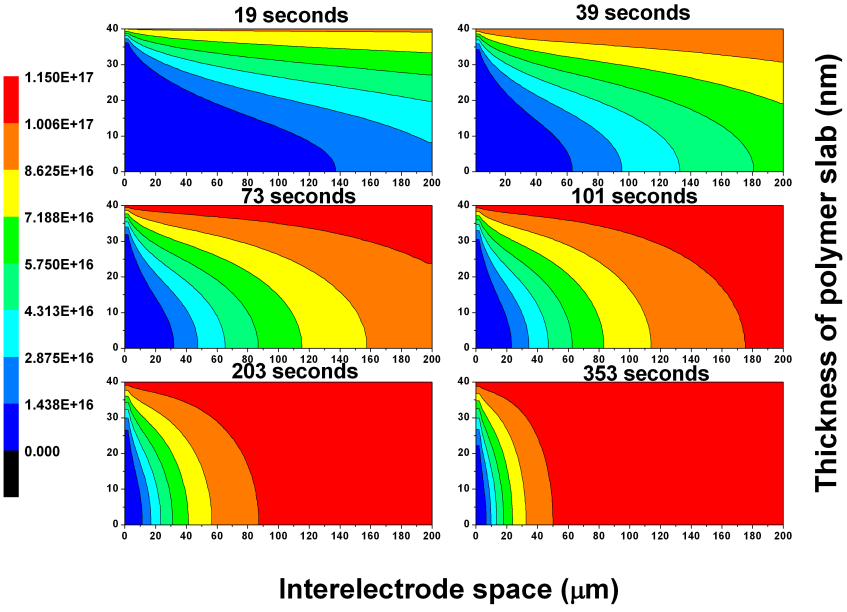

Figure 6.8: Contours of concentration with lumped diffusion coefficient model which assumes a linear variation of the diffusivity between the electrodes.

To compare these results with experimental results, we integrate the concentration values along Y direction at each X location. At each time step we compare the diffused ion concentration at each X location as measured from experiments

and as predicted from the model. We will then analyze these comparisons and make suitable observations.

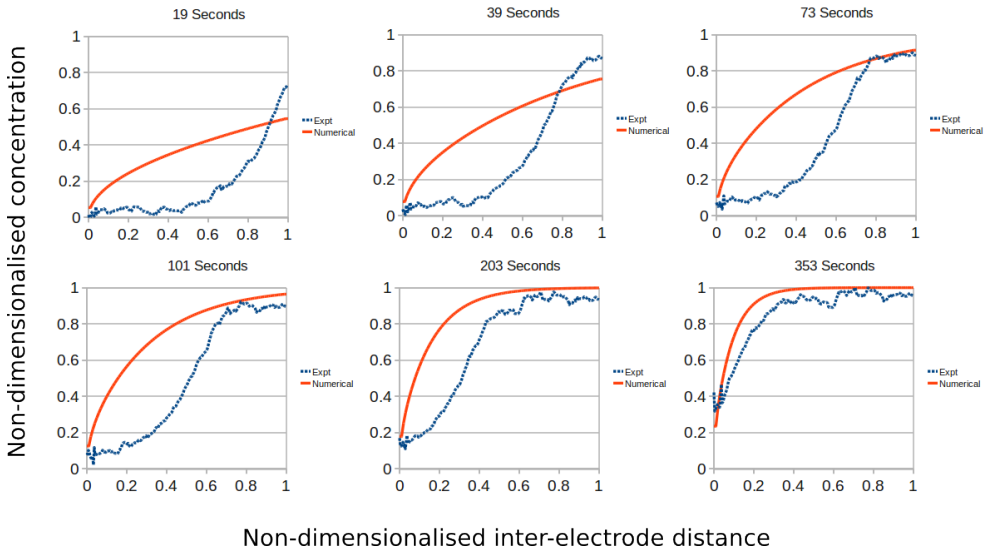

Figure 6.9: Results from lumped diffusivity coefficient model comparing the numerical data(red line) obtained with experimental data (blue line).

Figure 6.9 shows the comparison of experimental and computational concentration profile along the length of the device at various time steps. It can be seen that during the initial time instances (e.g. t=19 seconds) there is a strong mismatch between the experimental results and numerical results both in the shape of the variation as well as the peak values. During later phases however, both these errors start to reduce and the maximum values from the numerical result start to match the experimental results. However, the discrepancy in the trend continues till the end and is not satisfactory.

We tune the value of this lumped coefficient as well as its variation profile along the distance between electrodes, to best fit the experimental data. We get the best match with experimental results when the diffusivity is assumed to vary linearly between electrodes with a maximum value (at the right boundary) of $2.0 \times 10^{-11} cm^2/s$ (at a potential difference of 3.5 V between electrodes). This is in line with the reported value of lumped diffusivity coefficient in the order of $10^{-12} cm^2/s$ [73].

However, even with the best value for the lumped diffusion coefficient there

is a strong discrepancy between numerical and experimental results. We hence hypothesize that this discrepancy arises due to the assumption of lumping the diffusion and drift effects into a single diffusion coefficient. Diffusion coefficient is related to the second derivative of concentration gradient as discussed above whereas the drift coefficient is dependant on the gradient of the electric potential filed. The approach of lumping these two dissimilar physical quantities is hence not justifiable.

We hence develop a model that treats the diffusion and drift as independent phenomena. We discuss this model in section 6.12

6.12 Numerical Model with Independent Drift and Diffusion Coefficients

To address the limitations due to the lumping of drift and diffusion coefficients together, we develop a numerical model which accounts for separate drift and diffusion coefficients. A diffusion equation with drift term is used to describe physical phenomena like brownian motion and other similar mixing and mass transfer processes. Based on their particular form, they are called by various names including Fokker-Planck equation, Kolmogorov backward equation and Smoluchowski equation. For this work, we consider the governing equation in their generic form:

$$\frac{\partial \phi}{\partial t} = -\frac{\partial}{\partial x}\left[\lambda \phi\right] + \frac{\partial}{\partial x}\left[D\frac{\partial \phi}{\partial x}\right] \tag{6.15}$$

where λ is the drift velocity. However, in our case, the drift velocity can be determined by the mobility μ and the electrostatic field E using the relation

$$\lambda = \mu E \tag{6.16}$$

Further, we can express the electric field E as a gradient of the electric potential field V i.e.,

$$E = -\bigtriangledown V \tag{6.17}$$

Hence, equation 6.15 can be re-written as

$$\frac{\partial \phi}{\partial t} = -\frac{\partial}{\partial x}\left[-\mu\phi \bigtriangledown V\right] + \frac{\partial}{\partial x}\left[D\frac{\partial \phi}{\partial x}\right] \tag{6.18}$$

Or, in two dimensions,

$$\frac{\partial \phi}{\partial t} = -\frac{\partial}{\partial x}\left[-\mu\phi \bigtriangledown V\right] + \frac{\partial}{\partial y}\left[-\mu\phi \bigtriangledown V\right] + \frac{\partial}{\partial x}\left[D\frac{\partial \phi}{\partial x}\right] + \frac{\partial}{\partial y}\left[D\frac{\partial \phi}{\partial y}\right] \tag{6.19}$$

Since the diffusion coefficient for a given combinations of materials is constant and mobility of a given ion in a given semiconductor is a constat, we can simplify the equation as

$$\frac{\partial \phi}{\partial t} = \mu\left[\frac{\partial}{\partial x}\left[\phi \bigtriangledown V\right] + \frac{\partial}{\partial y}\left[\phi \bigtriangledown V\right]\right] + D\left[\frac{\partial^2 \phi}{\partial x^2} + \frac{\partial^2 \phi}{\partial y^2}\right] \tag{6.20}$$

Expanding the gradient notation with due regard to its vector components, we obtain

$$\frac{\partial \phi}{\partial t} = \mu\left[\frac{\partial V}{\partial x}\frac{\partial \phi}{\partial x} + \phi\frac{\partial^2 V}{\partial x^2} + \frac{\partial V}{\partial y}\frac{\partial \phi}{\partial y} + \phi\frac{\partial^2 V}{\partial y^2}\right] + D\left[\frac{\partial^2 \phi}{\partial x^2} + \frac{\partial^2 \phi}{\partial y^2}\right] \tag{6.21}$$

We use this equation as the governing equation for the model. We use a discretization approach as earlier and use a first order finite difference approximation for all first derivatives and second order finite difference approximation for all the second derivatives. We can hence write the time marching equation applied to the computational mesh as

$$\begin{aligned}\phi^{t+1}_{(i,j)} = \phi^{t}_{(i,j)} + \Delta t\Bigg[\mu\Bigg\{&\frac{V^t_{(i+1,j)} - V^t_{(i,j)}}{\Delta x}\frac{\phi^t_{(i+1,j)} - \phi^t_{(i,j)}}{\Delta x} + \phi\frac{V^t_{(i+1,j)} - 2V^t_{(i,j)} + V^t_{(i-1,j)}}{\Delta x^2} + \\ &\frac{V^t_{(i,j+1)} - V^t_{(i,j)}}{\Delta y}\frac{\phi^t_{(i,j+1)} - \phi^t_{(i,j)}}{\Delta y} + \phi\frac{V^t_{(i,j+1)} - 2V^t_{(i,j)} + V^t_{(i,j-1)}}{\Delta y^2}\Bigg\} + \\ &D\left\{\frac{\phi^t_{(i+1,j)} - 2\phi^t_{(i,j)} + \phi^t_{(i-1,j)}}{\Delta x^2} + \frac{\phi^t_{(i,j+1)} - 2\phi^t_{(i,j)} + \phi^t_{(i,j-1)}}{\Delta y^2}\right\}\Bigg]\end{aligned} \tag{6.22}$$

We use this discretized time marching equation for solving the governing equation with initial and boundary conditions as described in section 6.4.3.3

6.12.1 Voltage variation

The governing equation above requires a voltage field to be imposed on the computational domain to allow for the calculation of the ion concentrations. The voltage field itself is a function of ion concentration since it is determined by the extent of doping caused by the ions in the semiconductor. Hence, the problem becomes non-linear. An accurate solution accounting for the non-linearity involves solving for ion concentration, hole concentrations in the semiconductor and using the charge distribution to obtain potential field using the Poisson's equation. Further the extent of doping varies with time, making the solution highly complicated. For this work, we have instead taken a simpler approach of including the non-linear effects by a simplified voltage variation approximation. We have based this approach on the following assumptions:

- When a semiconductor heavily doped to the level of interface ionic concentration, the conductivity is assumed to be high and we can neglect the potential drop across the heavily doped region. Numerically, a cut of value of 0.99975 of the interface ion concentration is used to determine a heavily doped semiconductor regime.
- When a semiconductor zone is partially doped, i.e. before the ion concentration in polymer film reaches the value of the ion concentration at the interface, the potential drop across the whole partially doped semiconductor region varies as the square of the distance from the ground electrode. This approximation is done based on the profile that best matches with our experimental results.
- voltage profile calculated at each time step using these assumptions can be used in turn to calculate the ion concentrations.

No potential drop accross the doped region and the quadratic variation of the voltage profile within the undoped semiconductor region matches the experimental profile best. Moreover, the quadratic profile assumed above has a very good

qualitative match with experimental results viz, the scanning kelvin probe microscopy studies on an operating device, presented by Matyba et al[86] of a planar light emitting electrochemical cells.

6.12.2 Assumptions and Approximations

Similar to lumped diffusion coefficient model, we use several assumptions and approximations in the case of numerical model with independent drift and diffusivity coefficients. Below is a list of assumptions and approximations.

1. The movement of ions into and within the semiconductor layer is solely by the diffusion and drift processes alone and hence governed by the governing equation 6.22.

2. Diffusion coefficient and mobility are not dependant on electric potential and hence constants within the semiconductor layer.

3. Electrode thickness can be neglected and the electrodes can be represented by singular points in 2D.

4. Diffusion of $EMIM^+$ ions from the gel into the semiconductor can be neglected and has no effect on the concentration of $TFSI^-$ ions.

6.13 Results and Discussions

As before, we compare the experimental results with model predictions at various time instances. Figure 6.10 shows the contours of concentration at various time instances within the computational domain. We observe that the distribution of ions obtained from this model is different from that obtained by the lumped diffusion coefficient model.

We make a comparison with experimental results using the integrated ion concentration along Y direction at each X location. Figure 6.11 shows concentration profile versus distance from numerical and experimental results. In general, we observe that there is a good qualitative match between the experimental results and model predictions. At the right extreme of the model, the diffusion and

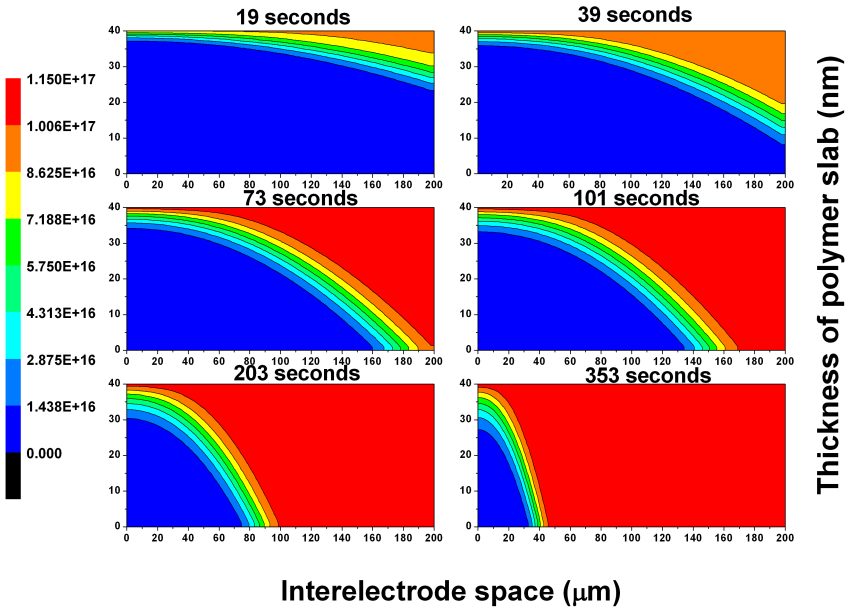

Figure 6.10: Contours of ion concentration from numerical model with independent drift and diffusion coefficients

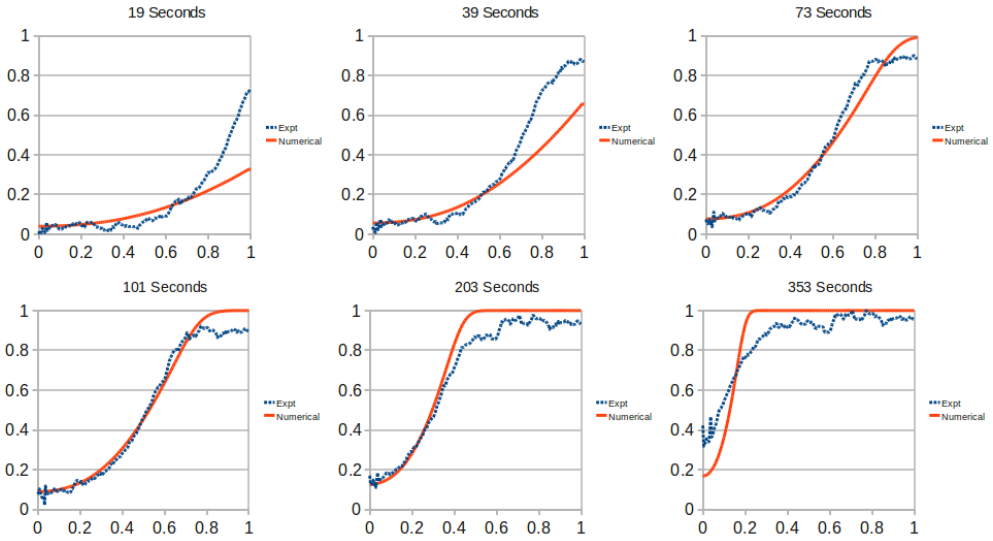

Figure 6.11: Results from model (red line) with drift coefficient differing from the previous lumped diffusion model in comparison with experimental data (blue line).

drift are very high as could be expected from the high local potential favoring the movement of $TFSI^-$ ions into the semiconductor. Conversely, at the left extreme of the domain, the extent of diffusion is very low. The profile of the distribution as predicted by the numerical model agrees well with the experimental results.

Quantitatively, we observe that during initial time steps, there is a mismatch between the predicted and experimental results towards in the right hand part of the computational domain. This indicates that there is a non-linear doping effect occurring in the initial few seconds of the simulation that has not been taken into account in the numerical model. During intermediate time intervals, there is a very good match between the experimental and numerical results. This indicates that the initial non-linear effects have become less significant and the ion movement is mostly governed by the drift and diffusion as accounted for by the theoretical model. During the final time steps, we see that the theoretical model under-predicts the ion concentration in the viscinity of the left electrode. This can be explained partially by the end effects occurring due to a formation of a strong p-n junction near the left electrode and by the fact that the numerical model does not account for diffused $EMIM$ ions. Presence of $EMIM$ ions also induces photoluminescence quenching near the left electrode and since we have not modeled the movement of $EMIM$ ions, the model fails to predict their presence, resulting in an overall under-prediction of doping levels near the left electrode.

Using this model, we have experimented with various values for diffusivity and drift coefficients. We find that a diffusion coefficient of $1.0 \times 10^{-15} cm^2/s$ and a drift coefficient of $1.0 \times 10^{-13} cm^2/Vs$ fits very well with fluorescence quenching of the polymer film with time at a fixed voltage.

The relationship between these values can also be independently verified using Einstein equation

$$D = \frac{\mu k_B T}{e} \tag{6.23}$$

where k_B is the Boltzman's constant, T is the temperature and e is the elementary charge. The obtained values from the numerical model independently are in line with this relationship.

With our numerical model, we show that the drift motion of ions contributes

significantly in quenching the photoluminescence of the active polymer layer, compared to the diffusion of ions. This is consistent with the fact that we do not see photoluminescence quenching of the active polymer layer in bilayer devices for many hours if the device has not been applied any voltage. However, on the application of voltage PL quenching of the polymer (refer section 5.2.4) in a 200 μm channel device happens on the time scale of seconds (400 s). In this model drift and diffusion effects are well decoupled as opposed to a lumped model.

For comparison, the values for diffusion coefficient reported by Lee et al.[73] is of the order of $10^{-12} cm^2/s$ in case of $TFSI^-$ ions in P3HT polymer and the values reported by Mills et al.,[88] in case of $ClO4^-$ ions in P3HT is of the order of $1.3 \times 10^{-14} cm^2/s$. We however note that these values were based on a 1 dimensional model and drift and diffusion effects were lumped in these theoretical models.

However, the numerical results exhibit one distinct deviation from the experimental results. There is a difference at the value of saturation of the concentration between numerical and experimental results. While the numerical model predicts a saturation at a constant value at all time steps, the experimental values of saturated ion concentration increase slowly with time (in spite of being normalized with constant normalization factor).

This discrepancy can be attributed to the boundary condition at the gel-semiconductor interface. We have made an assumption that the ion gel is an infinite source of ions and hence the concentration of available ions at the interface is always constant. However, in reality, the availability of ions at the gel-semiconductor interface is determined by the finite ion current across the interface. The effect of the finite current is hence to increase with time the concentration of ions available at the interface for diffusion and drift.

To account for this temporal variation of ion concentration at the interface, we use a time varying boundary condition at the interface and re-run the numerical model. We have found that, from the starting value of the concentration, a 10% linear increase through the simulation time (450 seconds) provides an acceptable match with the experimental results.

Figure 6.12 shows the results obtained by a varying boundary condition. We observe that by applying a time-varying boundary condition, we can eliminate

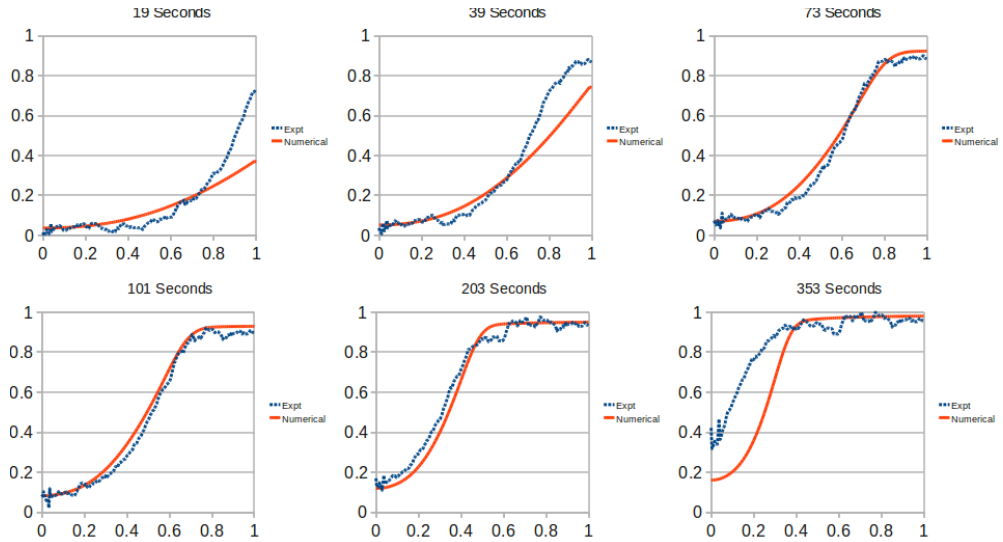

Figure 6.12: Results comparing the numerical data(red line) obtained with temporally varying boundary conditions with experimental data (blue line).

the first discrepancy to a good extent. The differences between experimental and numerical results can be attributed to the factors such as the non-linear variation in diffusion and drift coefficients due to presence of previously diffused ions and spatial distribution of charge carriers, approximations in the numerical model that are not consistent with experimental device, for example, electrodes on the experimental device have a finite dimension and also ignoring of 3D effects in a 2D numerical model, although we have selected the experimental results at a location with minimal variation along the ignored Z dimension.

6.14 Conclusion

In this work, we have shown that lumping the diffusion and drift coefficients together into one coefficient is not a valid approximation. Further, we have developed a theoretical model for the movement of ions within the semiconductor layer governed by both diffusion and drift independently. We have developed a 2D numerical model based on the theoretical model and have compared the results of the numerical model with the results of a fluorescence probing of the bilayer device with time, at constant potential.

Based on the predictions of numerical model and the comparison of the results to experimental data, we make the following conclusions.

- Migration of the ions within the semiconductor layer is governed by both diffusion and drift effects.
- Lumping the diffusion and drift effects into a single diffusion coefficient does not satisfactorily explain the experimental results.
- In case of $TFSI^-$ ions diffusing in a F8BT semiconductor layer, the values of diffusion coefficient and drift coefficient that best match experimental results are $1.0 \times 10^{-15} cm^2/s$ and $1.0 \times 10^{-13} cm^2/Vs$ respectively.
- Relation between the above values of diffusion and drift (mobility) coefficients can also be independently verified using Einstien Diffusion equation, further validating the numerical model.
- A quadratic variation of voltage profile in the partially doped region of the semiconductor and no potential drop across the doped region provides the best match with the experimental results.
- Moreover, by introducing temporal increment of 10% in the concentration of available ions at the semiconductor-dielectric interface, during the course of 450 seconds, we have shown that the predictions of the numerical model can be further improved. This implies a finite ion current across the interface.

The model developed in this work can be used to asses the diffusion of various combinations of ion gels and polymer semiconductors.

Chapter 7

Conclusions and outlook

7.1 Conclusions

In this work, the light emission in ion gel gated polymer transistors has been reported for the first time and shown that the light emission mechanism in ion gel gated polymer semiconductor transistor is more akin to the mechanism behind the light emitting electrochemical cells.

Firstly, we have studied ion gel gated field effect transistors and report light emission in them when the drain-source voltage V_{ds} exceeds the energy gap of the semiconductor divided by elementary charge. The turn on voltage for light emission is very low compared to other devices with traditional gate dielectric materials. We have also demonstrated that the devices exhibit characteristics of a typical organic field effect transistor when the drain-source voltage is below the corresponding energy gap of the semiconductor and once that threshold is exceeded, light emission occurs. We have shown that the in the light emission regime, both photocurrent due to the electroluminescence and drain current are very well correlated and varies with voltage, as $(V_{ds} - V_{onset})^4$ where V_{onset} is the onset corresponding to the beginning of the light emission or shooting of the current respectively. Using the CMS study, we have shown that the gate voltage dependent ion penetration into the active polymer layer occurs, which makes these devices more akin to a light emitting electrochemical cell.

We also report that the light emission intensity corresponds to the drain cur-

rent and can be modulated with the gate voltage. The ability to modulate the photocurrent however comes at the cost of a reduced EQE. We have shown that the EQE of these devices reduces exponentially with applied gate voltages. Although the gate voltages initially well modulate the transistor behavior, the gate voltage also accelerates the movement of ions into the semiconductor layer, increasing the conductivity of the semiconductor. Eventually, the semiconductor exhibits ohmic characteristics. Hence the highest EQE exhibited by these devices is in the absence of an applied gate voltage. Nonetheless, the effect of the gate voltage corresponding to increasing ion concentration clearly reduces the onset voltages.

In the absence of an applied gate voltage, the devices become planar bilayer LECs, which we have further studied in this work. We report light emission at room temperature in F8BT devices with EMIM-TFSI/SOS ion gel layer on the top of the semiconductor. The devices exhibit light emission characteristics in which the photo current corresponds to the drain current similar to the light emission in the light emission regime of the ion gel gated transistors as described above.

We have demonstrated that when a constant bias is applied, the intensity of luminescence from the devices initially ramps up for about 15 minutes and reaches a steady state. The steady state light intensity remains for about further 90 minutes and then the light intensity diminished gradually. The devices continue to emit light at least till 190 minutes from the start, albeit at the intensity falls down during the later period.

Using fluorescence probing of the device under the constant bias and comparing the same with electroluminescence of the device, we have demonstrated that the doping of the semiconductor due to the presence of ions leads to the formation of a p-n junction eventually and that is the cause behind the light emission in these devices. The photoluminescence experiments also indicate a high diffusivity for $TFSI^-$ ions compared to $EMIM^+$ ions, resulting in a large p-doped area and a very small n-doped area within the semiconductor layer.

We have shown that the light emission due to recombination of holes and electrons occurs in the close proximity of the electron injecting electrode which is consistent with the fact of less diffusion of EMIM ions assisting the electron

injection and transportation and also with the fact that these devices are electron transportation limited (obtained from transistor results in electron accumulation). This indeed results in the absorption of photons from the metal electrode injecting electrons, reducing the EQE. To overcome this and move the light emission zone further away from the metal electrode in order to optimize the device, we have developed devices with transparent ZnO electrodes extending beyond the metal electrodes. We report an improved EQE with ZnO electrode devices.

We also report an improved EQE when a different positive ion is used in the form of BMPY/TFSI ion gel. This slightly moves the recombination zone away from the electron injecting electrode for about $\approx 1\mu m$. When a ZnO electrode is used in combination with BMPY/TFSI ion gel, although there is a significant increase in the photo current, owing to a corresponding high increase in the drain current there has not been any improvement in the EQE. However, the gradual developing up of the electroluminescence and steadying of current in these polymer-gel bilayer devices makes it quite tricky to conclude this, until we do a careful study of EQE with time.

We have also observed light emission with polymers such as F8T2, F8TBT and OC1OC10 indicating a wide range of polymer semiconductors that can be used in combination with these ion gels in a planar bilayer configuration at room temperature, as light emitting devices.

We have developed a theoretical model for the movement of ions within the semiconductor layer based on the drift and diffusion of the ions. We implement the theoretical model into a numerical model and compare the results from the numerical model with the results from the photoluminescence quenching experiments on the F8BT EMIM/TFSI bilayer devices.

We first demonstrate that a theoretical model with a lumped diffusion coefficient to account for both drift and diffusion is insufficient to satisfactorily explain the movement of ions within the semiconductor layer. We further show that independent treatment of drift and diffusion effects suitably explain the ion concentration variation within the semiconductor with time.

Using the numerical model and comparing the results to the fluorescence probing experiments, for TFSI ions moving in F8BT, we obtain a drift coefficient (mobility) of $1.0 \times 10^{-13} cm^2/Vs$ and a diffusion coefficient of $1.0 \times 10^{-15} cm^2/s$.

We show that drift motion of ions is significant in quenching the photoluminescence of the active polymer layer, compared to the diffusion of ions. Moreover, we conclude that in the fully doped semiconductor region, there is a negligible voltage drop. Most of the potential drop occurs in the region of partial doping and the magnitude of the potential drop varies as a square of the distance to the electron injecting electrode.

7.2 Outlook

Bilayer light emitting LECs offer significant application potential with their low turn on and operating voltages. Combined with their favorable electrical characteristics, their physical properties like transparency and flexibility favor their application in large area display devices. While, we know that the prototype of the ion gel, polymer semiconductor planar bilyaer devices work at room temperature, an improvement in the external quantum efficiency of these devices is necessary.

Based on the observations and conclusions of this study, there appear to be two distinct approaches to improving the EQE of these devices, one in which polymers with comparable hole and electron mobilities are employed and the other in which an ion gel with comparable diffusivity/mobility of both anions and cations within the semiconductor are used. Since the devices used in this study are electron mobility limited, improving the electron mobility will aid in moving the recombination zone away from the metal electrodes, leading to EQE improvement. Similarly, a comparable diffusion of both anions and cations into the semiconductor will lead to comparable size of p and n doped areas in the semiconductor, resulting the recombination zone in the middle of the inter electrode space. Another key criteria is to limit the ion diffusion into the polymer layer such as that is employed by the frozen junction LECs)[21] or also by using the third terminal (similar to ion gel gated transistor) to limit the ion diffusion suitably, or these two approches together in order to get the desired p-n junction with minimum amount of ions required in the polymer layer to do so. For example, fixing the gate voltage at 3.5 V and fixing the drain voltage at 3.5 V with source grounded would allow only $EMIM^+$ ions penetraion into the polymer

layer. Keeping in mind that the diffusivity of the $EMIM^+$ ions is very slow, if such an arrangement is set for a suitable period of time, that would eventually get the recombination zone away from the electron injecting electrode.

The numerical model developed in this work can also provide a foundation for extending it into 3 dimensions and for application of the model to arbitrary device configurations. The model, in its current or further developed state, can be used to estimate the diffusivity and drift coefficients of various ions in various semiconductors. The model can further be extend to include intrinsic voltage profile calculations by solving the Poisson's equation for charges and ions, which would unfold the potential distribution profile in these devices. The nature of potential variation in LECs is a source of great debate and the numerical model in combination with experiments such as direct measurement of the potential profile by scanning kelvin microscopy for example, can be an extremely valuable tool to investigate the field distribution.

Appendix: Electron Transportaion in Gel Gated Transistors

This section lists certain facts related to the electron transportation in polymer semiconductor-ion gel gated transistors.

Interestingly, though we do not see electron transportation with F8BT polymer either with EMIM-TFSI/SOS or BMPY-TFSI/SPMMAS ion gels, we do see the electron transportation with F8TBT with BMPY-TFSI/SPMMAS which is however is very small when compared to hole transportation. Figure 1 shows the output characteristics of a transistor in electron accumulation regime.

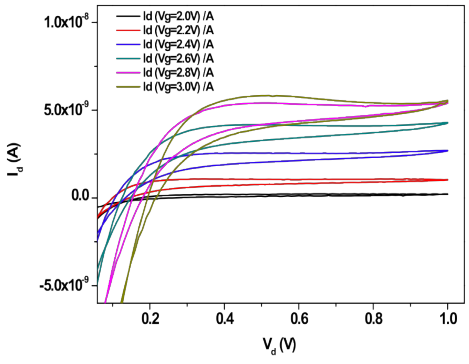

Figure 1: Output characteristics showing the electron transportation of a transistor with channel length, L =40 μm and channele width =2 cm, where the polymer is F8TBT and the gate dilelectric is BMPY-TFSI/SPMMAS ion gel

Prominent $EMIM^+$ Diffusion Under Vacuum

It is interesting that we do see signatures of the electron accumulation in CMS results with F8BT when EMIM-TFSI/SOS ion gel is used, but under the vacuum. However, from the working point of the transistor, under the same conditions, there has not been any electron transportation observed. Figure 2 shows charge modulation spectra taken at different positive gate voltages under the vacuum (refer to chapter 4.)

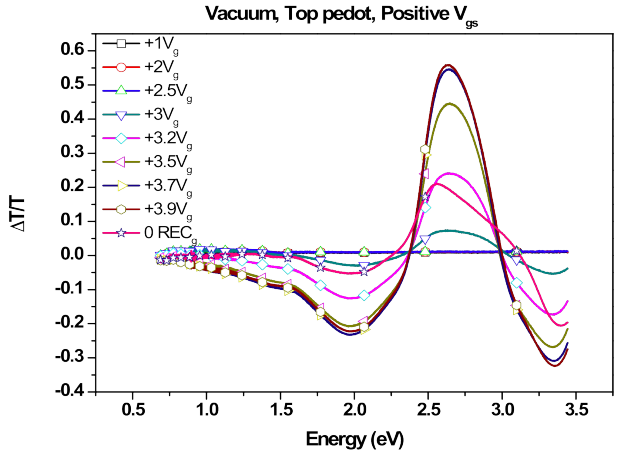

Figure 2: CMS Spectra in electron accumulation regime under vacuum of 10^{-6} mBar. Variation of $\Delta T/T$ with Energy at different gate voltages starting from 1V till 3.9V are shown. Recovery spectrum (0V), after the removal of gate voltage, is shown as well.

It is puzzling that we do see the penetration of EMIM ions into the polymer layer on the application of similar positive gate voltages under vacuum, but not in the nitrogen atmosphere. This might tell something about the variation in the diffusivity constant of EMIM ions under the vacuum compared to the same under the nitrogen atmosphere. The reason for the variation in diffusivity constant for the positive ions between nitrogen atmosphere and vacuum is uncertain.

Nonetheless, no electron transportation under the vacuum, even with the presence of assisting positive ions is explainable. This can be attributed to the slow diffusivity of EMIM ions which limit them to certain spatial regime in the semiconductor channel. Since we haven not been able to observe electron transportation in these devices, possibly due to the unfavorable dielectric and polymer

interface, in order to see the electron transportation in such a system, having EMIM ions throughout the channel, from source to drain is necessary. Under such conditions as well, if the the interface between the semiconductor and gel is not clean for electron transportation, the transistor characteristics might not result.

Appendix: ZnO - A Perfect Hole Blocking Layer

ZnO has been well know for its use as a hole blocking layer[114]. However, with the ZnO patterned electrode devices, when the potential difference is reversed, i.e set in such a way that the holes are supposed to be injected through the ZnO side, we observe a good amount of hole current. If we see the light emission in the middle of the channel, next to ZnO layer (refer figure 5.20 in chapter 5), with the reversed source and drain, light emission shifts promptly next to the now electron injecting Au electrode.

In the first instance it gives us an impression that hole injection is happening through the ZnO layer. This looks reasonable considering the working mechanism of light emitting electrochemical cells, where, on the application of voltage more than the energy gap of the polymer divided by the elementary charge, because of the assistance of ions in the charge injection[101] in such a voltage regime, irrespective of the work function of the electrodes, the hole injection via ZnO layer sounds feasible.

Interpretations of Hole Injection from ZnO side

However, we see clear scaling down of the current matching L=10 μm for electrons via ZnO and L=20 μm for ZnO side biased positively, which means holes are injected from the Au electrode edge underneath the thin ZnO layer rather than holes through ZnO layer, making the effective channel length of 20 μm.

Figure 4 shows such comparison between these two different biasing conditions at different gate voltages at lower V_{ds} (transistor regime) as well higher V_{ds} (LEC)

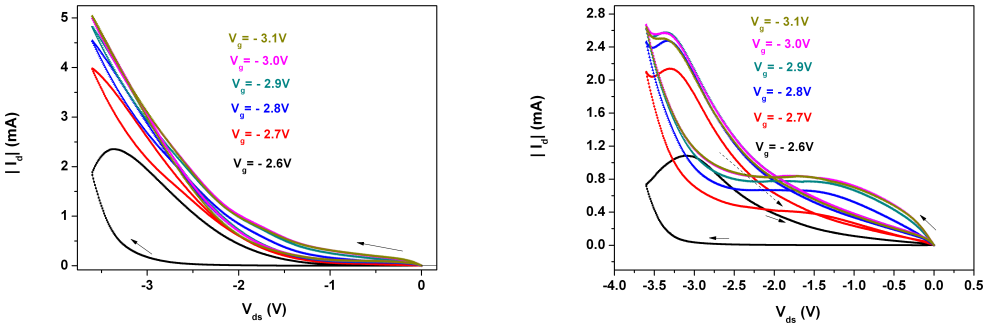

Figure 3: Output characteristics (a) while electrons are injecting through ZnO, L=10 μm (b) while holes are supposed to be injected from the ZnO side.

regime.

Red dots represent the I_d values while electrons are injecting through ZnO, L=10 μm. Black dots represents half of the current value through the channel while electrons are injecting through ZnO and blue dotted line is shows the values of I_d when holes are supposed to be injected from the ZnO side.

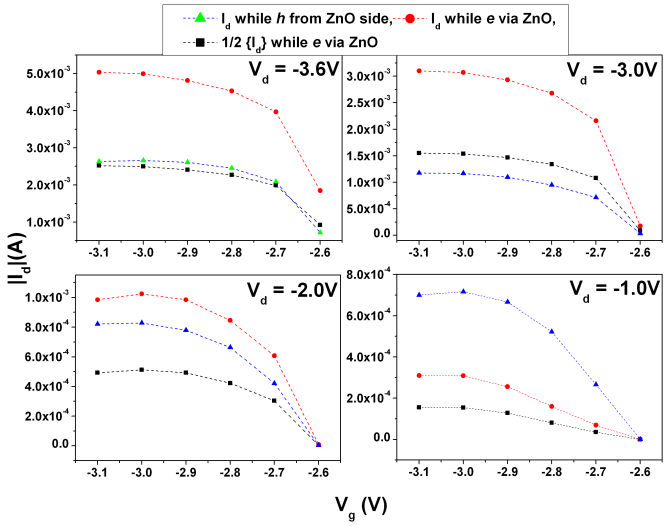

Figure 4: Data showing the comparison of the drain current variation while ZnO is given negative and positive potentials extracted from figure 3

.

It is apparent from figure 4 that the drain source current is scaling by half when the channel length becomes double, especially at higher V_{ds}. At lower V_{ds}

with the L=10 μm combination, this scaling is not really valid as we can see in figure 3(a) that the drain current is contact resistance limited.

We show that the holes which are getting injected from ZnO side are not really injected through ZnO but they are injected from gold electrodes making the effective channel length in this case 20 μm. Regardless of the fact that charges can be injected irrespective of the work function of metal electrodes, these results show that ZnO can be used as safe hole blocking layer in a light emitting electrochemical cells fabrication if needed.

Appendix: Program listing in C

This section provides a program listing used to implement the numerical model discussed in chapter 6. NOTE: Some additional line breaks have been introduced in the listing to fit printable format.

```
# include <stdio.h>
# include <math.h>

int main(void)
{

double totaltime=451; /* Total simulation time - seconds */
double dt=1e-3; /* Time step - seconds */
double x=2.0e-4; /* X dimension of the model - meters */
double y=4.0e-8; /* Y dimension of the model - meters */
double diff=1.0e-19; /*diffusivity in x direction - m2/s */
double lambda=-8.0e-18; /* ion mobility in m2/Vs */

int nx=101; /*number of grid cells in x direction*/
int ny=51; /*number of grid cells in y direction*/
int nt= totaltime/dt;
int i=0;
int j=0;
int t=0;
float interval=0.0;
double transflag = 0.0;
char choice='n';
double c[2][nx][ny]; /*array to store the concentrations*/
double dx,dy,diffx_local,diffy_local,sum[nx],voltage[nx][ny],summax,deltavx, deltavy;
double dv_dx,dphi_dx,d2v_dx2,dv_dy,d2v_dy2,dphi_dy;
int xdoped=nx;


FILE *file; /* results file for raw concentration values */
FILE *integrated; /* results file for integrated values */
dx=x/(nx-1);
dy=y/(ny-1);
```

```
/*initial conditions*/
        for(i=0; i<nx; i++){
                sum[i]=0;
                for (j=0; j<ny; j++){
                        c[0][i][j]=0.0;
                        c[1][i][j]=0.0;
                }
        }



/* some user validation of the data */
printf("dt,␣dx,␣dy␣%e␣%e␣\n␣nt,␣nx,␣ny␣%d␣%d␣%d␣\n␣continue?
y/n␣\n", dt, dx, dy,nt,nx,ny);
scanf("%c", &choice);
if (choice=='n'|| choice =='N') return(0);

printf("Enter␣the␣time␣interval␣for␣transient␣results␣(seconds)\n");
scanf("%f",&interval);

file=fopen("result.txt","w");
fprintf(file,"␣x=␣%e␣\n␣y=␣%e␣time=␣%e␣\n␣nx=␣%d␣\n␣ny=␣%d␣\n␣dx=␣%e␣\n
␣dy=␣%e␣\n␣dt=␣%e␣\n␣Diff=␣%e␣\n\n",x,y,totaltime,nx,ny,dx,dy,dt,diff);
integrated=fopen("integrated.txt","w");
fprintf(integrated,"␣x=␣%e␣\n␣y=␣%e␣time=␣%e␣\n␣nx=␣%d␣\n␣ny=␣%d␣\n␣dx=␣%e
\n␣dy=␣%e␣\n␣dt=␣%e␣\n␣Diff=␣%e␣\n\n",x,y,totaltime,nx,ny,dx,dy,dt,diff);


/*time looping*/
for (t=0;t<nt;t=t++)
{
transflag=transflag+dt;

for(i=nx-1;i>=0;i--)
{
if((sum[i]>=3.999e-18)&&(i<=xdoped)){
        xdoped=i;
        if(transflag>interval)printf("␣now␣doped␣till␣node␣%d␣\n",xdoped);
        }
}


/*Set voltage profile*/
for(i=0;i<xdoped;i++){
                for(j=0;j<ny;j++){
                        voltage[i][j]=3.5*(1-(((double)(xdoped-i)/(double)xdoped)*
                        ((double)(xdoped-i)/(double)xdoped)))*((double)j/(double)ny);
                }
        }
        for(i=xdoped;i<nx;i++){
```

```
                for(j=0;j<ny;j++){
                        voltage[i][j]=1.0*((double)j/(double)ny)*3.5;
                }
        }

/*apply BCs*/
for (i=0;i<nx;i++)
{
c[0][i][0]=1.0e-10;
c[1][i][0]=1.0e-10;
}/*Concentration at gel-F8BT junction*/


/*solve*/
        for (i=1;i<nx-1;i++)
        {

                for (j=1;j<ny-1;j++)
                {

                        dv_dx=(voltage[i][j]-voltage[i-1][j])/dx;
                        dphi_dx=(c[0][i][j]-c[0][i-1][j])/dx;
                        d2v_dx2=((voltage[i+1][j]-2*voltage[i][j]+voltage[i-1][j])/(dx*dx));
                        dv_dy=(voltage[i][j]-voltage[i][j-1])/dy;
                        d2v_dy2= ((voltage[i][j+1]-2*voltage[i][j]+voltage[i][j-1])/(dy*dy));
                        dphi_dy=(c[0][i][j]-c[0][i][j-1])/dy;

                c[1][i][j]=c[0][i][j]+
                (dt)*
                (
                (diff*((c[0][i+1][j]-2*c[0][i][j]+c[0][i-1][j])/(dx*dx))) +
                (diff*((c[0][i][j+1]-2*c[0][i][j]+c[0][i][j-1])/(dy*dy))) +
                 (lambda*dv_dx*dphi_dx) + (lambda*c[0][i][j]*d2v_dx2)+
                 (lambda*dv_dy*dphi_dy) + (lambda*c[0][i][j]*d2v_dy2)
                );
                }
        }


/*Concentration gradient at FTBT-Subsctrate junction is zero.*/
for(i=0;i<nx;i++)
{
c[1][i][ny-1]=c[1][i][ny-2];
}

/* boundary conditions at left and right*/
for(j=1;j<ny;j++){
c[1][0][j]=c[1][1][j];
c[1][nx-1][j]=c[1][nx-2][j];
}
```

```
/*write transient results files*/

if(transflag>interval)
{
transflag=0.0 + dt; /*reset flag for writing transient results*/

/*write transient results on each grid point*/
fprintf(file,"Time=%f␣\n", (t+1)*dt);
fprintf(integrated,"\n␣Time=%f␣", (t+1)*dt);
printf("Simulation␣time␣=␣%f␣seconds␣\n", (t+1)*dt);
for (j=0;j<ny;j++)
{
        fprintf(file,"\n");
        for (i=0;i<nx;i++)fprintf(file,"%e␣",c[1][i][j]);
}
fprintf(file,"\n␣\n");


/*Calculate and write integrated results*/
for (i=0;i<nx;i++)
        {
        sum[i]=0;
        for(j=1;j<ny;j++)sum[i]=sum[i]+(0.5*(c[1][i][j-1]+c[1][i][j])*dy);
        fprintf(integrated,"%e␣",sum[i]);
        }
}


/*move results from new timestep to old timestep*/

        for (i=1;i<nx;i++)
        {
                for (j=1;j<ny;j++)
                {
                        c[0][i][j]=c[1][i][j];
                }
        }


} /*end of time loop*/

fclose(file);
fclose(integrated);
return 0;

}
```

List of Abbreviations

Roman Symbols

AFM	Atomic Force Microscopy
BMIM-PF6	1-butyl-3-methyl imidazolium hexa fluorophosphate
BMPY-TFSI	1-butyl-4-methyl pyridinium bis(trifluoromethane sulfonyl)imide
CMS	Charge Modulation Spectroscopy
EDL	Electrical Double Layer
EL	ElectroLuminescence
EMIM-TFSI	1-ethyl-3-methyl imidazolium bis(trifluoro methylsulfonyl)imide
EQE	External Quantum Efficiency
F8BT	poly(9,9-dioctyl fluorene-co-benzo thiadiazole)
F8T2	poly(9,9-dioctyl fluorene-alt-bithiophene)
F8TBT	poly(9,9-dioctyl fluorene)-2,7-diyl-alt-[4,7-bis(3-hexyl thiophen-5-yl)-2,1,3-benzo thiadiazole]-2,2-diyl)
FET	Field Effect Transistor
HOMO	Highest Occupied Molecular Orbital
LEC	Light emitting Electrochemical Cell
LED	Light Emitting Diode

LEFET	Light Emitting Field Effect Transistor
LUMO	Lowest Unoccupied Molecular Orbital
OC1OC10	poly(2-methoxy-5-(3,7-dimethyl octoxy)-p-phenylene vinylene)
PEO	Poly- Ethylene Oxide
PIA	Polaron Induced Absorption
PL	PhotoLuminescence
PMMA	poly(methyl methacrylate)
SOS	poly(styrene- block- ethylene oxide-block- styrene)
SPA	Semiconductor Parameter Analyser
SPMMAS	poly(styrene-block-methyl methacrylate-block-styrene)
TFSI	bis(TriFluoro methylSulfonyl)Imide

References

[1] Kohler A. and Beljonne D. *Adv. Funct. Mater.*, 14(11), 2004. 10

[2] Saleh B. E. A. and Teich M. C. Fundamentals of photonics. *Wiley, New York*, 1991. 14

[3] Michel Armand, Frank Endres, Douglas R Macfarlane, Hiroyuki Ohno, and Bruno Scrosati. Ionic-liquid materials for the electrochemical challenges of the future. *Nature Publishing Group*, 8(8):621–629, Jan 2009. doi: 10.1038/nmat2448. 43

[4] Carmen Bartic, Henri Jansena, Andrew Campitelli, and Staf Borghs. Ta2o5 as gate dielectric material for low-voltage organic thin-film transistors. *Organic Electronics*, 3:65–72, 2002. 26

[5] H. Becker, A. Lux, A.B. Holmes, and R.H. Friend. Pl and el quenching due to thin metal films in conjugated polymers and polymer leds. *Synthetic Metals*, 85:1289–1290, 1997. 76, 88

[6] D. Beljonne, J. Cornil, H. Sirringhaus, P.J. Brown, M. Shkunov, R.H. Friend, and J.-L. Bredas. Optical signature of delocalized polarons in conjugated polymers. *Advanced Functional Materials*, 11:229–234, 2001. 69, 75

[7] J. Blochwitz, M. Pfeiffer T. Fritz, and K. Leo. Low voltage organic light emitting diodes featuring doped phthalocyanine as hole transport material. *Appl. Phys. Lett.*, 73:729, 1998. 1

[8] D. Braun and A. J. Heeger. Visible-light emission from semiconducting polymer diodes. *Appl. Phys. Lett*, 58:1982–1984, 1991. 8

[9] J. H. Burroughes, C. A. Jonnes, and R. H. Friend. New semiconductor device physics in polymer diodes and transistors. *Nature*, 335:137–141, 1988. 8

[10] J. H. Burroughes, D. D. C. Bradley, A. R. Brown, R. N. Marks, K. Mackay, R. H. Friend, P. L. Burn, and A. B. Holmes. Light-emitting diode based on conjugated polymers. *Nature*, 347:539–41, 1990. 1, 11

[11] Marisa C Buzzeo, Christopher Hardacre, and Richard G Compton. Electrochemical window emim tfsi extended electrochemical windows made accessible by room temperature ionic liquid/ organic solvent electrolyte systems. *ChemPhysChem*, 7:176–180, 2006. 54

[12] I. H. Campbell, D. L. Smith, C. J. Neef, and J. P. Ferraris. Capacitance measurements of junction formation and structure in polymer light-emitting electrochemical cells. *Appl. Phys. Lett*, 72:2565–2567, 1998. 16

[13] Y. Caoa, G. Yua, C. Zhanga, R. Menonb, and A. J. Heeger. Polymer light-emitting diodes with polyethylene dioxythiophenepolystyrene sulfonate as the transparent anode. *Synthetic Metals*, 87:171–174, 1997. 16

[14] J.-F. Chang, M. C. Gwinner, M. Caironi, T. Sakanoue, and H. Sirringhaus. Conjugated-polymer-based lateral heterostructures defined by high-resolution photolithography. *Adv. Funct. Mater.*, 20:2825–2832, 2010. 39, 54

[15] J Cho, J Lee, Y Xia, B Kim, Y He, and M Renn. Printable ion-gel gate dielectrics for low-voltage polymer thin-film transistors. *Nature Materials*, 129:4532–4533, 2007. 43, 44, 49, 54, 82

[16] J.H Cho, J Lee, Y He, B.S Kim, T.P Lodge, and C.D Frisbie. High-capacitance ion gel gate dielectrics with faster polarization response times for organic thin film transistors. *Adv. Mater.*, 20(4):686–690, Feb 2008. doi: 10.1002/(ISSN)1521-4095. 27, 43

[17] Lay-Lay Chua, Jana Zaumseil1, Jui-Fen Chang, Eric C.W.and Peter K.H., Henning Sirringhaus, and Richard H. Friend. General observation of n-

type field-effect behaviour in organic semiconductors. *Nature*, 434:194–199, 2005. 24

[18] B. E. Conway and W. G. Pell. Double-layer and pseudocapacitance types of electrochemical capacitaors and thier applications to the ddevelopment of hybrid devices. *Journal of Solid State Electrochem*, 7:637–644, 2003. 47, 48

[19] J. Cornil and J.L. Bredas. Nature of the optical transitions in charged oligothiophenes. *Adv.Mater.*, page 295, 1995. 11, 68

[20] Gregory P. Crawford. *Flexible Flat Panel Display Technology*. 2005. 81

[21] J. Dane, C. Tracy, and J. Gao. Direct observation of a frozen junction in polymer light-emitting electrochemical cells. *Appl. Phys. Lett.*, 86:153509, 2005. 144

[22] J. C. DeMello. Interfacial feedback dynamics in polymer light-emitting electrochemical cells. *Phys Rev B*, 66:235210, 2002. 19

[23] J C DeMello, N Tessler, S C Graham, and R H Friend. Ionic space-charge effects in polymer light-emitting diodes. *Phys. Rev. B*, 57(20):12951–12963, May 1998. 19

[24] J.C. Demello. *Nature Materials*, 6:796, 2007. 17

[25] Diode details, 2009. `http://sales.hamamatsu.com/en/products/solid-state-division/si-photodiode-series/si-photodiode/part-s1133-01.php`. 38, 39

[26] Spectrometer details. `http://www.chem.agilent.com/en-US/Search/Library/_layouts/Agilent/PublicationSummary.aspx?whid=68020&liid=1695`. 40

[27] D. J. Dick, A. J. Heeger, Y. Yang, and Q. B. Pei. Imaging the structure of the p-n junction in polymer light-emitting electrochemical cells. *Adv. Mater*, 8:985–987, 1996. 16

[28] C. D. Dimitrakopoulos, S. Purushothaman, J. Kymissis, A. Callegari, and J. M. Shaw. Low-voltage organic transistors on plastic comprising high-dielectric constant gate insulators. *Science*, 283:822–824, 1999. 26

[29] Ludvig Edman. Bringing light to solid-state electrolytes: The polymer light-emitting electrochemical cell. *Electrochimica Acta*, 50:3878–3885, 2005. 82

[30] A. Paul et al. *Chemical Physics Letters*, 402:375–379, 2005. 28

[31] M.Bird et al. *to be published.*, 2010. 69, 71

[32] M.Gwinner et al. *to be published.*, 2010. 71

[33] Slinker et al. *Nature Materials*, 6:894, 2007. 16, 80

[34] Y. He et al. *J. Phys. Chem. B*, 111:4645, 2007. 28

[35] Baldo M.A. etal. Highly efficient phosphorescent emission from organic electroluminescent devices. *Nature*, 395:151–154, 1998. 12

[36] Alvarado S. F., Seidler P. F., Lidzey D. G., and Bradley D. D. C. Direct determination of the exciton binding energy of conjugated polymers using a scanning tunneling microscope. *Phys. Rev. Lett*, 81:1082–1085, 1998. 9, 13

[37] J. Fang, Y. Yang, and L. Edman. *Appl. Phys. Lett.*, 93:063503, 2008. 85

[38] Stephen R. Forrest. The road to high efficiency organic light emitting devices. *Organic Electronics*, 4:45–48, 2003. 81

[39] Heiko Frenzel, Alexander Lajn, Holger von Wenckstern, Michael Lorenz, Friedrich Schein, Zhipeng Zhang, and Marius Grundmann. Mesfet electronics:recent progress on zno-based metal-semiconductor field-effect transistors and their application in transparent integrated circuits. *Advanced Materials*, 22 (47):5323, 2010. 94

[40] R. H. Friend, Gymer R. W.and Holmes A. B., Burroughes J. H., Marks R. N., Taliani C., Bradley D. D. C., Santos D. A. D., Bredas J. L., Logdlund M., and Salaneck W. R. *Nature*, 397:121, 1999. 10, 11, 12, 14

[41] J. Gao and J. Dane. Visualization of electrochemical doping and light emitting junction formation in conjugated polymer films. *Appl. Phys. Lett.*, 84:2778–2780, 2004. 16

[42] J. Gao, A. J. Heeger, I. H. Campbell, and D. L. Smith. Direct observation of junction formation in polymer light-emitting electrochemical cells. *Phys. Rev. B,*, 59:2482–2485, 1999. 16

[43] Bernard Geffroy, Philippe le Roy, and Christophe Prat. Organic light-emitting diode (oled) technology: materials, devices and display technologies. *Polymer International*, 55:572582, 2006. 81

[44] F. M. Gray. Solid polymer electrolytes: Fundamentals and techno- logical applications. *VCH Publishers, New York*, 1991. 27

[45] Y. Greenwald, F. Hide, J. Gao, F. Wudl, and A. J. Heeger. Cyclic voltammetry studies of light-emitting electrochemical cells. *J. Electrochem. Soc.*, 144:70–72, 1997. 16

[46] M Gross, DC Muller, HG Nothofer, U Scherf, D Neher, C Brauchle, and K Meerholz. Improving the performance of doped pi-conjugated polymers for use in organic light-emitting diodes. *Nature*, 405(6787):661–665, Jan 2000. 1

[47] Johannes Grüner, Marcus Remmers, and Dieter Neher. Direct determination of the emission zone in a polymer light-emitting diode. *Advanced Materials*, 9:964–968, 1997. 92

[48] G. Gustafsson, Y. Cao, G. M. Treacy, F. Flavetter, N. Colaneri, and A. J. Heeger. Flexible light-emitting diodes made from soluble conducting polymer. *Nature*, 357:477–479, 1992. 8

[49] M. C. Gwinner, Y. Vaynzof, K. K. Banger, P. K. H. Ho, R. H. Friend, and H. Sirringhaus. Solution-processed zinc oxide as high-performance air-stable electron injector in organic ambipolar light-emitting field-effect transistors. *Adv. Funct. Mater.*, 20:3457–3465, 2010. 35, 96

[50] Bassler H. Injection,transport and recombination of charge carriers in organic light-emitting diodes. *Polym. Adv. Technol.*, 9:402–418, 1998. 12

[51] Brown P. J.and Sirringhaus H., Harrison M., Shkunov M., and Friend R. H. *Phys.Rev. B*, 63:125204, 2001. 11, 67

[52] Shimotani H., Asanuma H., Takeya J., and Iwasa Y. *Appl. Phys. Lett.*, 89: 203501, 2006. 26

[53] Marcus Halik, Hagen Klauk, Ute Zschieschang, Günter Schmid, Christine Dehm1, Markus Schütz, Steffen Maisch, Franz Effenberger, Markus Brunnbauer, and Francesco Stellacci. Low-voltage organic transistors with an amorphous molecular gate dielectric. *Nature*, 431:963–966, 2004. 26

[54] M.G. Harrison, R.H. Friend, F. Garnier, and A. Yassar. The charged excitations in thin films of [alpha]-sexithiophene within semi-transparent field-effect devices: investigation by optical spectroscopy of field-induced charge and by photoimpedance spectroscopy. *Synthetic Metals*, 67:215–221, 1994. 67

[55] Gufeng He, Oliver Schneider, Dashan Qin, Xiang Zhou, Martin Pfeiffer, and Karl Leo. Very high-efficiency and low voltage phosphorescent organic light-emitting diodes based on a p-i-n junction. *J. Appl. Phys.*, 95:5773, 2004. 1

[56] Aline Hepp, Holger Heil, Wieland Weise, Marcus Ahles, Roland Schmechel, and Heinz von Seggern. Light-emitting field-effect transistor based on a tetracene thin film. *Physical Review Letters*, 9:157406, Oct 2003. 1, 24, 57

[57] Justin M. Hodgkiss, Guoli Tueifried, Wilhelm T. S. Huck, and Richard H. Friend. Ion-induced formation of charge-transfer states in conjugated polyelectrolytes. *J. Am. Chem. Soc*, 131:8913–8921, 2009. 44, 62, 65, 93

[58] Y. Hu, C. Tracy, and J. Gao. High-resolution imaging of electrochemical doping and dedoping rocesses in luminescent conjugated polymers. *Appl. Phys. Lett*, 88:123507, 2006. 16

[59] Jingsong Huang, Martin Pfeiffer, Ansgar Werner, Jan Blochwitz, Karl Leo1, and Shiyong Liu. Low-voltage organic electroluminescent devices using pin structures. *Appl. Phys. Lett.*, 80:139, 2002. 1

[60] Panzer M. J. and Frisbie C. D. *Appl. Phys. Lett*, 88:203504, 2006. 26

[61] Takeya J., Yamada K., Shigeto K., Tsukagoshi K., Ikehata S., and Aoyagi Y. *Appl. Phys. Lett*, 88:112102, 2006. 26

[62] Scott J.C., Karg S., and Carter S.A. Bipolar charge and current distributions in organic light-emitting diodes. *J. Appl. Phys.*, 82:1454–1460, 1997. 12

[63] L G Kaake, Y Zou, M J Panzer, C D Frisbie, and X-Y Zhu. Vibrational spectroscopy reveals electrostatic and electrochemical doping in organic thin film transistors gated with a polymer electrolyte dielectric. *J. Am. Chem. Soc*, 129:7824–7830, Feb 2007. 29, 43

[64] Loren G. Kaake, Bryan D. Paulsen, C. D. Frisbie, and X.Y. Zhu. Mixing at the charged interface of a polymer semiconductor and a polyelectrolyte dielectric. *J. Phys. Chem. Lett*, 1(5):862–867, 2010. 29

[65] Dinesh Kabra, Li Ping Lu, Myoung Hoon Song, Henry J. Snaith, and Richard H. Friend. Efficient single-layer polymer light-emitting diodes. *Advanced Materials*, 22(19):3194–3198, 2010. 1

[66] Moon Sung Kang, Jiyoul Lee, David J Norris, and C Daniel Frisbie. High carrier densities achieved at low voltages in ambipolar pbse nanocrystal thin-film transistors. *Nano Lett.*, 9(11):3848–3852, Oct 2009. 43, 44

[67] N. Karl and Marktanner. *J. Mol. Cryst. Liquid Cryst.*, 149:355, 2001. 23

[68] Sun Woong Kim, Byong Hoon Hwang, Joo Hyeon Lee, Jae Ik Kang, Kyoung Wook Min, and Woo Young Kim. 2.4-in monochrome small molecular oled display for mobile application. *Current Applied Physics*, 2:335–338, 2002. 81

[69] Hagen Klauk, Ute Zschieschang, Jens Pflaum, and Marcus Halik. Ultralow-power organic complementary circuits. *Nature*, 445:745–748, 2007. 26

[70] Breadas J. L., Cornil J., and Heeger A. J. The excitonbinding-energy inluminescent conjugated polymers. *Adv. Mater.*, 8:447–452, 1996. 13

[71] Y. Lauw, M. D. Horne, T. Rodopoulos, A. Nelson, and F. A. M. Leermakers. Electrical double-layer capacitance in room temperature ionic liquids: Ion-size and specific adsorption effects. *J. Phys. Chem. B,*, 114 (34):11149–11154, 2010. 26, 48, 49

[72] Jiyoul Lee, Matthew J Panzer, Yiyong He, Timothy P Lodge, and C Daniel Frisbie. Ion gel gated polymer thin-film transistors. *J. Am. Chem. Soc.*, 129:4532–4533, Mar 2007. doi: 10.1021/ja070875e. 2, 28, 29, 43

[73] Jiyoul Lee, Loren G Kaake, Jeong Ho Cho, X-Y Zhu, Timothy P, and C Daniel Frisbie. Ion gel-gated polymer thin-film transistors: Operating mechanism and characterization of gate dielectric capacitance, switching speed, and stability. *J. Phys. Chem. C 2009, 113, 8972–8981*, 113:8972–8981, May 2009. 30, 43, 49, 114, 123, 130, 137

[74] J.M. Leger. Organic electronics: The ions have it. *Advanced Materials*, 20: 837841, 2008. 30

[75] Y. F. Li, J. Gao, G. Yu, Y. Cao, and A. J. Heeger. Ac impedance of polymer light-emitting electrochemical cells and light-emitting diodes: A comparative study. *Chem. Phys. Lett*, 287:83–88, 1998. 16

[76] Huixuan Liu, Jia Sun, Qingxin Tang, and Qing Wan. Ultralow-voltage electric double-layer sno2 nanowire transistors gated by microporous sio2 based solid electrolyte. *J. Phys. Chem. C*, 114 (28):12316–12319, 2010. 26

[77] Timothy P Lodge. A unique platform for materials design. *Science*, 321: 50, Mar 2008. 28, 43

[78] Cleave V. M., Yahioglu G., LeBarny P., Friend R. H., and Tessler N. Harvesting of singlet and triplet energy in polymer leds. *Adv. Mater.*, 11: 285–288, 1999. 12

[79] Pope M. and Swenberg C. E. Electronic processes in organic crystals. *Clarendon Press, Oxford*, 1982. 10

[80] G. Malliaras and R. Friend. An organic electronics primer. *Phys Today*, 58: 53–58, 2005. 11

[81] G. et al. Malliaras. Operating mechanism of light-emitting electrochemical cells-authors' response. *Nature Materials*, 7:168, 2008. 19

[82] J. A. Manzanares, H. Riess, and A. J. Heeger. Polymer light-emitting electrochemical cells: A theoretical study of junction formation under steady-state conditions. *J. Phys. Chem. B*, 102:4327–4336, 1998. 16, 17

[83] Rebeca Marcilla, David Mecerreyes, Gustaf Winroth, Sergio Brovelli, Maria Del Mar Rodriguez Yebra, and Franco Cacialli. Light-emitting electrochemical cells using polymeric ionic liquid/polyfluorene blends as luminescent material. *Appl. Phys. Lett.*, 96:043308–3, 2010. 80

[84] Rebeca Marcilla, David Mecerreyes, Gustaf Winroth, Sergio Brovelli, Maria Del Mar Rodriguez Yebra, and Franco Cacialli. Light-emitting electrochemical cells using polymeric ionic liquid/polyfluorene blends as luminescent material. *Appl. Phys. Lett.*, 96(4):043308, Jan 2010. 83

[85] Toshinori Matsushima and Chihaya Adachi. Extremely low voltage organic light-emitting diodes with p-doped alpha-sexithiophene hole transport and n-doped phenyldipyrenylphosphine oxide electron transport layers. *Appl. Phys. Lett.*, 89:253506, 2006. 1

[86] Piotr Matyba, Klara Maturova, Martijn Kemerink, Nathaniel D Robinson, and Ludvig Edman. The dynamic organic p–n junction. *Nature Materials*, 8:672–676, 2009. 16, 18, 19, 80, 134

[87] A. Miller and E. Abrahams. *Phys. Rev.*, 120:745, 1960. 23

[88] T Mills, L Kaake, and X Zhu. Polaron and ion diffusion in a poly (3-hexylthiophene) thin-film transistor gated with polymer electrolyte dielectric. *Applied Physics A: Materials Science & Processing*, 95:291–296, Jan 2009. 29, 43, 137

[89] J. Morgadoa, R.H. Friend, F. Cacialli, B.S. Chuah, H. Rost, S.C. Moratti, and A.B. Holmes. Light-emitting electrochemical cells based on poly(p-phenylene vinylene) copolymers with ion-transporting side groups. *Synthetic Metals*, 122:111–113, 2001. 82

[90] N. F. Mott and E. A. Davis. *Electronic processes in non-crystalline materials.* Oxford University Press, London, 2nd edition, 1979. 23

[91] M. Muccini. *Nature Materials*, 5:605, 2006. 25

[92] Herbert Naarmann. *Polymers, Electrically Conducting.* Wiley-VCH Verlag GmbH and Co. KGaA, 2000. ISBN 9783527306732. 7

[93] S Ono, S Seki, R Hirahara, Y Tominari, and J Takeya. High-mobility, low-power, and fast-switching organic field-effect transistors with ionic liquids. *Appl. Phys. Lett*, 92:103313–3, Mar 2008. 43

[94] S Ono, K Miwa, S Seki, and J Takeya. High-performance organic field-effect transistors with binary ionic liquids. *Organic Electronics*, 10(8):1579–1582, Dec 2009. doi: 10.1016/j.orgel.2009.09.004. 43

[95] O. Ostroverkhova, D. G. Cooke, F. A. Hegmann, J. E. Anthony, V. Podzorov, M. E. Gershenson, O. D. Jurchescu, and T. T. M. Palstra. *Appl. Phys. Lett*, 88:162101, 2006. 23

[96] Matthew J Panzer and C Daniel Frisbie. Polymer electrolyte-gated organic field-effect transistors: Low-voltage, high-current switches for organic electronics and testbeds for probing electrical transport at high charge carrier density. *J. Am. Chem. Soc*, 129:6599–6607, Feb 2007. 43

[97] Matthew J Panzer and C. Daniel Frisbie. Exploiting ionic coupling in electronic devices: Electrolyte-gated organic field-effect transistors. *Adv. Mater.*, 20(16):3177–3180, Aug 2008. doi: 10.1002/adma.200800617. 27, 43, 48, 49, 82

[98] Matthew J. Panzer, Christopher R. Newman, and C. Daniel Frisbie. Low-voltage operation of a pentacene field-effect transistor with a polymer electrolyte gate dielectric. *Appl. Phys. Lett.*, 86:103503, 2005. 26

[99] Q. Pei and A. J. Heeger. Operating mechanism of light-emitting electrochemical cells. *Nature Materials*, 7:167, 2008. 19

[100] Q. B. Pei, G. Yu, C. Zhang, Y. Yang, and A. J. Heeger. Polymer light-emitting electrochemical-cells. *Science*, 269:1086–1088, 1995. 16, 17

[101] Q. B. Pei, Y. Yang, G. Yu, C. Zhang, and A. J. Heeger. Polymer light-emitting electrochemical cells: In situ formation of a light-emitting p-n junction. *J. Am. Chem. Soc.*, 118:3922–3929, 1996. 1, 14, 15, 16, 81, 82, 93, 151

[102] Liam S. C. Pingree, Deanna B. Rodovsky, David C. Coffey, Glenn P. Bartholomew, and David S. Ginger. Scanning kelvin probe imaging of the potential profiles in fixed and dynamic planar lecs. *J. Am. Chem. Soc*, 129: 1590315910, 2007. 19, 80

[103] V. Podzorov, Menard, E., Rogers, J. A., and M. E. Gershenson. *Phys. Rev. Lett.*, 95:226601, 2005. 23

[104] M. Pope, H. P. Kallmann, and P. Magnante. Electroluminescence in organic crystals. *The Journal of Chemical Physics*, 38:2042, 1963. 11

[105] Blom P.W.M., deJong M.J.M., and Breedijk S. Temperature dependent electron-hole recombination in polymer light-emitting diodes. *Appl. Phys. Lett.*, 71:930–932, 1997. 12

[106] Sebastian Reineke1, Frank Lindner1, Gregor Schwartz1, Nico Seidler1, Karsten Walzer1, Bjorn Lussem1, and Karl Leo. White organic light-emitting diodes with fluorescent tube efficiency. *Nature*, 459:234–238, 2009. 13

[107] I. Riess and D. Cahen. Analysis of light emitting polymer electrochemical cells. *J. Appl. Phys.*, 82:3147–3151, 1997. 16

[108] Nathaniel D. Robinson, Joon-Ho Shin, Magnus Berggren, and Ludvig Edman. Doping front propagation in light-emitting electrochemical cells. *Phys. Rev. B*, 74:155210, 2006. 65

[109] Nathaniel D. Robinson, Junfeng Fang, Piotr Matyba, and Ludvig Edman. Electrochemical doping during light emission in polymer light-emitting electrochemical cells. *Phys. Rev. B*, 78:245202, 2008. 85, 93

[110] Dhoot A. S., Yuen J. D., Heeney M., McCulloch I., Moses D., and Heeger. *A. J.Proc. Natl. Acad. Sci. U.S.A.*, 103:11834–11837, 2006. 26

[111] Kim J. S., Ho P. K. H., Greenham N. C., and R. H. Friend. *J. Appl. Phys*, 88:1073, 2000. 14

[112] M. Sampietro, R. Sotgiu, F. P. Wenzl, L. Holzer, S. Tasch, and G. Leising. Electrical characteristics of light-emitting electrochemical cells based on a wide bandgap polymer. 61:266–271, 2000. 16

[113] Andreas Sandstrom, Piotr Matyba, Olle Inganas, and Ludvig Edman. Separating ion and electron transport: The bilayer light-emitting electrochemical cell. *J. Am. Chem. Soc*, 132:6646–6647, 2010. 4, 44, 45, 82, 83

[114] Galileo Sarasqueta, Kaushik Roy Choudhury, Jegadesan Subbiah, and Franky So. Organic and inorganic blocking layers for solution-processed colloidal pbse nanocrystal infrared photodetectors. *Adv. Funct. Mater*, 21: 167–171, 2011. 151

[115] L. B. Schein, C. B. Duke, and A. R. McGhie. *Phys. Rev. Lett.*, 40:197, 1978. 23

[116] William E. Schiesser and Graham W. Griffiths. *A Compendium of Partial Differential Equation Models.* Cambridge University Press, 2009. 115

[117] Giles P. Siddons, David Merchin, Ju Hee Back, Jae Kyeong Jeong, and Moonsub Shim. Highly efficient gating and doping of carbon nanotubes with polymer electrolytes. *Nano Letters*, 4(5):927–931, 2004. 28

[118] D. L. Smith. Steady state model for polymer light-emitting electrochemical cells. *J. Appl. Phys.*, 81:2869–2880, 1997. 16

[119] Qingjiang Sun, Yongfang Li, and Qibing Pei;. Polymer light-emitting electrochemical cells for high-efficiency low-voltage electroluminescent devices. *Display Technology, Journal of*, 3(2):211–224, Jun 2007. doi: 10.1109/JDT.2007.896737. 16, 19, 20, 44

[120] S. M. Sze. *Semiconductor Devices - Physics and Technology*. John Wiley and Sons Inc, 2002. 21

[121] Ozel T., Gaur A., Rogers J. A., and Shim M. *Nano Lett*, 5:905–911, 2005. 26

[122] Tsukasa Torimoto, Tetsuya Tsuda, Ken-Ichi Okazaki, and Susumu Kuwabata. New frontiers in materials science opened by ionic liquids. *Adv. Mater.*, page 1326, Dec 2009. doi: 10.1002/adma.200902184. 43

[123] T. Tsuzuki and S. Tokito. Highly efficient and low-voltage phosphorescent organic light-emitting diodes using an iridium complex as the host material. *Advanced Materials*, 19:276280, 2007. 1

[124] Rauscher U., Bassler H., Bradley D. D. C., and Hennecke M. *Phys. Rev. B*, 42:9830, 1990. 9

[125] T Uemura, R Hirahara, Y Tominari, S Ono, S Seki, and J Takeya. Electronic functionalization of solid-to-liquid interfaces between organic semiconductors and ionic liquids: Realization of very high performance organic single-crystal transistors. *Appl. Phys. Lett*, 93:1433, Dec 2008. 29, 43

[126] T Uemura, M Yamagishi, S Ono, and J Takeya. Low-voltage operation of n-type organic field-effect transistors with ionic liquid. *Appl. Phys. Lett.*, 95(10):103301, Jan 2009. doi: 10.1063/1.3225153. 43

[127] Stephan van Reenen, Piotr Matyba, Andrzej Dzwilewski, Ren A. J. Janssen, Ludvig Edman, and Martijn Kemerink. A unifying model for the operation of light-emitting electrochemical cells. *J. Am. Chem. Soc.*, 132(39):13776–13781, 2010. 17, 19

[128] J. Veres, S. Ogier, G. Lloyd, and D de Leeuw. *Chem. Mat.*, 16:4543, 2004. 21

[129] D'Andrade B. W. and Forrest S. R. *Adv. Mater*, 16:1585, 2004. 11

[130] Tang C. W. and Vanslyke S. A. *Appl. Phys. Lett.*, 51,:913, 1987. 11

[131] F. P. Wenzl, C. Suess, A. Haase, P. Poelt, D. Somitsch, P. Knoll, U. Scherfe, and G. Leising. The influence of spatial disorder of the ion distribution on the surface morphology in thin films of blend based organic mixed ionic-electronic conductors. *Thin Solid Films*, 433:263–268, 2003. 82

[132] Deng Y. Y. and Sirringhaus H. *Phys. Rev. B*, 72:045207, 2005. 11, 72, 73

[133] CH Yang, QJ Sun, J Qiao, and YF Li. Ionic liquid doped polymer light-emitting electrochemical cells. *J Phys Chem B*, 107(47):12981–12988, Jan 2003. doi: 10.1021/jp034818t. 82

[134] G. Yu, J. Gao, J. C. Hummelen, F. Wudl, and A. J. Heeger. Polymer photovoltaic cells: Enhanced efficiencies via a network of internal donor-acceptor heterojunctions. *Science*, 270:1789–1791, 1995. 8

[135] G. Yu, Y. Cao, C. Zhang, Y. F. Li, J. Gao, and A. J. Heeger. Complex admittance measurements of polymer light-emitting electrochemicalcells: Ionic and electronic contributions. *Appl. Phys. Lett.*, 73:111–113, 1998. 16

[136] Jana Zaumseil. *N-Channel, Ambipolar and Light-Emitting Polymer Field-Effect Transistors*. 2006. 9, 10, 14, 21

[137] Jana Zaumseil and Henning Sirringhaus. Electron and ambipolar transport in organic field-effect transistors. *Chem. Rev.*, 107:1296–1323, Dec 2007. doi: 10.1021/cr0501543. 24, 44

[138] Jana Zaumseil, Carrie L. Donley, Ji-Seon Kim, Richard H. Friend, and Henning Sirringhaus. Efficient top-gate, ambipolar, light-emitting field-effect transistors based on a green-light-emitting polyfluorene. *Adv. Mater*, 18:2708 –2712, 2006. 1, 56, 75

[139] Jana Zaumseil, Xinning Ho, Jeffrey R. Guest, Gary P. Wiederrecht, and John A. Rogers. Electroluminescence from electrolyte-gated carbon nanotube field-effect transistors. *ACS Nano*, 3 (8):2225?2234, 2009. 28

[140] N. Zhao, Y.-Y. Noh, J.-F. Chang, M. Heeney, I. McCulloch, and H Sirringhaus. Polaron localization at interfaces in high-mobility microcrystalline conjugated polymers. *Advanced Materials*, 21:37593763, 2009. 72, 73